

**I: Retrieval of Atmospheric Carbon Dioxide
from High-Resolution Spectra**

**II: Interannual Variability of the Stratospheric
Quasi-Biennial Oscillation**

Thesis by

Le Kuai (蒯乐)

In Partial Fulfillment of the Requirements

for the Degree of

Doctor of Philosophy



California Institute of Technology

Pasadena, California

2011

(Defended April 22, 2011)

© 2011

Le Kuai (蒯乐)

All Rights Reserved

Dedicated to my parents

Acknowledgements

It is like yesterday that I visited Caltech for the first time. After five years, I completed this thesis with the help of many people in many ways. Before I express my gratitude to them, I must thank my cousin, Ying Zhang and her husband, Rongkun Zhang. They urged me to apply to Nanjing University when I did not trust myself that I could do it. Again, they encouraged me to apply to Caltech. They are both very successful in their careers and have more experience than I. Without their advice and support, I would not have achieved my educational goals. Although Ying is my cousin, she is more than my real sister. She is a talented, graceful, beautiful, and extremely strong woman. She remains optimistic under any circumstance. I learned a lot from her.

The second strongest woman in my family is my dear mum. My advisor, Professor Yuk Yung, has a comment about her: "I believe if your mum has an opportunity for graduate school, she will do even better than you." I would like to thank her for devoting most of her life to raising me and educating me to be the third strongest woman in our family. My father always shows me how to earn respect from others by working hard, being generous and being brave. It is the best wealth he gave me and makes my life much smoother.

I want to express my most sincere appreciations to my advisor, Professor Yuk Yung. In addition to training me how to be successful in research, he also taught me how to face my life. Without his patient and guidance, I would not have been able to survive the competition at Caltech. I must thank my other professors, Andrew Ingersoll, Paul Wennberg, Mike Brown, Geoffrey Blake, Mark Richardson, along with outstanding scientists, Charles Miller, Brian Connor, Moustafa Chahine, Jack Margolis, David Crisp,

Kevin Bowman, John Worden, and Duane Waliser. I really appreciate the insightful comments of Professor Ka-Kit Tung on our two QBO papers.

I present my most special thanks to Dr. Run-Lie Shia. He is a brilliant scientist and provided me great advice on all my papers. My acknowledgements should also go to Vijay Natraj, who introduced me to the retrieval project. I thank Gretchen Keppel Aleks, Debra Wunch, and Geoffrey Toon for their kindly guidance in GFIT. I have benefited greatly from the discussions with my research group members, including Xun Jiang, Daniel Feldman, Daniel Liao, Nicholas Heavens, Xi Zhang, Michael Line, King-Fai Li, and Sally Newman.

The support from staff members, including Irma Black, Alexandra Tigno, Margaret Carlos, Nora Oshima, Mike Black, Scott Dungan, Ken Ou, and Shawn Ewald is gratefully acknowledged.

I cherish the memories I share with my awesome officemates, Margarita Marinova, Darin Ragozzine, Alejandro Soto, Aaron Wolf, Miki Nakajma, and fellow graduate students, including Alex Hayes, Kaveh Pahlevan, Colette Salyk, and Xin Guo. I express my gratitude to my dear friends, Junting Fu, Yi-Chun Chen, Xiang Liu, Icy Ma, Tan Liu, Rui Huang, Yanlin Wu, Yu Zhao, Li Liu, Jie Chen, Xi Zhang, Da Yang, Zan Zhang, and Wendian Shi. Constant warm support has kept coming from my adorable friends at a distance, Ye Sun, Jing Dai, Fei Gu, Wei Cai, Tim Zhang, and Hong Hua.

A complete list would not be possible, but I hope to take this opportunity to express to some extent my gratitude to those people who care about me.

Table of Contents

List of Figures	ix
List of Tables	xi
Overview	xii
Part I: Retrieval of Atmospheric Carbon Dioxide from High-Resolution Spectra1	
Chapter 1: Channel Selection Using Information Content Analysis: A Case Study of CO₂ Retrieval from Near-Infrared Measurements	2
Abstract.....	3
1.1 Introduction.....	4
1.2 Model	8
1.3 Channel Selection	9
<i>1.3.1. Methods: Information Content Analysis</i>	9
<i>1.3.2. Channel Selection</i>	10
1.4 CO ₂ Retrievals	12
1.5 Conclusions.....	14
1.6 Acknowledgements.....	15
1.7 References.....	16
Chapter 2: Vertically Constrained CO₂ Retrievals from TCCON Measurements ...	29
Abstract.....	30
2.1 Introduction.....	31
2.2 Data and Methodology.....	35
<i>2.2.1 TCCON Data</i>	35

2.2.2 <i>Aircraft In Situ Profiles</i>	36
2.2.3 <i>Information Analysis</i>	37
2.2.4 <i>Retrieval Setting</i>	38
2.3 Profile Retrievals	40
2.3.1 <i>Synthetic Retrievals</i>	40
2.3.2 <i>Realistic Retrievals</i>	42
2.4 Channel Selections.....	45
2.4.1 <i>Synthetic Scaling Retrievals</i>	46
2.4.2 <i>Realistic Scaling Retrievals</i>	46
2.4.3 <i>Synthetic Profile Retrievals</i>	47
2.5 Conclusions.....	48
2.6 Acknowledgements.....	49
2.7 References.....	51
 Part II: Interannual Variability of the Stratospheric Quasi-Biennial	
Oscillation	70
 Chapter 3: Nonstationary Synchronization of Equatorial QBO with SAO in	
Observation and Model	71
Abstract.....	72
3.1 Introduction.....	74
3.2 QBO-SAO Synchronization: Data Analysis.....	76
3.3 QBO from THINAIR Model	80
3.3.1 <i>Model</i>	80
3.3.2 <i>Time-Varying Solar-Cycle Run</i>	81

3.3.3 <i>Perpetual Solar Forcing Runs</i>	82
3.4 A Possible Mechanism for QBO-SAO Synchronization	83
3.4.1 <i>Parametric Study</i>	86
3.5 Conclusions.....	88
3.6 Acknowledgements.....	89
3.7 References.....	90
Chapter 4: The Modulation on the Period of the Quasi-Biennial Oscillation by the Solar Cycle	102
Abstract.....	103
4.1 Introduction.....	105
4.2 Relevant Features in ERA-40 Data.....	107
4.3 Model	109
4.4 Model Solar Influence on QBO Period.....	110
4.4.1 <i>Time-Varying SC Run</i>	110
4.4.2 <i>“Perpetual” Solar Forcing Runs</i>	111
4.4.3 <i>Exaggerated, “Perpetual” Solar-Cycle Forcing</i>	112
4.5 Partition of the QBO Period into Westerly and Easterly Durations	113
4.6 Possible Mechanisms for Solar Modulation of QBO Period.....	114
4.7 Conclusions.....	118
4.8 Acknowledgements.....	120
4.9 References.....	121

List of Figures

Figure 1.1. Weighting functions for CO ₂ peak near the surface.....	20
Figure 1.2. Channels with highest IC for CO ₂ , temperature, H ₂ O and surface pressure ...	21
Figure 1.3. Channels with highest IC for CO ₂ are those with intermediate absorption.....	22
Figure 1.4. IC for CO ₂ , temperature, H ₂ O and surface pressure for 40 channels with highest CO ₂ IC	23
Figure 1.5. IC increases with the number of channels selected. The increase in IC is very little from 200 channels to 1016 (all) channels.....	24
Figure 1.6. CO ₂ retrieval comparisons.....	25
Figure 2.1. The same absorption line centered at 6243.9 cm ⁻¹ measured by OCO-2, sza = 17° and by TCCON, sza = 22.5°	56
Figure 2.2. CO ₂ band at 1.6 μm observed on June 17, 2008 by TCCON at Park Falls (Wisconsin) with solar zenith angle of 22.5°	57
Figure 2.3. Partial X _{CO₂} profile for true (black star) and mean partial X _{CO₂} of 100 retrievals.....	58
Figure 2.4. Examples of profile retrievals from the same spectrum but with three different a priori profiles.....	59
Figure 2.5. (a) Comparison of measured spectrum from TCCON and model spectrum by GFIT; (b) CO ₂ absorption line; (c) H ₂ O absorption line; (d) solar absorption line; (d) the residuals between the measured spectrum and model spectrum	60
Figure 2.6. Examples of the retrievals from the same spectrum but with three different spectra windows.....	61

Figure 3.1. Height-time cross section of the monthly mean ERA-40 zonal mean zonal wind.....	95
Figure 3.2. QBO period in ERA-40 data at 5 hPa	96
Figure 3.3. Height-time cross section of zonal mean zonal wind for the SC-varying model case.....	97
Figure 3.4. Same as figure 3.2 but for model results for the SC-varying case.	98
Figure 3.5. Height-time cross section of zonal mean zonal wind for SC-mean case	99
Figure 3.6. Histogram of the periods of the QBO for different wave forcings.....	100
Figure 4.1. Height-time cross section of the monthly mean ERA-40 zonal wind	125
Figure 4.2. QBO period in ERA-40 data at 5 hPa	126
Figure 4.3. Height-time cross-section of zonal mean zonal wind for 1×SC-vary case from year 126 to 151.5 and year 149.3 to 172.8 in two panels, respectively	127
Figure 4.4. Same as figure 4.2 but from model results for the 1×SC-vary case	128
Figure 4.5. Histogram of the QBO period, counting the number of occurrences when the QBO period is 4-SAO period and when it is 5-SAO period.....	129
Figure 4.6. Time-height cross section of the equatorial monthly-mean zonal wind component from the THINAIR model simulation.....	130
Figure 4.7. Histogram of the QBO period	131
Figure 4.8. QBO period averaged over the model run, as a function of the solar forcing, in units of SC-max	132
Figure 4.9. QBO periods as a function of years in the 400-year periodic SC run	133

List of Tables

Table 1.1. Selected channels	26
Table 1.2. Test of retrievals	27
Table 1.3. Uncertainty studies	28
Table 2.1. Information analysis for CO ₂ retrievals from TCCON and OCO-2 spectra.....	62
Table 2.2. Bias in total X _{CO₂} from realistic profile retrievals	63
Table 2.3. Same as table 2.2 but in partial X _{CO₂}	64
Table 2.4 Same as table 2.3 but on different dates. The GIT a priori profiles are applied in all the profile retrievals.	65
Table 2.5. Information analyses for selected channels	66
Table 2.6. Synthetic scaling retrieval tests for microwindow.....	67
Table 2.7. Bias in total X _{CO₂} for realistic scaling retrievals with different spectral windows	68
Table 2.8. The same as table 2.6 but for the synthetic profile retrievals and also include the biases in partial X _{CO₂}	69
Table 3.1. Parameters used to force the QBO in the THINAIR model	101

Overview

This thesis is devoted to an understanding of climate changes in the troposphere and the stratosphere from different aspects. In the troposphere, projecting future climate depends on our understanding of the exchange of CO₂ between the atmosphere, oceans, and terrestrial ecosystems. To understand the carbon cycle, it is important to estimate the sources and sinks of CO₂. The so-called inverse approach has been widely used to retrieve the abundances of atmospheric species, such as CO₂, from global surface networks and subsequently estimate their surface fluxes and variability. Understanding of the global distribution and temporal variability of atmospheric CO₂ thus helps constrain the surface carbon sources and sinks. In the stratosphere, the equatorial quasi-biennial oscillation (QBO) affects the polar stratosphere during winter, with the easterly phase of the QBO creating the condition for a more perturbed and warmer polar vortex. Therefore, the variation of the QBO period has additional significance, especially with respect to the timing of its phase relative to the Northern Hemisphere (NH) winter. The study of the interannual variability of the QBO improves our understanding of the climate system.

In this thesis, a retrieval algorithm is developed to estimate both CO₂ column abundance and its profile using radiances in the near-infrared region. In addition, the interannual variability of QBO is explored by studying both observation data and the modeled results. The thesis includes two parts. Part I (chapters 1 and 2) is a summary of the work about the CO₂ retrievals. Part II (chapters 3 and 4) is devoted to the stratospheric dynamics.

In chapter 1, a method based on the theoretical information analysis is developed and tested to select channels for the CO₂ retrievals from OCO-like measurements. It tests the effectiveness of retrievals using fewer channels. Besides speeding up the retrieval process, channel selection can minimize errors due to uncertainties in other parameters such as temperature and surface pressure.

In chapter 2, the CO₂ profile retrieval from a ground-based Fourier Transfer Spectrometer (FTS) instrumentation is studied. The retrieved vertical CO₂ profiles are compared with scaling retrievals and are validated by aircraft measurements. The method of channel selection is applied to the retrievals from the real measurements from ground-based FTS spectra.

The synchronization of stratospheric QBO with the semiannual oscillations (SAO) in the mesosphere is discussed in chapter 3. Both in observations and modeling data, the period of QBO is found to be a multiple of six months. This confirms that the synchronization is not just a tendency but also a robust phenomenon in the upper stratosphere. The nonstationary behavior of synchronization is not caused by the 11-year solar-cycle forcing, but is instead caused by the incompatibility of the QBO's natural period determined by its wave forcing, and the "quantized" period determined by the SAO.

In chapter 4, the mechanism of solar-cycle modulation of the QBO period is examined using a two-and-half-dimensional THINAIR model. In contrast to the previous work, we find the mean QBO period increases with the solar forcing.

Part I:
Retrieval of Atmospheric Carbon Dioxide from
High-Resolution Spectra

Chapter 1: Channel Selection Using Information Content Analysis: A Case Study of CO₂ Retrieval from Near-Infrared Measurements

Le Kuai¹, Vijay Natraj², Run-Lie Shia¹, Charles Miller², Yuk L. Yung¹

1. Division of Geological and Planetary Sciences, California Institute of Technology

2. Jet Propulsion Laboratory, California Institute of Technology

(Kuai, L., et al., 2010: Channel selection using information content analysis: A case study of CO₂ retrieval from near infrared measurements. *J Quant. Spectrosc. Radiat. Transfer.*, **111**, 1296–1304.)

Abstract

A major challenge in retrieving CO₂ concentrations from thermal infrared remote sensing comes from the fact that measurements in the 4.3 and 15 μm absorption bands (AIRS or TES) are sensitive to both temperature and CO₂ variations. This complicates the selection of absorption channels with maximum CO₂ concentration information content. In contrast, retrievals using near infrared (NIR) CO₂ absorption bands are relatively insensitive to temperature and are most sensitive to changes of CO₂ near the surface, where the sources and sinks are located. The Orbiting Carbon Observatory (OCO) was built to measure reflected sunlight in three NIR spectral regions (the 0.76 μm O₂ A-band and two CO₂ bands at 1.61 and 2.06 μm). In an effort to significantly increase the speed of accurate CO₂ retrieval algorithms for OCO-2, we performed an information content analysis to identify the 20 best channels from each CO₂ spectral region to use in retrievals. Retrievals using these 40 channels provide as much as 75% of the total CO₂ information content compared to retrievals using all 1016 channels in each spectral region. The CO₂ retrievals using our selected channels have a precision better than 0.1 ppm. This technique can be applied to the retrievals of other geophysical variables (e.g., temperature or CH₄), or modified for other instruments, such as AIRS, TES or TCCON.

1.1 Introduction

Understanding changes in the concentrations, global sources and sinks, dynamics and other processes that control the variability of atmospheric carbon dioxide (CO₂) has emerged as one of the principal challenges of 21st century Earth system science. Since ground-based measurements are sparse over the ocean, in the tropics and elsewhere in the developing world, satellite observations of atmospheric CO₂ are poised to revolutionize our understanding of global carbon cycle by providing unprecedented spatiotemporal resolution and coverage.

Carbon dioxide is one of the most important greenhouse gases, and the rapid increase in its concentration due to the anthropogenic sources in the atmosphere has great impact on the climate. The anthropogenic sources of CO₂ include fossil fuel combustion and other human activities. The natural sinks are the oceans and terrestrial plants. A better understanding of these sources and sinks is required to improve CO₂ flux estimates.

TCCON is a network of ground-based Fourier Transform Spectrometers recording direct solar light in the near-infrared spectral region. The precise measurements of CO₂ column abundance, e.g., over Park Falls, Wisconsin and Lauder, New Zealand (<http://www.tcon.caltech.edu/>) (Washenfelder et al. 2006), provide an essential validation resource for space-based estimation such as from the Atmospheric Infrared Sounder (AIRS) (Chahine et al. 2005, 2008), the Tropospheric Emission Spectrometer (TES) (Kulawik et al. 2010), the Infrared Atmospheric Sounding Interferometer (IASI)

(Crevoisier et al. 2009), the Scanning Imaging Absorption Spectrometer for Atmospheric Chartography (SCIAMACHY) (Bosch et al. 2006; Buchwitz et al. 2005, 2007), the Orbiting Carbon Observatory (OCO) (Crisp et al. 2004), and the Greenhouse gases Observing SATellite (GOSAT) (Sato et al. 2009; Yokomizo 2008; Yokota et al. 2009).

Rayner and O'Brien (2001) showed that space-based measurements could improve CO₂ flux estimates provided the measurements have a precision of better than about 2 ppm ppm (parts per million) on regional scales. The observations from the thermal emission instruments such as AIRS, TES, and IASI have improved our understanding of the CO₂ seasonal variability and its spatial distributions in the mid latitudes and tropics. These thermal infrared (TIR) observations have CO₂ weighting functions that peak in the middle and upper troposphere (Chahine et al. 2005; Kulawik et al. 2010). However, the near infrared (NIR) CO₂ measurements are very sensitive to the CO₂ near the surface (figure 1.1), where most of its sources and sinks are present (Kuang et al. 2002). Therefore, CO₂ retrieval using NIR measurements should improve the estimation of global CO₂ sources and sinks and provide complementary information to that from TIR estimations. It was found that a +0.1 K temperature error resulted in a +2.5 ppm CO₂ error in the TIR band retrievals (Kulawik et al. 2010). However, the temperature uncertainty-induced CO₂ errors are much smaller in the NIR band retrievals. The target precision of the CO₂ column measurements from an OCO-like instrument is about 1 ppm for a single sounding on regional scales and monthly timescales (Miller et al. 2007).

For the first time, two satellites dedicated to CO₂ observations were launched in 2009—unfortunately, the NASA OCO experienced a launch failure. The JAXA GOSAT is providing space-based measurements in both NIR and TIR spectral regions. Both AIRS and TES provide measurements of the TIR CO₂ band at 15 μm. In addition, TES also uses two laser bands at 967 – 990 and 1070 – 1117 cm⁻¹ for CO₂ retrieval (Kulawik et al. 2010). An OCO-like instrument will measure the O₂ *A* band (0.76 μm), the CO₂ band at 1.61 μm and the CO₂ band at 2.06 μm. The GOSAT Fourier Transfer Spectrometer (FTS) covers a wide spectral range (0.76 – 15 μm).

One of the major challenges to fast and accurate retrievals is the choice of channels used for the retrieval. We could of course use all the channels and retrieve all the parameters simultaneously. However, this results in complicated and slow retrievals. Further, it is very hard to eliminate biases due to correlations between the parameters. Clarmann and Echle discussed the selection of the optimum microwindows with respect to their associated retrieval errors (Clarmann et al. 2001). The sources of retrieval errors are random errors of the measurement, and errors of the forward model and its input parameters. One goal of channel selection is to make an optimum trade-off between random measurement errors and systematic errors. Adding more channels usually decreases random measurement errors but increases the systematic errors.

There has been some work on the optimization of retrievals from high spectral resolution measurements on the basis of information content (IC) analysis. Most of the earlier work has focused on choosing microwindows for retrieving temperature, humidity and other

geophysical parameters. For example, Clarmann et al. (2001) and Dudhia et al. (2002) developed the microwindow selection method for the Michelson Interferometer Passive Atmospheric Sounding (MIPAS) measurement; Chédin et al., (2003) and Crevoisier et al. (2003) used channel selection for CO₂ retrieval from AIRS spectra; Sofieva and Kyrölä (2003) described channel selection for GOMOS measurements, Worden et al. (2004) for TES, and Saitoh et al. (2009) for GOSAT.

The selection of optimized microwindows by Clarmann et al. (2001) was applied to N₂O microwindows for measurements made by a Fourier transform spectrometer. Another practical application of the microwindow selection that maximizes IC was demonstrated for the retrieval of methane profiles from MIPAS measurements by Dudhia et al. (2002). Crevoisier et al. (2003) extended the methods to reduce the number of channels for the retrieval of CO₂ and other trace gases from AIRS. They compared a new method, the Optimal Sensitivity Profile (OSP) method, with other methods based on IC and degrees of freedom (DOF) analysis and concluded that using the OSP method optimized the choice of channels for AIRS retrievals of CO₂ and other trace gases. The methods for the selection of measurement subsets using information theory were also examined by Sofieva and Kyrölä (2003). They developed a sequential deselecting procedure and proposed a fast algorithm for channel selection. These methods were applied to the selection of the most informative spectral channels for GOMOS measurements. GOMOS is a stellar occultation instrument for UV-visible spectra. Saitoh et al. (2009) developed an algorithm to retrieve CO₂ vertical profiles from the 15 μm band (700 – 800 cm⁻¹) for GOSAT (Saitoh et al. 2009). They showed that separately selecting a subset of channels

based on CO₂ IC for three vertical regions provided retrieval results equivalent to those using all channels in the 15 μm band. However, none of these studies considered the selection of CO₂ channels in the NIR. Our objective is to develop a general technique for channel selection using information analysis (Rodgers 1996).

In this chapter, we discuss the channel selection for retrieving the column abundance of CO₂ based on IC analysis. Nothing, however, precludes the use of this technique for retrieving any other geophysical parameter. Section 2 describes the forward model used for the radiative transfer simulations. Section 3 gives an introduction to the concepts of IC and DOF, and describes the channel selection technique. We compare a retrieval using the selected channels to one using all channels in section 4. In section 5, we derive some conclusions from our preliminary study and discuss the practical advantages of this technique.

1.2 Model

The radiances are computed using the OCO Orbit Simulator (O'Brien et al. 2009), which simulates a single orbit of an OCO-like instrument. The meteorological and cloud profiles are drawn from a static database of ECMWF profiles (Chevallier 2001). The surface properties are taken from MODIS, and the CO₂ profiles are obtained from the Parameterized Chemical Transport Model (Kawa et al. 2004). The gas absorption cross sections are taken from HITRAN 2004 (Rothman et al. 2005) with CO₂ line updates from 4300 to 7000 cm⁻¹ provided by the work of Toth et al., (2008). This is done on a 0.01

cm⁻¹ spacing high-resolution grid, which resolves individual O₂ or CO₂ lines in the near infrared with a minimum of two points per Doppler width (Bosch et al. 2006). The Rayleigh scattering properties are computed using the model of Bodhaine et al. (1999). The intensity and polarization calculations are performed using the successive orders of interaction (Bodhaine et al. 1999) and the two orders of scattering (Natraj and Spurr 2007) models respectively. The radiative transfer computation time is dramatically improved using a low-streams interpolation technique (O'Dell 2010). The solar model (Bosch et al. 2006) employs an empirical list of solar line parameters as well as a model for the solar continuum. The Jacobians are computed using finite differences (figure 1.1).

1.3 Channel Selection

1.3.1. Methods: Information Content Analysis

We apply information content analysis to choose channels that have the most information content for CO₂ and are at the same time insensitive to other parameters such as temperature, water vapor and surface pressure. In retrieval theory, there are two useful quantities that provide a measure of the information. Degrees of freedom indicate the number of useful independent quantities in a measurement (Rodgers 2000). The Shannon information content is a scalar quantity that is defined qualitatively as the factor (in bits) by which knowledge of a quantity is improved by making the measurement (Crevoisier et al. 2003). The following equations show the relationship between information content (H), degrees of freedom (d_s), the singular values (λ_i) of the normalized Jacobian matrix (\tilde{K}) and the averaging kernel matrix (A) (Rodgers 2000).

$$\tilde{K} = S_{\xi}^{-\frac{1}{2}} K S_a^{-\frac{1}{2}}, \quad (1.1)$$

$$I_n - A = (K^T S_{\xi}^{-1} K + S_a^{-1}) S_a^{-1} = \hat{S} S_a^{-1}, \quad (1.2)$$

$$H = \frac{1}{2} \sum_i \ln(1 + \lambda_i^2) = -\frac{1}{2} \ln |I_n - A|, \quad (1.3)$$

$$d_s = \sum_i \lambda_i^2 / (1 + \lambda_i^2) = \text{tr}(A), \quad (1.4)$$

where S_a is the covariance matrix for *a priori* and S_{ξ} is the measurement error covariance matrix.

1.3.2. Channel Selection

First, we apply IC analysis to each channel to determine the DOF and IC for CO₂. Then the channels (in each band) are ranked in decreasing order of IC. It is found that the channels with high IC for CO₂ are those with intermediate absorption (figure 1.2). This is because, for very weak channels, there is too little CO₂ absorption to give a useful signal, while for the saturated channels, the absorption is too high to have any sensitivity to the CO₂ concentration. We apply the same procedure for other parameters, such as temperature, water vapor and surface pressure, and then rank the channels in a similar fashion. The 20 channels with highest IC for CO₂, temperature, water vapor and surface pressure are plotted respectively in figure 1.2. The O₂ A-band channels are only sensitive to temperature and pressure. Figure 1.2 also shows that the channels with high IC for CO₂ are mostly different from those for temperature, water vapor and surface pressure.

The order of the channels (in terms of IC) for clear sky is very similar for high aerosol optical depth (AOD) and high cloud optical depth (COD) scenarios. This implies that the channel selection procedure is robust and could be applied to retrieval under different scenarios. It is evident that more channels have DOF close to 1 in the high AOD scenario (see last four panels of figure 1.3). This is probably due to backscattering by aerosols.

Figure 1.4 shows the 40 channels (20 each in the 1.61 and 2.06 μm CO_2 bands) with highest IC for CO_2 and the corresponding IC for temperature, water vapor and surface pressure. Most of the channels have high IC for CO_2 and surface pressure but low IC for temperature and water vapor. We use the following procedure to choose the channels for CO_2 retrieval. First, channels with CO_2 IC more than 0.8 bits are selected. Within the selected channels, those that have more than 0.2 bits temperature IC are removed. Among the remaining channels, 40 (20 each in the 1.61 and 2.06 μm CO_2 bands) that have least sensitivity to surface pressure and water vapor are selected for the CO_2 retrievals (see table 1.1 for a list of chosen channels).

A simultaneous retrieval using all 2032 channels in both the 1.61 μm and 2.06 μm CO_2 bands provides 1.67 DOF and 5.9 bits of IC. Figure 1.5 shows that a retrieval using the first 200 channels (ranked in order of decreasing IC) in each band would have 1.55 DOF and 5.35 bits of IC. This represents about 90% of the IC provided by a retrieval using all channels. If we use just the top 20 channels in each band, we still retain around 75% of the IC.

1.4 CO₂ Retrievals

For the retrieval study, we assume a constant CO₂ concentration of 370. The signal to noise ratio (SNR) is set to be 300 for all channels. This is a reasonable value for an OCO-like instrument. The (constant) a priori and initial guess for CO₂ are set at 375 ppmv and 380 ppmv respectively. The diagonal values of the a priori covariance matrix are set to be 1% of the initial value. The off diagonal elements are calculated assuming exponential decay with a scale height of 8 km (Rodgers 2000).

In the lower atmosphere, the temperature, water vapor, and aerosol profiles are well determined by the measurement; they are strongly constrained by the a priori at higher altitudes (Connor et al. 2008). With this in mind, we retrieve the CO₂ concentrations at seven levels between 2 and 5 km, where we expect maximum sensitivity from NIR measurements. Table 1.2 shows the retrieval results for 6 cases. Case 1 is the ideal case where the measurements have no random noise. The column averaged dry air mole fraction of CO₂ (X_{CO_2}) from a full-channel retrieval is 370.007 ppmv, in excellent agreement with the true X_{CO_2} . Case 2 is the same as case 1 except that random noise has been added to the pseudomeasured spectrum. Case 3 considers what happens if we average 100 retrievals with different sets of random noise. This is to simulate a retrieval of several contiguous soundings from real space-based measurements. The X_{CO_2} accuracy is comparable to the case with no noise. Case 4–6 are the same as cases 1–3 except that we use only the 40 channels selected by IC analysis. In the case with no random noise, the X_{CO_2} accuracy is 0.048 ppmv (case 4). The accuracy when we average 100 retrievals

with different random noise (case 6) is only 0.057 ppmv, which is comparable to case 4. Figure 1.6 shows very good agreement between the retrieved CO₂ profiles and the truth.

In the above study, CO₂ is the only unknown parameter. The other atmospheric variables are assumed to be perfectly known. However, in a real retrieval, uncertainties in these atmospheric parameters would introduce a bias in the CO₂ retrieval. For the purposes of this work we only consider the clear sky scenario; cloudy scenarios will be discussed in a subsequent chapter. A 1 K uncertainty in the temperature profile resulted in a 0.5 ppmv bias in the retrieved XCO₂. A similar 10 hPa perturbation to the surface pressure or 1% uncertainty in the water vapor profile caused a similar XCO₂ bias (table 1.3).

For the realistic retrievals, before retrieving the CO₂ using these 40 channels, one or more channels need to be selected for retrieving the zero level as well as other channels for retrieving the continuum level. Zero-level offsets are caused by the incorrect calculations of the depth of the absorption lines in the forward model. This will contribute to the errors in retrieved XCO₂. Those channels for zero level should have the strongest CO₂ absorption and be saturated. In contrast, those channels selected for continuum level should have low absorption by any gas and be away from the solar signatures. A linear continuum level is a good assumption for narrow spectral window. The continuum tilt will be retrieved at the same time. In the case of continuum level with significant curvature, a polynomial fit will be required. Retrieval of the continuum level allows us to convert radiance to transmittance or reflectance.

In order to minimize the systematic errors from the uncertainties in other parameters, the channels should be selected individually for temperature, surface pressure and water vapor using the information analysis. First of all, the temperature will be retrieved with selected channels that are more sensitive to temperature but less sensitive to other parameters. The retrieved temperature will be used in the retrieval of surface pressure with different selected channels for surface pressure. Next, both the retrieved temperature and surface pressure will be used in the retrieval of water vapor using its selected channels. Finally, CO₂ will be retrieved using retrieved temperature, surface pressure and water vapor and using above 40 channels. The iteration will start over again to retrieve temperature by using previous retrieved values of CO₂, surface pressure and water vapor. We anticipate that this process of iterative retrievals will efficiently reduce the effect of uncertainties in the other three parameters on the final retrieval of CO₂.

1.5 Conclusions

OCO-like instruments typically have thousands of detector channels. However, it is unnecessary to use all the channels to retrieve CO₂ since only some of them are sensitive to CO₂. Further, many channels are sensitive to other variables such as temperature and surface pressure. We have developed a technique based on IC analysis to select channels for CO₂ retrievals using NIR measurements. It was found that the channels with high CO₂ IC are those with intermediate absorption. We selected 40 channels with high sensitivity to CO₂ and low sensitivity to other parameters. The channel selection was

found to be independent of the scattering scenario (clear vs. cloudy sky). Retrieval using the 40 channels was also shown to retain 75% IC.

Retrievals using the selected channels have comparable error characteristics to the all-channel retrievals. The accuracy of the 40-channel retrieval after averaging over several pseudosoundings is about 0.05 ppmv. Even with the uncertainties of 1 K in temperature, 10 hPa in surface pressure, or 1% in water vapor, the X_{CO_2} bias would be about 0.5 ppmv.

The same technique can be applied to select channels most sensitive to T, surface pressure, water vapor or any other parameter. In this way, it is possible to retrieve them one by one. This introduces the possibility of an iterative retrieval to account for uncertainties in relevant geophysical parameters. The channel selection technique allows us to use optimal sets of channels to retrieve atmospheric variables. We intend to apply this method to CO_2 retrievals from GOSAT measurements.

1.6 Acknowledgements

This research is supported by the Orbiting Carbon Observatory (OCO) project, a NASA Earth System Science Pathfinder (ESSP) mission. The authors would like to thank Denis O'Brien, Igor Polonsky and Chris O'Dell from Colorado State University for providing us the orbit simulator code and for helping with its development and maintenance, and James McDuffie from the Jet Propulsion Laboratory (JPL) for providing covariance information.

1.7 References

- Bodhaine, B. A., et al., 1999. On Rayleigh optical depth calculations. *J. Atmos. Oceanic Technol.*, **16**, 1854–1861.
- Bosch, H., et al., 2006. Space-based near-infrared CO₂ measurements: Testing the Orbiting Carbon Observatory retrieval algorithm and validation concept using SCIAMACHY observations over Park Falls, Wisconsin. *J. of Geophys. Res. — Atmos.*, **111**, D23302, doi:23310.21029/22006jd007080.
- Buchwitz, M., et al., 2005. Atmospheric methane and carbon dioxide from SCIAMACHY satellite data: initial comparison with chemistry and transport models. *Atmos. Chem. Phys.*, **5**, 941–962.
- , 2007. First direct observation of the atmospheric CO₂ year-to-year increase from space. *Atmos. Chem. Phys.*, **7**, 4249–4256.
- Chahine, M. T., et al., 2005. On the determination of atmospheric minor gases by the method of vanishing partial derivatives with application to CO₂. *Geophys. Res. Lett.*, **32**, L22803, doi:22810.21029/22005gl024165.
- , 2008. Satellite remote sounding of mid-tropospheric CO₂. *Geophys. Res. Lett.*, **35**, L17807, doi:17810.11029/12008gl035022.
- Chédin, A., et al., 2003. The feasibility of monitoring CO₂ from high-resolution infrared sounders. *J. Geophys. Res.—Atmos.*, **108**, art. no.—4064.
- Chevallier, F., 2001. Sampled databases of 60-level atmospheric profiles from the ECMWF analyses. *SAF Programme Research Report 4, EUMETSAT/ECMWF, Am Kavalleriesand*, **31**, Postfach D–64297 Darmstadt, Germany.

- Clarmann, T. V., et al., 2001. Optimized microwindows in atmospheric spectroscopy. *Hyperspectral Remote Sensing of the Land and Atmosphere*, W. L. Smith, and Y. Yasuoka, editors., 135–142.
- Connor, B. J., et al., 2008. Orbiting carbon observatory: Inverse method and prospective error analysis. *J. Geophys. Res. — Atmos.*, **113**, D05305, doi: 10.1029/2006jd008336.
- Crevoisier, C., et al., 2003. AIRS channel selection for CO₂ and other trace-gas retrievals. *Q. J. R. Meteorol. Soc.*, **129**, 2719–2740.
- , 2009. First year of upper tropospheric integrated content of CO₂ from IASI hyperspectral infrared observations. *Atmos. Chem. Phys.*, **9**, 4797–4810.
- Crisp, D., et al., 2004. The Orbiting Carbon Observatory (OCO) mission. *Adv. Space Res.*, **34**, 700–709.
- Dudhia, A., et al., 2002. Microwindow selection for high-spectral-resolution sounders. *Appl. Opt.*, **41**, 3665–3673.
- Kawa, S. R., et al., 2004. Global CO₂ transport simulations using meteorological data from the NASA data assimilation system. *J. Geophys. Res. — Atmos.*, **109**, D18312, doi:10.1029/2004jd004554.
- Kuang, Z. M., J. Margolis, G. Toon, D. Crisp, and Y.L. Yung, 2002. Spaceborne measurements of atmospheric CO₂ by high-resolution NIR spectrometry of reflected sunlight: an introductory study. *Geophys. Res. Lett.*, **29**, 1716–1719.
- Kulawik, S., et al., 2010. Characterization of tropospheric emission spectrometer (TES) CO₂ for carbon cycle science. *Atmos. Chem. Phys.*, **10**, 5601–5623.

- Miller, C. E., et al., 2007. Precision requirements for space-based X-CO₂ data. *J. Geophys. Res. — Atmos.*, **112**, D10314, doi: 10.1029/2006jd007659.
- Natraj, V., and R. J. D. Spurr, 2007. A fast linearized pseudospherical two orders of scattering model to account for polarization in vertically inhomogeneous scattering-absorbing media. *J. Quant. Spectrosc. Radiat. Transfer*, **107**, 263–293.
- O'Brien, D., Polonsky I, O.Dell CW., 2009. The OCO simulator. Technical Report. Cooperative Institute for Research in the Atmosphere, Fort Collins, CO, in preparation.
- O'Dell, C. W., 2010. Acceleration of multiple-scattering, hyperspectral radiative transfer calculations via low-streams interpolation. *J. Geophys. Res. — Atmos.*, **115**, D10206, doi: 10.1029/2009jd012803.
- Rayner, P. J., and D.M. O'Brien, 2001. The utility of remotely sensed CO₂ concentration data in surface source inversions. *Geophys. Res. Lett.*, **28**, 175–178.
- Rodgers, C. D., 1996. Information content and optimisation of high spectral resolution measurements. *Optical Spectroscopic Techniques and Instrumentation for Atmospheric and Space Research II*, P. B. Hays, and J. X. Wang, editors, 136–147.
- , 2000. *Inverse Methods for Atmospheric Sounding: Theory and Practice.*: World Scientific, 256 pp.
- Rothman, L. S., et al., 2005. The HITRAN 2004 molecular spectroscopic database. *J. Quant. Spectrosc. Radiat. Transfer*, **96**, 139–204.
- Saitoh, N., et al., 2009. CO₂ retrieval algorithm for the thermal infrared spectra of the greenhouse gases observing satellite: Potential of retrieving CO₂ vertical profile

- from high-resolution FTS sensor. *J. Geophys. Res. — Atmos.*, **114**, D17305, 17316 PP., doi:17310.11029/12008JD011500.
- Sato, M., et al., 2009. FIP's environmentally conscious solutions and GOSAT. *Fujitsu. Sci. Tech. J.*, **45**, 134–140.
- Sofieva, V. F., and E. Kyrölä, 2003. Information approach to optimal selection of spectral channels. *J. Geophys. Res. — Atmos.*, **108**, 4513, doi:4510.1029/ 2002jd002980.
- Toth, R. A., et al., 2008. Spectroscopic database of CO₂ line parameters: 4300–7000 cm⁻¹. *J. Quant. Spectrosc. Radiat. Transfer*, **109**, 906–921.
- Washenfelder, R. A., et al., 2006. Carbon dioxide column abundances at the Wisconsin Tall Tower site. *J. Geophys. Res. — Atmos.*, **111**, D22305, doi: 22310.21029/ 22006jd007154.
- Worden, J., et al., 2004. Predicted errors of tropospheric emission spectrometer nadir retrievals from spectral window selection. *J. Geophys. Res. — Atmos.*, **109**, D09308, doi: 09310.01029/ 02004jd004522.
- Yokomizo, M., 2008. Greenhouse gases observing Satellite (GOSAT) Ground Systems. *Fujitsu. Sci. Tech. J.*, **44**, 410–+.
- Yokota, T., et al., 2009. Global concentrations of CO₂ and CH₄ retrieved from GOSAT: First preliminary results. *Sola*, **5**, 160–163.

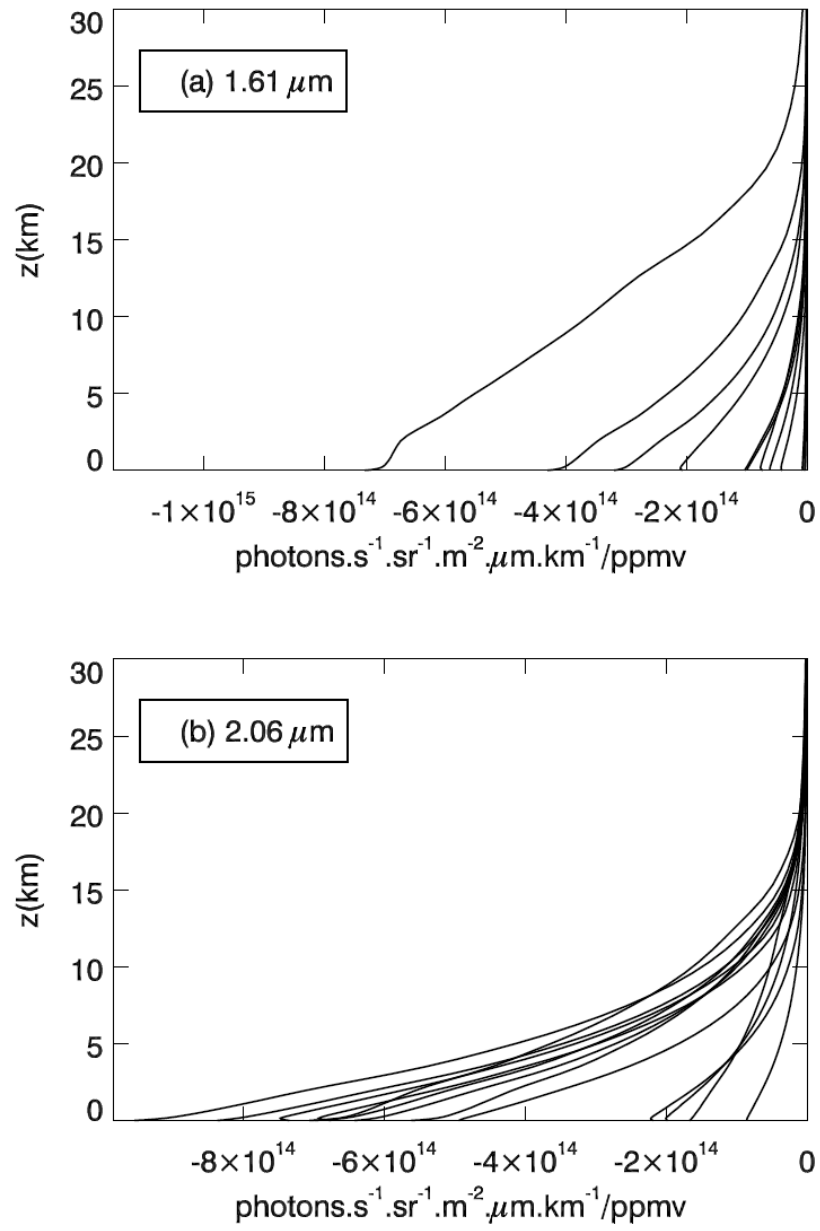


Figure 1.1. Weighting functions for CO₂ peak near the surface. (a) 1.61 μm CO₂ band; (b) 2.06 μm CO₂ band.

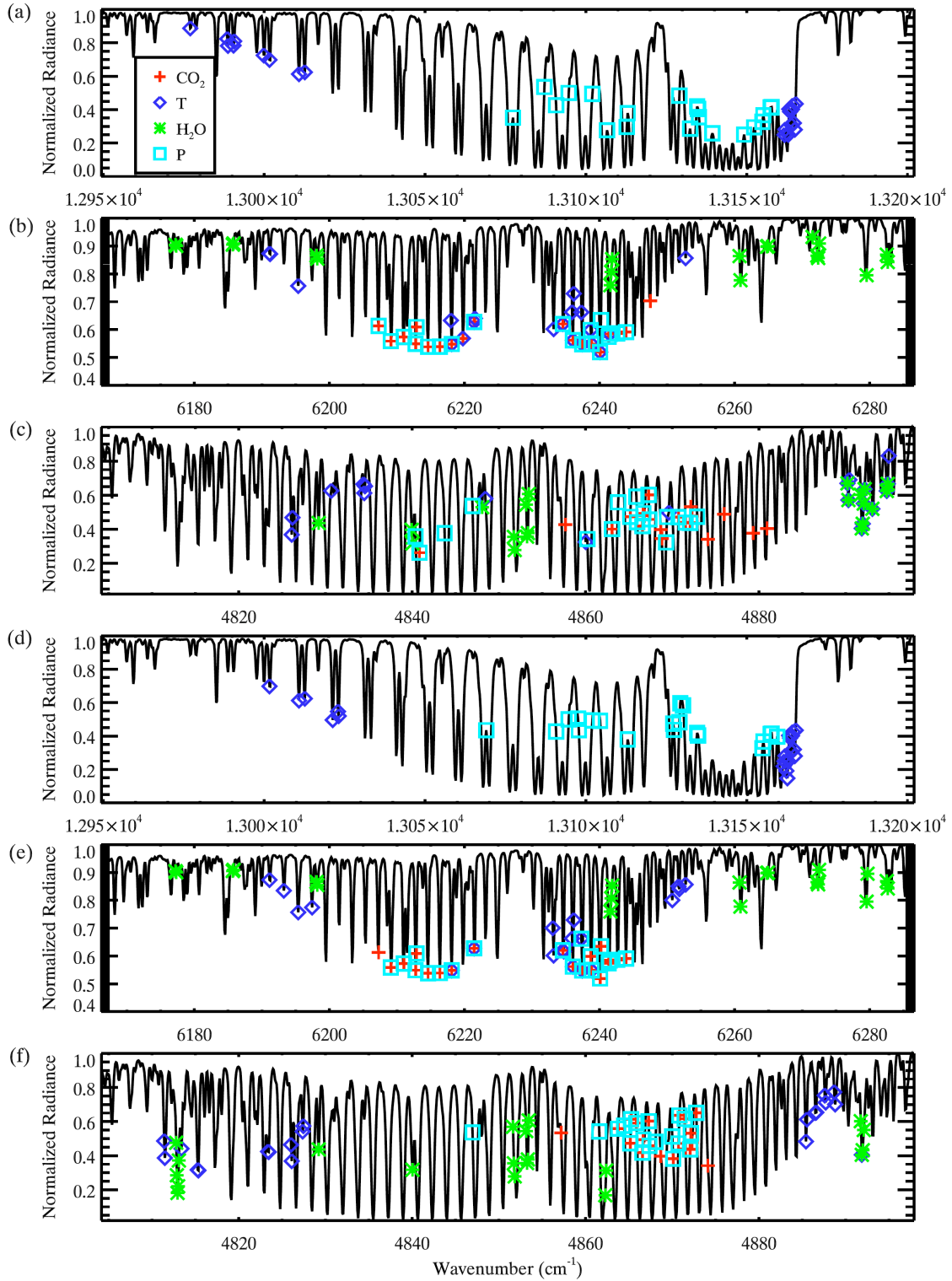


Figure 1.2. Channels with highest IC for CO₂ (cross), temperature (diamond), H₂O (star) and surface pressure (square). (a–c) clear sky scenario; (d–f) cloudy sky scenario.

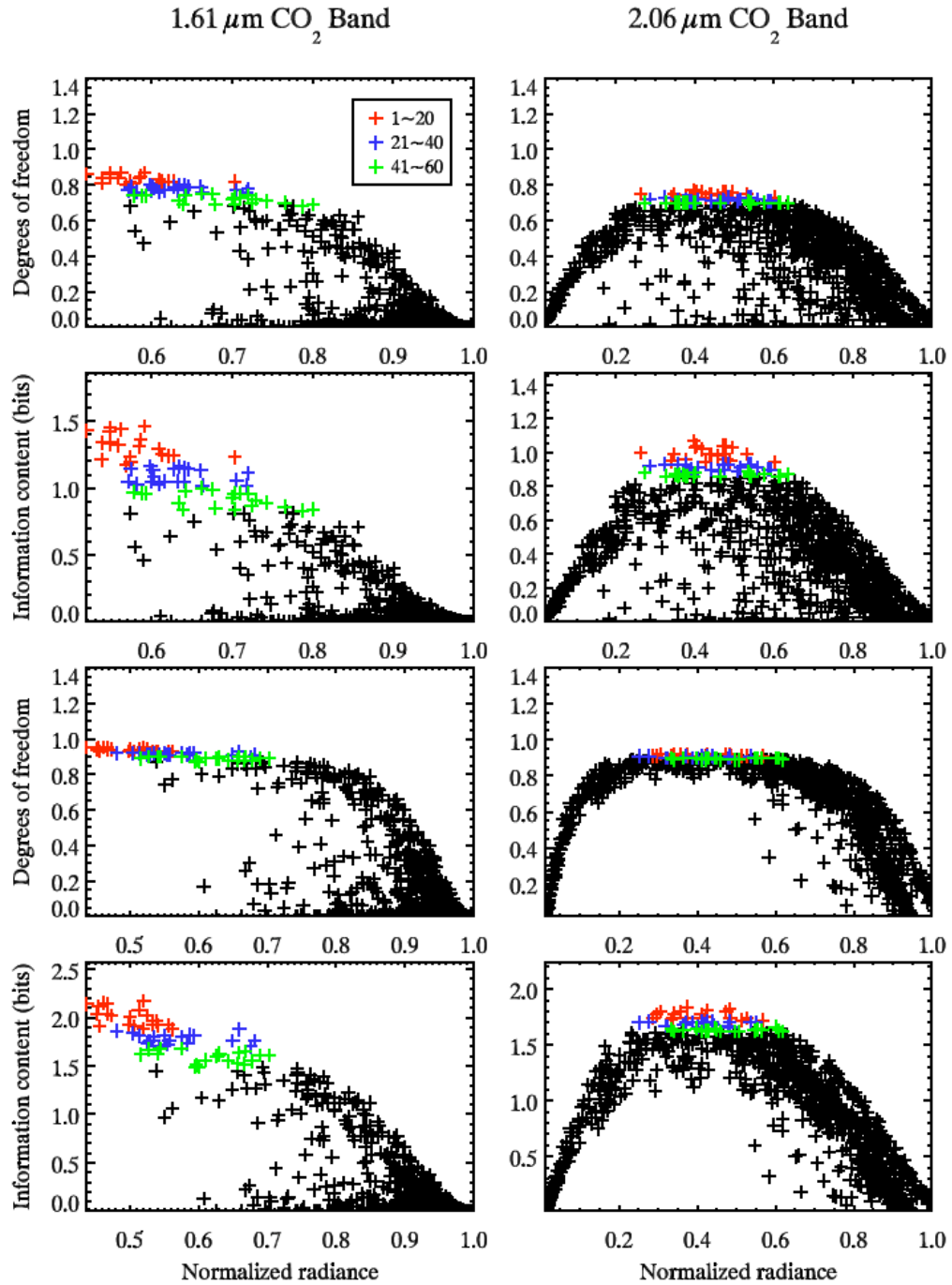


Figure 1.3. Channels with highest IC for CO₂ are those with intermediate absorption. (red) channels ranked 1–20; (blue) channels ranked 21–40; (green) channels ranked 41–60. (top 4) clear sky scenario; (bottom 4) cloudy sky scenario; (left column) 1.61 μm band; (right column) 2.06 μm band.

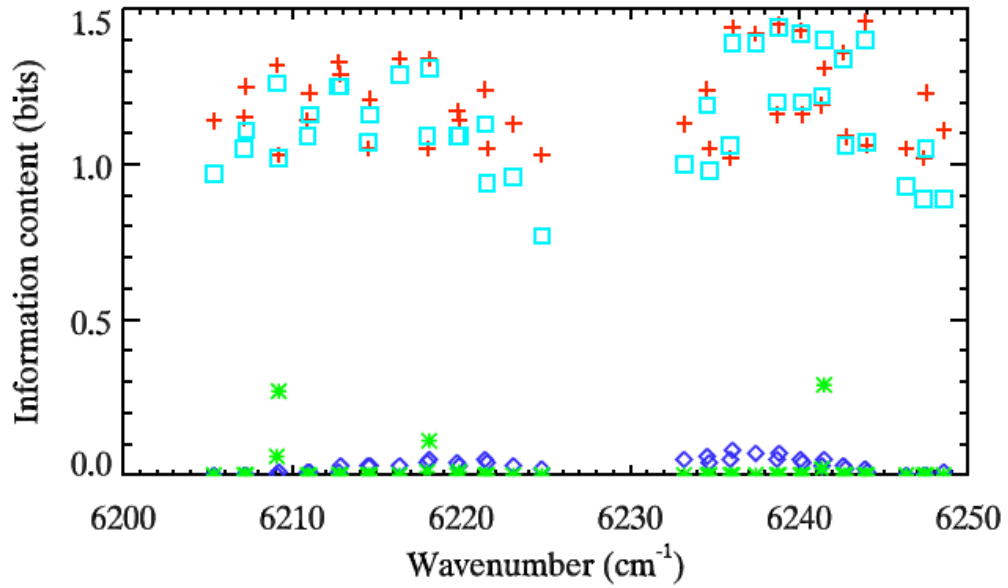
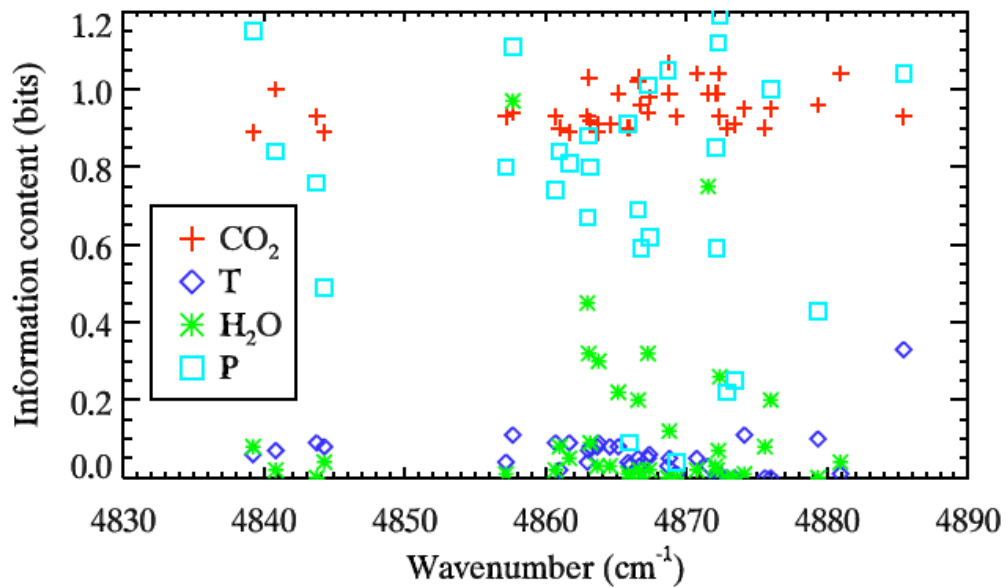
1.61 μm CO_2 Band2.06 μm CO_2 Band

Figure 1.4. IC for (cross) CO_2 ; (diamond) temperature; (asterisk) H_2O ; (square) surface pressure for 40 channels with highest CO_2 IC.

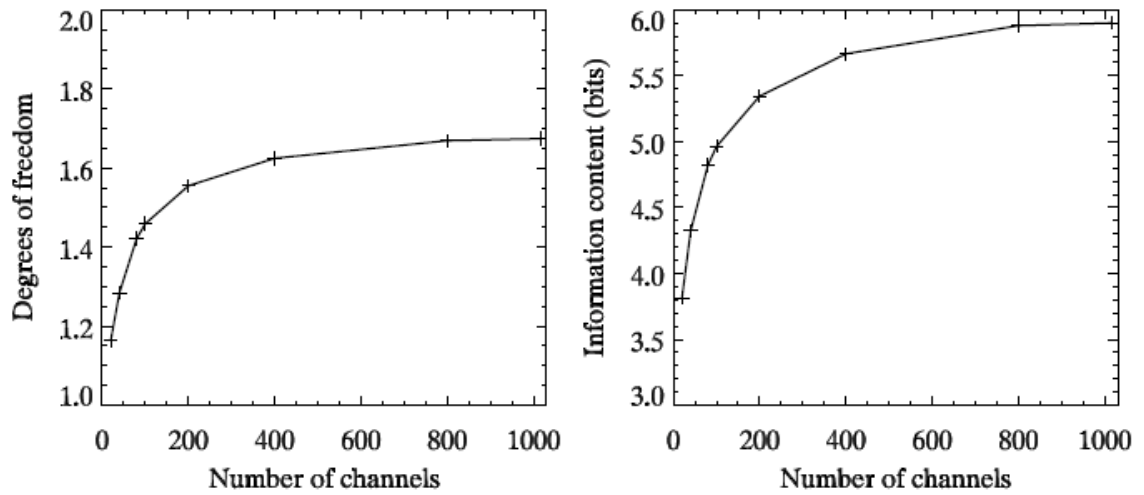


Figure 1.5. IC increases with the number of channels selected. The increase in IC is very little from 200 channels to 1016 (all) channels.

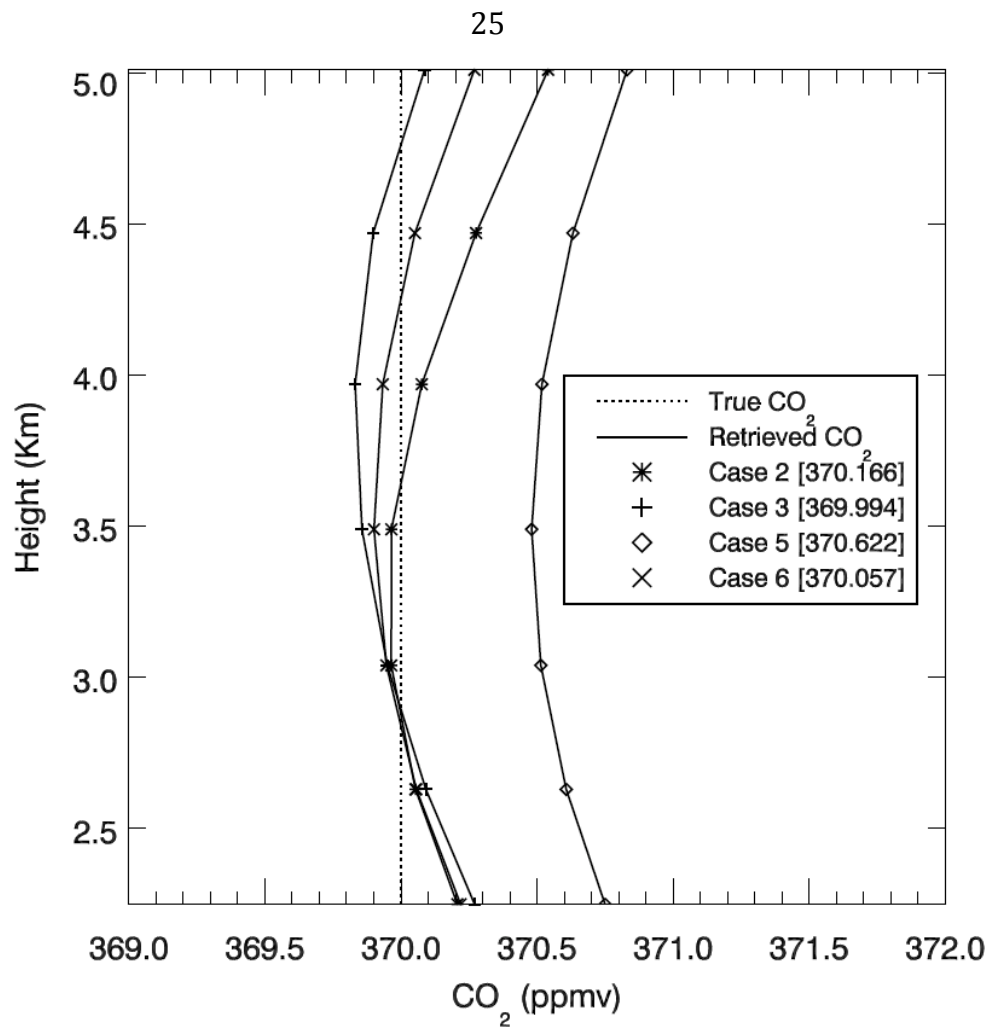


Figure 1.6 CO₂ retrieval comparisons. Case 2: All channel retrieval. Case 3: Average of 100 all-channel retrievals. Case 5: 40-channel retrieval. Case 6: Average of 100 40-channel retrievals. The a priori is 375 ppm (constant) for all cases. Random noise is included in the pseudomeasurements.

Table 1.1. Selected channels

1.61 μm (cm^{-1})	2.06 μm (cm^{-1})
6212.76	4872.26
6209.1	4880.93
6207.28	4872.05
6211.04	4872.15
6247.51	4875.98
6207.17	4869.29
6205.37	4872.36
6210.92	4873.39
6248.55	4872.88
6244.03	4875.57
6246.34	4832.21
6209.21	4874.63
6247.38	4874.74
6205.26	4874.01
6216.24	4842.02
6245.18	4878.08
6212.64	4872.77
6245.06	4895.52
6203.48	4875.46
6243.77	4876.09

Table 1.2. Test of retrievals

Case	Random noise	Channels	ΔXCO_2 (ppmv)
Case 1	No	2032	0.01
Case 2	Yes	2032	0.17
Case 3	Yes (averaging 100 cases)	2032	-0.01
Case 4	No	40	0.05
Case 5	Yes	40	0.62
Case 6	Yes (averaging 100 cases)	40	0.06

Table 1.3. Uncertainty studies

	Uncertainty	Bias in XCO ₂ (ppmv)
Temperature	1 K	0.46
Surface pressure	10 hPa	0.55
Water vapor	1%	0.44

Chapter 2: Vertically Constrained CO₂ Retrievals from TCCON Measurements

Le Kuai¹, Brian Connor², Debra Wunch¹, Gretchen Keppel Aleks¹, Run-Lie Shia¹,
Charles Miller³, Geoffrey Toon³, Paul Wennberg¹ and Yuk Yung¹

1. Division of Geological and Planetary Sciences, California Institute of Technology,
MC: 150-21, Pasadena, CA, 91125, USA. E-mail: kl@gps.caltech.edu
2. BC Consulting Ltd., 6 Fairway Dr, Alexandra 9320, New Zealand
3. Jet Propulsion Laboratory, California Institute of Technology

(To be submitted to *J. Geophys. Res.*)

Abstract

Partial column-averaged CO₂ at three tropospheric layers has been retrieved from the Total Carbon Column Observing Network (TCCON) measurements in the 1.6 μm CO₂ absorption band. Information analysis suggests that a measurement with ~60 absorption lines may provide three or more pieces of independent information, depending on the signal-to-noise ratio and solar zenith angle. This has been confirmed by retrievals based on synthetic data. Realistic retrievals of total and partial column-averaged CO₂ over Park Falls, Wisconsin on July 12, 2004, agree with aircraft measurements. Furthermore, the total column averages are always underestimated by less than 1%. The results above provide a basis for CO₂ profile retrievals using ground-based observations in the near-infrared region. It is shown that retrievals using fewer absorption lines may also obtain results with comparable accuracies, although it highly depends on the selection as well as the number of absorption lines. This may help optimize the computational expenses for retrievals from a large number of measured spectral lines.

2.1 Introduction

Remote sensing observations improve our understanding of the spatial and temporal distributions of carbon dioxide (CO_2) in the atmosphere. Total Carbon Column Observing Network (TCCON) is a network of ground-based Fourier transfer spectrometers (FTS). An automated solar observatory measures high quality incoming solar absorption spectra in the near-infrared region ($4000 - 9000 \text{ cm}^{-1}$) (www.tcon.caltech.edu, Wunch et al. 2011, 2010). There are 16 sites located worldwide, including both operational and future sites. Although unevenly distributed over the world, the ensemble retrieves the long-term column-averaged abundance of greenhouse gases, such as carbon dioxide (CO_2), methane (CH_4), and other trace gases (e.g. CO , N_2O) with high accuracy and high precision (Washenfelder et al. 2006; Wunch et al. 2010, 2011; Yang et al. 2002).

The difference between column-averaged CO_2 (X_{CO_2}) and surface CO_2 can vary from 2 to 10 ppmv depending on the location and the time of the year (Olsen and Randerson 2004). Compared to surface values, the seasonal variation of X_{CO_2} generally has a time lag in phase with less variability due to the time delay caused by the vertical mixing. The advantage of the column measurements is that they are less affected by the variability due to the vertical transport, but they are also less sensitive to surface sources and sinks. Higher surface concentrations usually occur at nighttime or in winter due to CO_2 buildup in a shallow planetary boundary layer (PBL), while surface uptake due to plant growth occurs during the daytime or in summer. Therefore, the vertical profile information of

atmospheric CO₂ is required for estimating the regional source and sink, understanding the vertical transport, and determining the exchange between the surface and atmosphere.

In this chapter, we show that the vertically constrained CO₂ abundance can be retrieved from TCCON high-quality measurements. A major improvement to the column retrieval is that three scaling factors along each profile are retrieved to obtain the vertical distribution information. In addition to the accurately retrieved total column abundance, the vertical variation is given by the partial column averaged CO₂ in different parts of the atmosphere.

The major uncertainty sources in the TCCON retrievals are spectroscopy, measurement noise, instrument line shape function (ILS), temperature, surface pressure, zero line offset and airmass. A lot of efforts have been undertaken to reduce the instrumental uncertainties of a TCCON experiment (Abrams et al. 1994; Gisi et al. 2011; Hase et al. 1999; Keppel-Aleks et al. 2007; Messerschmidt et al. 2010). The overview of the uncertainty study for the TCCON measurement is discussed in Wunch et al., (2010, 2011). Calibration and quantification of the precision and accuracy of the column measurements have been done against the *in situ* aircraft profiles. In this study, we also use one of these aircraft profiles, measured at Park Falls (Washenfelder et al. 2006) on July 12, 2004, as a validation source for the retrievals from coincident spectra.

There has been a lot of previous work devoted to the microwindow retrievals and channel selections. In general, the sources of retrieval errors include the random errors of the

measurement, and the systematic errors of the forward model and its input parameters. One goal of channel selection is to make an optimum trade-off between random measurement errors and systematic errors (Clarmann et al. 2001). Adding more channels usually decreases random measurement errors but increases the systematic errors.

Some work on the optimization of retrievals from high spectral resolution measurements are based on information content (IC) analysis. Most of the earlier work has focused on choosing microwindows for retrieving temperature, humidity and other geophysical parameters. For example, Clarmann et al. (2001) and Dudhia et al. (2002) developed the microwindow selection method for the Michelson Interferometer Passive Atmospheric Sounding (MIPAS) measurement; Chédin et al., (2003) and Crevoisier et al. (2003) used channel selection for CO₂ retrieval from AIRS spectra; Sofieva and Kyrölä (2003) described channel selection for GOMOS measurements, Worden et al. (2004) for TES, Saitoh et al. (2009) for GOSAT, and Kuai et al. (2010) for OCO-2.

The selection of optimized microwindows by Clarmann et al. (2001) was applied to N₂O microwindows for measurements made by a Fourier transform spectrometer. Another practical application of the microwindow selection that maximizes IC was demonstrated for the retrieval of methane profiles from MIPAS measurements by Dudhia et al. (2002). Crevoisier et al. (2003) extended the methods to reduce the number of channels for the retrieval of CO₂ and other trace gases from AIRS. They compared a new method, the Optimal Sensitivity Profile (OSP) method, with other methods based on IC and degrees of freedom (DOF) analysis and concluded that using the OSP method optimized the

choice of channels for AIRS retrievals of CO₂ and other trace gases. The methods for the selection of measurement subsets using information theory were also examined by Sofieva and Kyrölä (2003). They developed a sequential deselecting procedure and proposed a fast algorithm for channel selection. These methods were applied to the selection of the most informative spectral channels for GOMOS measurements. GOMOS is a stellar occultation instrument for UV-visible spectra. Saitoh et al. (2009) developed an algorithm to retrieve CO₂ vertical profiles from the 15 μm band (700 – 800 cm⁻¹) for GOSAT. They showed that separately selecting a subset of channels based on CO₂ IC for three vertical regions provided retrieval results equivalent to those using all channels in the 15 μm band. A case study of the channel selection based on information analysis for CO₂ retrievals using OCO-like measurements are discussed by Kuai et al. (2010).

We use the microwindow synthetic measurements for both scaling retrieval and profile retrieval. The microwindow scaling retrievals from real TCCON measured spectra are also tested.

This chapter is organized as follows. TCCON and aircraft data, information analysis, and the setup of the vertically constrained retrieval are described in section 2. The study of the profile retrievals including both synthetic and realistic tests is discussed in section 3. The realistic retrievals are calibrated against an aircraft CO₂ profile. In section 4 we show the studies of the microwindow retrievals. The conclusions and more discussions follow in section 5.

2.2 Data and Methodology

2.2.1 TCCON Data

The precision in CO₂ total column measurements from TCCON is achieved to better than 0.25% (Wunch et al. 2010, 2011). With this precision, the monthly averaged column-integrated data are sufficient to reduce the uncertainties in the global surface carbon sources and sinks (Rayner and O'Brien 2001). The absolute accuracy of the CO₂ column measurements from TCCON is ~1% (Wunch et al. 2010).

These measurements have been calibrated using aircraft profile data in World Metrological Organization (WMO)-scale over five TCCON sites (Park Falls, Lamont, Darwin, Lauder and Tsukuba) (Wunch et al. 2010) so that they can be used in combination with *in situ* measurements for carbon cycle science.

The estimation of X_{CO_2} from TCCON data is also a primary validation source for the satellite observations from the Atmospheric Infrared Sounder (AIRS) (Chahine et al. 2005, 2008), the Tropospheric Emission Spectrometer (TES) (Kulawik et al. 2010), the Infrared Atmospheric Sounding Interferometer (IASI) (Crevoister et al. 2009), Orbiting Carbon Observatory (OCO-2) (Crisp et al. 2004), SCanning Imaging Absorption SpectroMeter for Atmospheric CartographY (Sciamachy) (Bosch et al. 2006), and Greenhouse Gases Observing Satellite (GOSAT) (Sato et al. 2009; Yokomizo 2008; Yokota et al. 2009). In contrast to the space-based instruments such as SCIAMACHY and GOSAT, which look down from the sky to record the reflected sunlight, the retrievals

from the TCCON spectra have minimal influences from aerosol, uncertainty in airmass, or variation in land surface properties (Wunch et al. 2011). TCCON data serve as a transfer standard between satellite observations and *in situ* networks (Reuter et al. 2011; Wunch et al. 2009, 2010, 2011; Yang et al. 2002).

2.2.2 Aircraft In Situ Profiles

The aircraft *in situ* measurements of CO₂ profiles have higher precision (~0.2 ppmv) and higher accuracy (~0.2 ppmv) (Wunch et al. 2010). We can consider these measurements to be the best observations of the true state of the atmosphere. In this study, the remote sensing measurements of CO₂ over Park Falls, Wisconsin site on July 12, 2004 (Washenfelder et al. 2006) are compared with the coincident *in situ* measurements during the Intercontinental Chemical Transport Experiment—North America campaign (INTEX—NA, Singh et al. 2006). The detection limit per response for CO₂ from NASA's DC-8 is 0.1 ppmv/1 s (Singh et al., 2006). Highly precise (± 0.25 ppmv) CO₂ profiles were obtained from 0.2 to 11.5 km in about 20 km radius. Due to the limitation of the aircraft measurements for altitude floor and ceiling, additional information for the surface and the stratosphere are required. The lowest measured value was assumed to be the surface value, and the profile above the aircraft ceiling was empirically derived from *in situ* measurements on high-altitude balloons (Wunch et al. 2010). An excellent correlation has been found by the comparison of the integrated aircraft profiles and the FTS retrieved X_{CO₂} (Singh et al. 2006; Washenfelder et al. 2006; Wunch et al. 2010). The calibration using aircraft data reduced the uncertainty in the retrieved X_{CO₂} by

TCCON to 0.25% (Singh et al. 2006; Washenfelder et al. 2006; Wunch et al. 2010, 2011).

In this work, we also use aircraft measured CO₂ profile as our standard. In addition to the comparison of total X_{CO₂}, we look at the difference in the partial X_{CO₂} in each scaling layer. The knowledge of the partial X_{CO₂} can improve our understanding of the vertical variation in the atmospheric CO₂.

2.2.3 Information Analysis

Recording the direct solar spectra, the TCCON FTS measurements have higher signal-to-noise ratio (SNR), about 885 for the InGaAs detector and 500 for the Si diode detector (Washenfelder et al. 2006), than the measurements of the same spectral region but in the reflected sunlight from GOSAT and OCO-2 instruments (~300). The CO₂ 1.6 μm band is measured using an InGaAs detector. The FTS measures absorption spectra with the high resolution of 0.02 cm⁻¹, and the fitted spectra are resolved to an even higher resolution of 0.0075 cm⁻¹. These measured spectra are about ten times finer resolution than those from spacecraft instruments.

The information theory analysis shows that, assuming SNR to be 885 for TCCON measurements and the diagonal value of a priori covariance matrix to be the square of 3% for CO₂ variations, the degrees of freedom for signal of the CO₂ from TCCON retrieval is 3.6, 3.8 and 4.3 for solar zenith angle (SZA) 22.5°, 58° and 80° respectively (table 2.1). The instrument noise level is a key parameter in most retrievals (O'Dell et al. 2010). Even

assuming SNR to be 300, there are still as many as 2.7 and 2.8 degrees of freedom from TCCON spectra with SZA 22.5° and 58° . A similar calculation for OCO-2 only gives 1.5 degrees of freedom because this measurement has lower resolution and lower SNR. The information theory analysis suggests that the CO₂ retrieval from TCCON measurements has at least three pieces of independent information. Its high spectral resolution and high SNR are sufficient to yield three pieces of vertical information.

The profile information is contained in the absorption line shape due to the pressure broadening. The CO₂ Jacobian profiles describe the sensitivity at the particular frequency to the CO₂ changes in different levels of the atmosphere. The Jacobian profiles for TCCON channels have peaks located at different levels resulting from the high spectra resolution (figure 2.1 d). Those channels that are closer to the line center (blue) have broader peaks, and have sensitivity to the CO₂ in middle and upper troposphere. The intermediate absorption channels (green) have larger peak values than both weak absorption and strong absorption channels. In contrast, the Jacobians from the channels measured by OCO-2 all maximize near the surface because its spectral resolution is not sufficient to capture the channels close enough to the line center that could provide complementary information higher up (figure 2.1 a and c).

2.2.4 Retrieval Setting

The TCCON instrument has a precise solar tracking system that records the direct sunlight. The high-quality spectra are measured under clear sky and can be corrected by the recorded DC-signal for partial cloudy sky condition (Keppel-Aleks et al. 2007). The

slant column of each absorber is obtained by a nonlinear least-square spectral fitting using a line-by-line spectral fitting algorithm (GFIT) developed at JPL. The radiative transfer model in GFIT computes simulated spectra using 71 vertical levels with 1 km intervals for the input atmospheric state. The details about the TCCON instrument setup and GFIT code are also described in Deutscher et al., 2010; Geibel et al., 2010; Washenfelder et al., 2006; Wunch et al., 2010, 2011; Yang et al., 2002.

The retrievals use one of TCCON-measured CO₂ absorption bands centered at 6220.00 cm⁻¹ with window width of 80.00 cm⁻¹ (figure 2.2) to compute the total column abundance. A study of the temperature sensitivity of the CO₂ retrieval suggests that a systematic error of 5 K in temperature profile would cause 0.35% or about 1 ppmv error in CO₂ (Yang et al. 2002). This is because the near infrared (NIR) CO₂ absorption band is much less sensitive to temperature than the thermal IR band (i.e., 15 μm), which has a 30 ppmv error in retrieved CO₂ for 1 K uncertainties in temperature (Kulawik et al. 2010).

In the scaling retrieval, assuming we have a good knowledge of the true atmospheric state with minimized spectroscopic errors, instrument line shape functions, etc., a scaling factor (γ) of the a priori profile (x_a) is retrieved. The estimated state vector can be calculated as

$$\hat{x} = \gamma \cdot x_a.$$

The improvement based on the scaling retrieval in this work is that instead of retrieving one scaling factor for the whole atmospheric CO₂, we retrieve three scaling factors. By scaling the three parts of the a priori profile, we can determine how the total column averaged CO₂ is vertically distributed in the atmosphere. To distinguish this from the scaling retrieval, we call it the profile retrieval in this chapter.

2.3 Profile Retrievals

2.3.1 Synthetic Retrievals

The retrieval simulations using the synthetic data would enable us to test the retrieval algorithm. The advantage of the synthetic study is that with the knowledge of the right answer, it can help us to evaluate the precision of the retrievals with different SNR and estimate the errors induced by the uncertainties of the atmosphere. It assumes the forward model is perfect. Thus, no errors arise from the spectroscopy and instrument line shape.

A reference transmission spectrum at 6180 – 6260 cm⁻¹ is simulated using GFIT. Atmospheric profiles including pressure, temperature and humidity are based on NCEP/NCAR reanalysis at Park Falls on July 12, 2004. One hundred synthetic observational spectra are generated by adding to the reference spectrum some noise of amplitude ε/SNR , where ε is a pseudorandom number uniformly distributed between 0 and 1.

Assuming there are no uncertainties in the true state of the atmosphere except the target gas to be retrieved, and that the forward model is perfect, the mean errors (the difference between the retrieved value and the true value) in total X_{CO_2} vary from 0.06 to 0.08 ppmv, depending on the selection of the depth of layers and SNR (885 to 300). Figure 2.3 compares the true partial X_{CO_2} (black star) and mean partial X_{CO_2} from 100 retrievals (red dot) for SNR=885. Their differences are not more than 0.5 ppmv. Three error bars for the 100-retrieved partial X_{CO_2} are no more than 0.7 ppmv. More discussions follow in section 4.3.

Two reasonable methods can be used to determine the depth of the three layers, and both work well in the synthetic retrievals. Since the NIR CO_2 absorption band has its maximum sensitivity in the lower troposphere, most of the information must come from this part of atmosphere, and so we can retrieve two layers below 5 km. We choose to retrieve one layer below 2 km and one layer from 3 to 5 km. The third layer is above 6 km.

The other method is to use the cumulative degrees of freedom as a function of altitude to quantitatively determine the depth of each layer (Natraj et al. 2011). In this way, the top of the bottom layer is determined at 3 km where the cumulative degrees of freedom are about 1. The second layer is from 4 up to 10 km for another one degree of freedom and rest of the atmosphere is the third layer.

The following studies use the first method to divide the layers because we are more interested in the CO₂ vertical distributions in the troposphere.

2.3.2 Realistic Retrievals

For comparison with the aircraft profile on July 12, 2004, the contemporaneous TCCON measured spectra were selected within a 2-hour window centered on the time when the aircraft measurements were taken. The averages of retrievals from these spectra are used, with error bars equal to one standard deviation (std).

Three tests of the profile retrievals started from different *a priori* profiles have been studied. The first test is to use the *a priori* profile that is shifted by 1% from the aircraft profile. Since aircraft data have temporal and spatial limitations, aircraft *a priori* profiles will not be available at all TCCON sites and in all seasons. It is of interest to compare the retrieval results using the GFIT *a priori* and aircraft profile *a priori*. Therefore, the second test is to use the GFIT *a priori* (Toon 1991; Wunch et al. 2011). The CO₂ *a priori* profile is derived by an empirical model based on fits to GLOBALVIEW data (GLOBALVIEW-CO₂: 2008) and changes based on the time of the year and the latitude of the site, for altitudes up to 10 km. In the stratosphere an age-dependent CO₂ profile is assumed (Andrews et al. 2001). This is done to obtain the best possible *a priori* profile for CO₂ at all TCCON sites in all seasons. The third test is to assume that, within each layer, CO₂ is well mixed with a constant mixing ratio. The *a priori* profile in this test is a constant CO₂ of 375 ppmv.

In all three tests, the retrieved CO₂ profiles converged to the aircraft profile (figure 2.4). Compared with the aircraft measurements, the mean biases in total X_{CO₂} for three tests are listed along with their uncertainties in table 2.2. In both profile retrievals and scaling retrievals, the three tests underestimate the total X_{CO₂} from 0.67 to 1.64 ppmv, but the profile retrievals always have less bias (<1ppmv) than the scaling retrievals (>1ppmv) for all three tests. In profile retrievals, there is a slightly smaller bias in the first test (0.67 ppmv) than the other two cases (~0.8 ppmv) because it has the same shape of the *a priori* profile as that measured by the aircraft. However, this advantage does not lead to a critical improvement over the retrievals using different *a priori*. This agrees with what was found by Wunch et al. (2010). In their scaling retrievals for column CO₂, the GFIT *a priori* profiles do not introduce additional bias, compared with the results by replacing the aircraft profiles along with the best estimate of the stratospheric profiles as *a priori* profiles.

The vertical resolution in the GFIT model is 1 km uniformly from the surface to 70 km with 71 grid points in total. We divided them into three scaling layers (0–2 km, 3–5 km and 6 km-top). This allowed us to keep the shape of *a priori* profile within the scaling layers. In the first test, because the shape of the *a priori* profile agrees perfectly with the aircraft profile (figure 2.4 a), the difference between the retrieved profile and aircraft profile within the same scaling layer do not vary much with altitude (figure 2.4 d). This is not true in the other two tests where the *a priori* profiles have different shapes from the true profiles (figure 2.4 b and c). Although relative larger difference can occur where the shape between the two profiles differ a lot in the last two tests (figure 2.4 e and f), the

biases in their partial column averaged CO₂ (diamond in figure 2.4 (d), (e) and (f)) are much reduced due to the compensation between the sublayers. The biases and their error bars for the total X_{CO₂} and partial X_{CO₂} are listed in table 2.3. The error bars in each partial X_{CO₂} are no more than 1 ppmv. Since the first two layers close to the surface are thinner and therefore are less weighted than the third layer, their errors to the partial X_{CO₂} contribute about 25% each in total X_{CO₂} error. The third layer will account for the retaining 50% in total X_{CO₂} error. Large uncertainties in the upper atmosphere result from the lack of information in the stratosphere. Wunch et al. (2011) mentioned that the stratospheric uncertainty is a significant component of the total error.

The profile retrievals using the GFIT a priori profile on the other two dates than July 12 in 2004 at Park Falls are compared with their aircraft measured data. Table 2.4 lists the bias in total and partial X_{CO₂} with their error bars. It suggests that the total X_{CO₂} error is all less than 1 ppm for the three days comparisons with 0.3-ppm precision. Most of the errors in partial X_{CO₂} are less than 1 ppm and some of them are between 1 and 2 ppm. The precisions are less than 1 ppm.

In the above studies, we show that in addition to the accurate estimation of the total X_{CO₂}, the profile retrievals can also provide vertical information about the CO₂ distribution as partial X_{CO₂}.

2.4 Channel Selections

In addition to the CO₂ absorption lines, the spectral window also contains weak absorption signatures of solar lines or other gases, e.g., H₂O and CH₄ (figure 2.5). The GFIT jointly retrieve all these absorbers. The large residuals between the fitted and measured spectra are coincident with the strong solar absorption lines. Information theory analysis show that by carefully selecting the microwindows that are sensitive to the target gas but less sensitive to other parameters, one can obtain the primary information from the whole-window retrieval (Kuai et al. 2010). A study of the channel selection for the TCCON spectra at 1.6 μm CO₂ band using information analysis is described in table 2.5. The details about the method of choosing good channels are discussed in Kuai et al. (2010). By combining the channels with most information about CO₂ profiles, the total degrees of freedom are still more than 3.0, for example, while reducing the number of channels from 10620 to 488. This suggests that the retrievals using the selected channels can provide almost as much information as the whole-window retrievals.

Two microwindows retrievals are compared with the whole-window retrieval. Microwindow I is centered at 6243.985 cm⁻¹ with the width of 3 cm⁻¹, including three absorption lines (figure 2.6 (e)). Microwindow II is also centered at 6243.985 cm⁻¹ but with the width of 1 cm⁻¹, which including 1 absorption line (figure 2.6 (h)). The first comparisons between the two microwindow retrievals and whole-window retrieval were performed in the synthetic scaling retrievals. Then the same steps would be applied to the realistic scaling retrievals from the aforementioned thirty-two simultaneous TCCON and

aircraft measurements on July 12, 2004 at Park Falls. The results on profile retrieval using microwindows will be presented after the scaling retrievals.

2.4.1 Synthetic Scaling Retrievals

Table 2.6 depicts the test of the microwindow scaling retrievals and their comparison with the whole-window retrievals in a synthetic study. With different SNR, the X_{CO_2} is accurately retrieved with error about 0.01%. However, the standard deviation of one hundred retrievals will increase from wider windows to narrower windows.

The error can be reduced from 0.2 ppmv to 0.07 ppmv from low SNR (=300) to high SNR (=885) for the retrievals with microwindow I. The benefit of using fewer channels in the retrieval is to reduce the systematic errors caused by the uncertainties in atmospheric parameters. However the advantage of using more channels in the retrieval is to reduce the error due to the random noise. Therefore, the rule to determine the total number of the channels is to minimize system biases and random errors.

2.4.2 Realistic Scaling Retrievals

After the simulated retrievals show that the retrievals with microwindows can perform as well as the whole-window retrievals, the same comparison is carried out between the retrievals from TCCON spectra and the aircraft CO_2 . Figure 2.6 shows the results of retrievals from the same measured spectrum but different windows. A large residual was found near 6244.41 cm^{-1} in figure 2.6 (f) due to the solar absorption line. Other large residuals are close to the line centers (figure 2.6 (f) and (i)). Table 2.7 documents the

mean bias of the thirty-two retrieved total X_{CO_2} relative to the aircraft X_{CO_2} . When the outliers are removed, the negative biases do not change significantly, but the precision of the retrievals is greatly reduced, especially for microwindow II with a narrower window. Both the synthetic and realistic retrievals suggest that the accuracies of the retrievals from different windows are almost the same but the uncertainties increase for narrower window.

2.4.3 Synthetic Profile Retrievals

Similar microwindow retrievals are also applied to the profile retrievals. Table 2.8 depicts the mean difference between the 100 retrievals and the truth. In addition to the bias in total X_{CO_2} , the biases in three partial X_{CO_2} are also included. The mean deviations from the true total X_{CO_2} are quite small (<0.3 ppmv) for the retrievals from different windows and different SNR. The wider window to be fitted or the larger SNR results in a smaller bias, but their influences are not significant. However, their effects on standard deviations are more pronounced. The negative biases in total X_{CO_2} are always found in the tests because the *a priori* CO_2 profiles are set to be 0.99 times the true profile. The partial column bias can be either positive or negative. However, they will be canceled in the calculation for the total column. In the scaling retrieval, microwindow II including 1 absorption line works well or can be even better, as shown in section 5.1 and 5.2. However, when additional vertical information needs to be retrieved, it has relatively larger biases and error bars in partial X_{CO_2} . A wider window is required for high precision. Thus, microwindow II is preferred in profile retrievals.

The retrievals listed in Table 2.8 all use 3% as the variations in CO₂ and diagonal matrix for covariance matrix. We also find that increasing the constraint in the stratosphere will improve the results. This is because there is little information in the stratosphere, and it relies more on the a priori. Further study of the microwindow for the realistic retrievals will be done in future.

2.5 Conclusions

TCCON provides long-term observations for the understanding of the CO₂ variations in different timescales and at different latitudes. In addition to the column retrievals of the CO₂, the complementing information on the vertical distribution of CO₂ can be obtained from those observations with high spectral resolution and high SNR. Our calculations have confirmed their potential for retrieving the CO₂ profile. The realistic profile retrievals from TCCON spectra are compared to CO₂ profiles measured *in situ* by aircraft. The comparison between the retrieved X_{CO_2} and the integration of the aircraft CO₂ profiles show an underestimation from both scaling and profile retrievals. This agrees with the conclusion from the previous work about the calibration of TCCON data against the aircraft measurements. The ratio of the X_{CO_2} determined from FTS scaling retrievals to that from integrated aircraft measured profile gives a correction factor of 0.991 ± 0.002 (mean \pm standard deviation of the ratios of FTS to aircraft X_{CO_2}) at Park Falls (Washenfelder et al. 2006; Wunch et al. 2010). However, Wunch et al. also retrieved CO₂ from the another band at 6339 cm^{-1} , and computed the average of two retrievals before they are scaled by the retrieved O₂ to a mean value of 0.2095 in order to

get the dry air column-averaged mole fractions (Deutscher et al. 2010; Geibel et al. 2010; Washenfelder et al. 2006; Wunch et al. 2010). Here we retrieved only from the window at 6220 cm^{-1} and did not scale by O_2 at this stage. The correction using scaling by retrieved O_2 help only to reduce the scattering of the retrieved data by reducing systematic errors that appears simultaneously in both CO_2 and O_2 but not to reduce the bias.

In this chapter, we place emphasis on expanding the scaling retrieval of total column integrated CO_2 to three partial columns. With this study, we demonstrate that the profile retrieval works as well as scaling retrieval and it provides the vertical information in three partial X_{CO_2} , in addition to the accurate retrieval of total X_{CO_2} . The microwindow retrievals that are more sensitive to CO_2 but have weaker signatures by other absorbing gases or solar lines can help to reduce the systematic error from their uncertainties but may be more influenced by random noise. The retrievals using smaller number of channels can perform as well as that fitting the whole absorption band. The test cases of microwindow retrievals demonstrate the potential of using selected channels for CO_2 retrievals with vertical constraints. The additional knowledge of the vertical distribution of the CO_2 will be useful for the quantification of the CO_2 sources and sinks.

2.6 Acknowledgements

This research is supported in part by the Orbiting Carbon Observatory 2 (OCO-2) project, a NASA Earth System Science Pathfinder (ESSP) mission and Project JPL.1382974 to the California Institute of Technology. We would like to thank Mimi Gerstell, Vijay

Natraj, Sally Newman, Jack Margolis, Xi Zhang, King-Fai Li, and Michael Line for useful discussions and comments on the paper. A special acknowledge should be given to Professor Yuk Yung for his efforts in editing this paper.

2.7 References

- Abrams, M. C., et al., 1994: Practical example of the correction of Fourier-transform spectra for detector nonlinearity. *Appl. Opt.*, **33**, 6307–6314.
- Andrews, A. E., et al., 2001: Mean ages of stratospheric air derived from in situ observations of CO₂, CH₄, and N₂O. *J. Geophys. Res. — Atmos.*, **106**, 32295–32314.
- Bosch, H., et al., 2006: Space-based near-infrared CO₂ measurements: Testing the Orbiting Carbon Observatory retrieval algorithm and validation concept using SCIAMACHY observations over Park Falls, Wisconsin. *J. of Geophys. Res. — Atmos.*, **111**, D23302, doi:23310.21029/22006jd007080.
- Chahine, M. T., et al., 2005: On the determination of atmospheric minor gases by the method of vanishing partial derivatives with application to CO₂. *Geophys. Res. Lett.*, **32**, L22803, doi:10.1029/2005gl024165.
- , 2008: Satellite remote sounding of mid-tropospheric CO₂. *Geophys. Res. Lett.*, **35**, L17807, doi:10.1029/2008gl035022.
- Chédin, A., et al., 2003: The feasibility of monitoring CO₂ from high-resolution infrared sounders. *J. Geophys. Res.—Atmos.*, **108**, art. no.—4064.
- Clarmann, T. V., et al., 2001: Optimized microwindows in atmospheric spectroscopy. *Hyperspectral Remote Sensing of the Land and Atmosphere*, W. L. Smith, and Y. Yasuoka, editors, 135–142.
- Crevoisier, C., et al., 2003: AIRS channel selection for CO₂ and other trace-gas retrievals. *Q. J. R. Meteorol. Soc.*, **129**, 2719–2740.

- , 2009: First year of upper tropospheric integrated content of CO₂ from IASI hyperspectral infrared observations. *Atmos. Chem. Phys.*, **9**, 4797–4810.
- Crisp, D., et al., 2004: The orbiting carbon observatory (OCO) mission. *Trace Constituents in the Troposphere and Lower Stratosphere*, J. P. Burrows, and A. M. Thompson, editors., 700–709.
- Deutscher, N. M., et al., 2010: Total column CO₂ measurements at Darwin, Australia site description and calibration against in situ aircraft profiles. *Atmos. Meas. Tech.*, **3**, 947–958.
- Dudhia, A., et al., 2002: Microwindow selection for high-spectral-resolution sounders. *Appl. Opt.*, **41**, 3665–3673.
- Geibel, M. C., et al., 2010: A new fully automated FTIR system for total column measurements of greenhouse gases. *Atmos. Meas. Tech.*, **3**, 1363–1375.
- Gisi, M., et al., 2011: Camtracker: A new camera controlled high precision solar tracker system for FTIR-spectrometers. *Atmos. Meas. Tech.*, **4**, 47–54.
- GLOBALVIEW-CO₂., 2008: Cooperative Atmospheric Data Integration Project — Carbon Dioxide, CD-ROM, NOAA ESRL, Boulder, Colorado, also available on Internet via anonymous FTP to <ftp.cmdl.noaa.gov>, last access: July 2009, Path: [ccg/co2/GLOBALVIEW](ftp://ccg/co2/GLOBALVIEW).
- Hase, F., et al., 1999: Analysis of the instrumental line shape of high-resolution fourier transform IR spectrometers with gas cell measurements and new retrieval software. *Appl. Opt.*, **38**, 3417–3422.
- Keppel-Aleks, G., et al., 2007: Reducing the impact of source brightness fluctuations on spectra obtained by Fourier-transform spectrometry. *Appl. Opt.*, **46**, 4774–4779.

- Kuai, L., et al., 2010: Channel selection using information content analysis: A case study of CO₂ retrieval from near infrared measurements. *J Quant. Spectrosc. Radiat. Transfer.*, **111**, 1296–1304.
- Kulawik, S., et al., 2010: Characterization of Tropospheric Emission Spectrometer (TES) CO₂ for carbon cycle science. *Atmos. Chem. Phys.*, **10**, 5601–5623.
- Messerschmidt, J., et al., 2010: Side by side measurements of CO₂ by ground-based Fourier transform spectrometry (FTS). *Tellus B.*, **62**, 749–758.
- Natraj, V., et al., 2011: Multispectral sensitivity studies for the retrieval of tropospheric and lowermost tropospheric ozone from simulated clear sky GEO-CAPE measurements, **submitted**.
- O'Dell, C., et al., 2011: Preflight Radiometric Calibration of the Orbiting Carbon Observatory (accepted). *Geoscience and Remote Sensing, IEEE Transactions on*.
- Olsen, S. C., and J. T. Randerson, 2004: Differences between surface and column atmospheric CO₂ and implications for carbon cycle research. *J. Geophys. Res. — Atmos.*, **109**, art. no.-D02301.
- Rayner, P. J., and D. M. O'Brien, 2001: The utility of remotely sensed CO₂ concentration data in surface source inversions. *Geophys. Res. Lett.*, **28**, 2429–2429.
- Reuter, M., et al., 2011: Retrieval of atmospheric CO₂ with enhanced accuracy and precision from SCIAMACHY: Validation with FTS measurements and comparison with model results. *J. Geophys. Res. — Atmos.*, **116**, D04301, doi:04310.01029/02010JD015047.
- Saitoh, N., et al., 2009: CO₂ retrieval algorithm for the thermal infrared spectra of the Greenhouse Gases Observing Satellite: Potential of retrieving CO₂ vertical profile

- from high-resolution FTS sensor. *J. Geophys. Res. — Atmos.*, **114**, D17305, 16 pp., doi:10.1029/2008JD011500.
- Sato, M., et al., 2009: FIP's environmentally conscious solutions and GOSAT. *Fujitsu. Sci. Tech. J.*, **45**, 134–140.
- Singh, H. B., et al., 2006: Overview of the summer 2004 intercontinental chemical transport experiment — North America (INTEX-A). *J. Geophys. Res. — Atmos.*, **111**, D24s01, doi:10.1029/2006jd007905.
- Sofieva, V. F., and E. Kyrölä, 2003: Information approach to optimal selection of spectral channels. *J. Geophys. Res. — Atmos.*, **108**, 4513, doi:4510.1029/2002jd002980.
- Toon, G. C., 1991: The JPL MkIV interferometer. *Opt. Photonics News*, **2**, 19–21.
- Washenfelder, R. A., et al., 2006: Carbon dioxide column abundances at the Wisconsin Tall Tower site. *J. Geophys. Res. — Atmos.*, **111**, D22305, doi:10.1029/2006jd007154.
- Worden, J., et al., 2004: Predicted errors of tropospheric emission spectrometer nadir retrievals from spectral window selection. *J. Geophys. Res. — Atmos.*, **109**, D09308, doi:09310.01029/02004jd004522.
- Wunch, D., et al., 2009: Emissions of greenhouse gases from a North American megacity. *Geophys. Res. Lett.*, **36**, L15810, doi: 10.1029/2009gl039825
- , 2010: Calibration of the total carbon column observing Network using aircraft profile data. *Atmos. Meas. Tech.*, **3**, 1351–1362.
- , 2011: The total carbon column observing network (TCCON). *Phil. Trans. R. Soc. A*, **in press**.

- Yang, Z. H., et al., 2002: Atmospheric CO₂ retrieved from ground-based near IR solar spectra. *Geophys. Res. Lett.*, **29**, 1339.
- Yokomizo, M., 2008: Greenhouse gases observing satellite (GOSAT) Ground Systems. *Fujitsu. Sci. Tech. J.*, **44**, 410–+.
- Yokota, T., et al., 2009: Global Concentrations of CO₂ and CH₄ Retrieved from GOSAT: First Preliminary Results. *Sola*, **5**, 160–163.

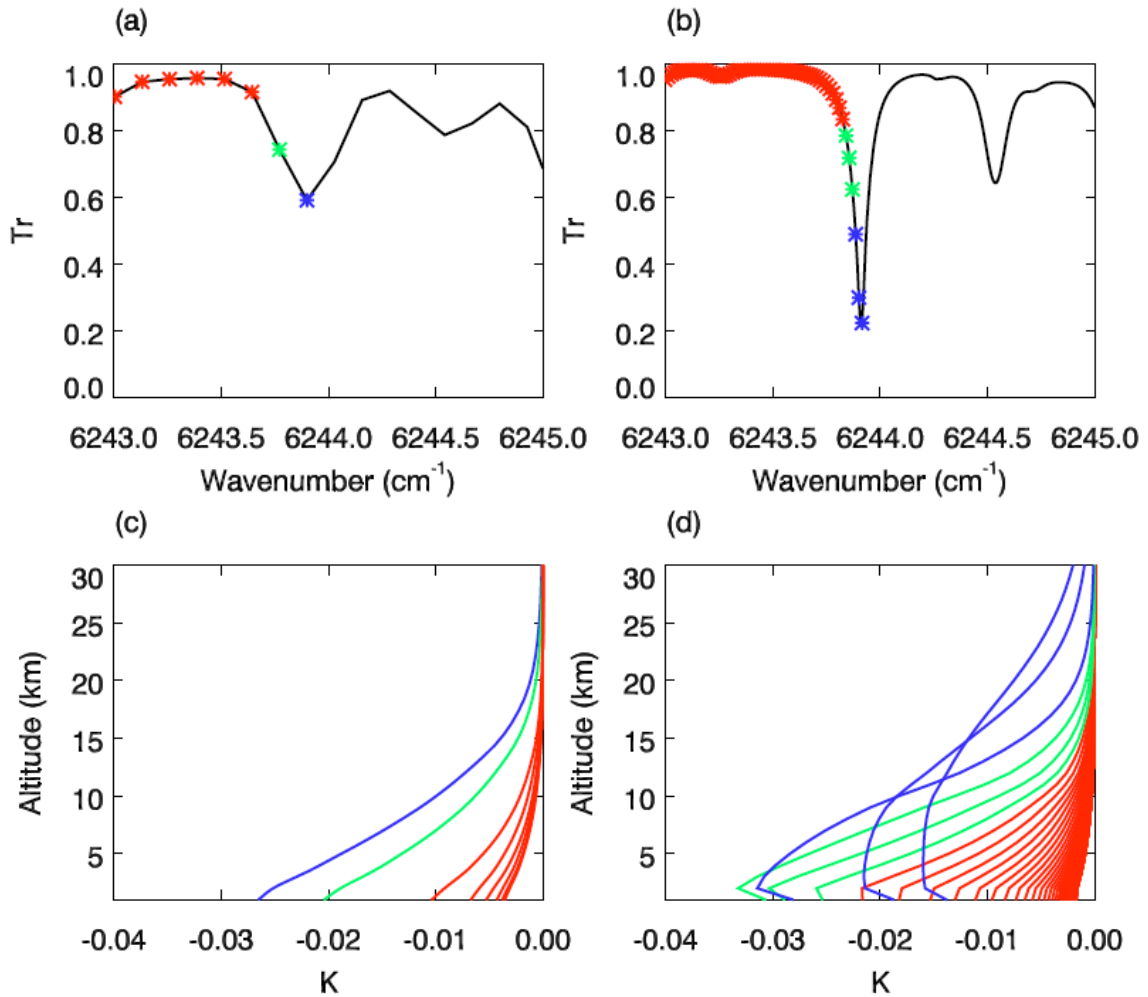


Figure 2.1. The same absorption line centered at 6243.9 cm^{-1} . (a) Measured by OCO-2, $sza=17^\circ$ and (b) by TCCON, $sza=22.5^\circ$. Star indicates the frequency measured. Their corresponding Jacobian ($K=d[Tr]/d[\ln(CO_2)]$) profiles are plotted in the two bottom panels (c) for OCO-2 and (d) for TCCON. The weak absorption channels are in red; intermediate absorption channels are in green; strong absorption channels are in blue.

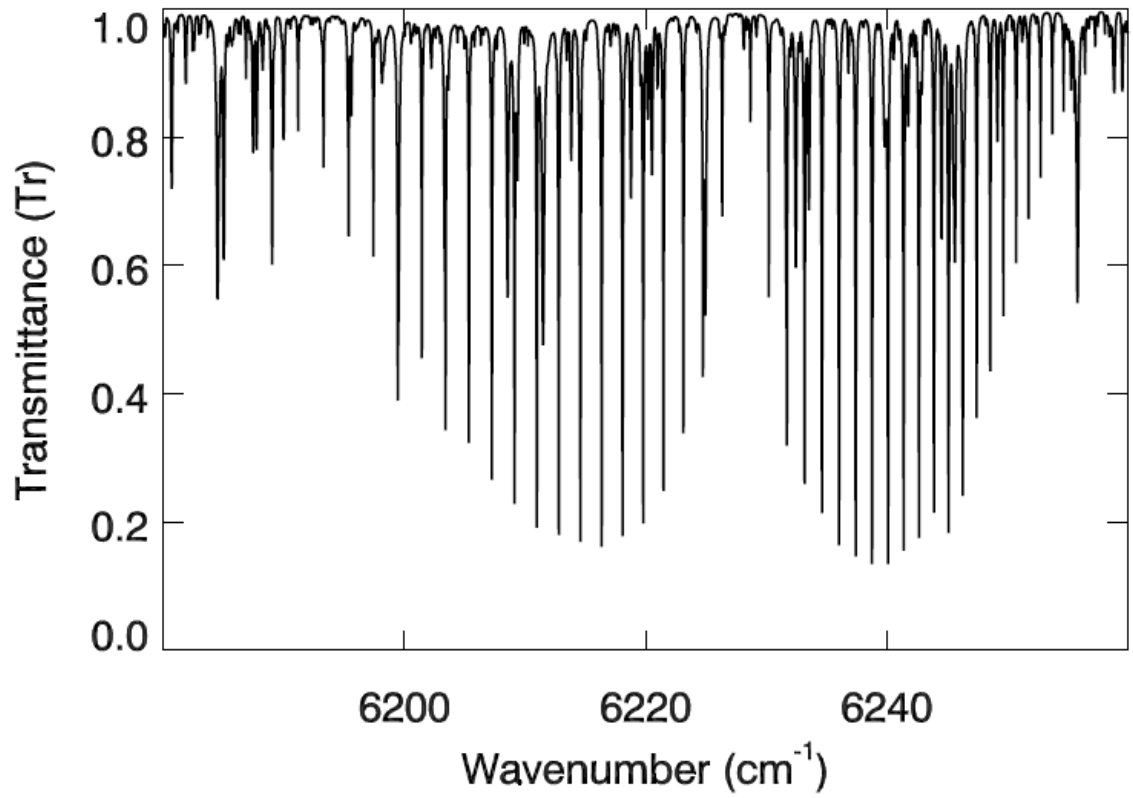


Figure 2.2. CO₂ band at 1.6 μm observed on June 17, 2008 by TCCON at Park Falls (Wisconsin) with solar zenith angle of 22.5°.

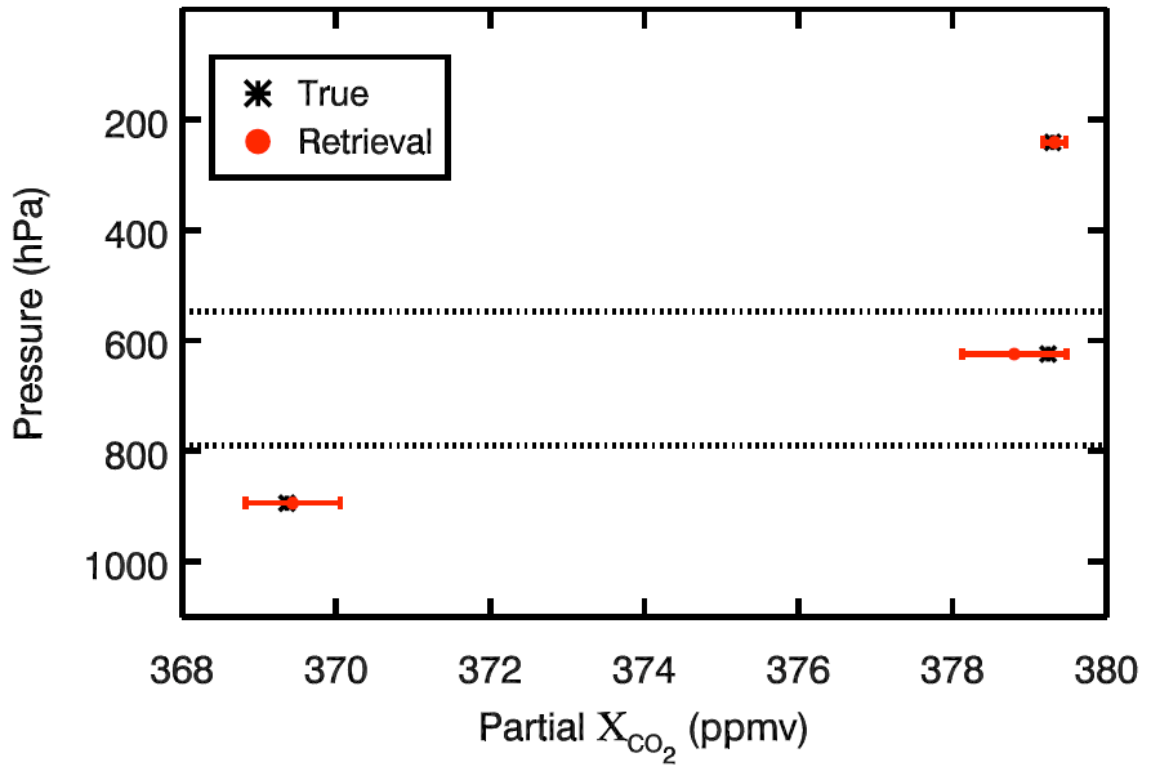


Figure 2.3. Partial X_{CO_2} profile for true (black star) and mean partial X_{CO_2} of 100 retrievals (red dot). SNR = 885. Dot lines indicate the top of each scaling layer. The error bar is one standard deviation of 100-retrieved partial X_{CO_2} .

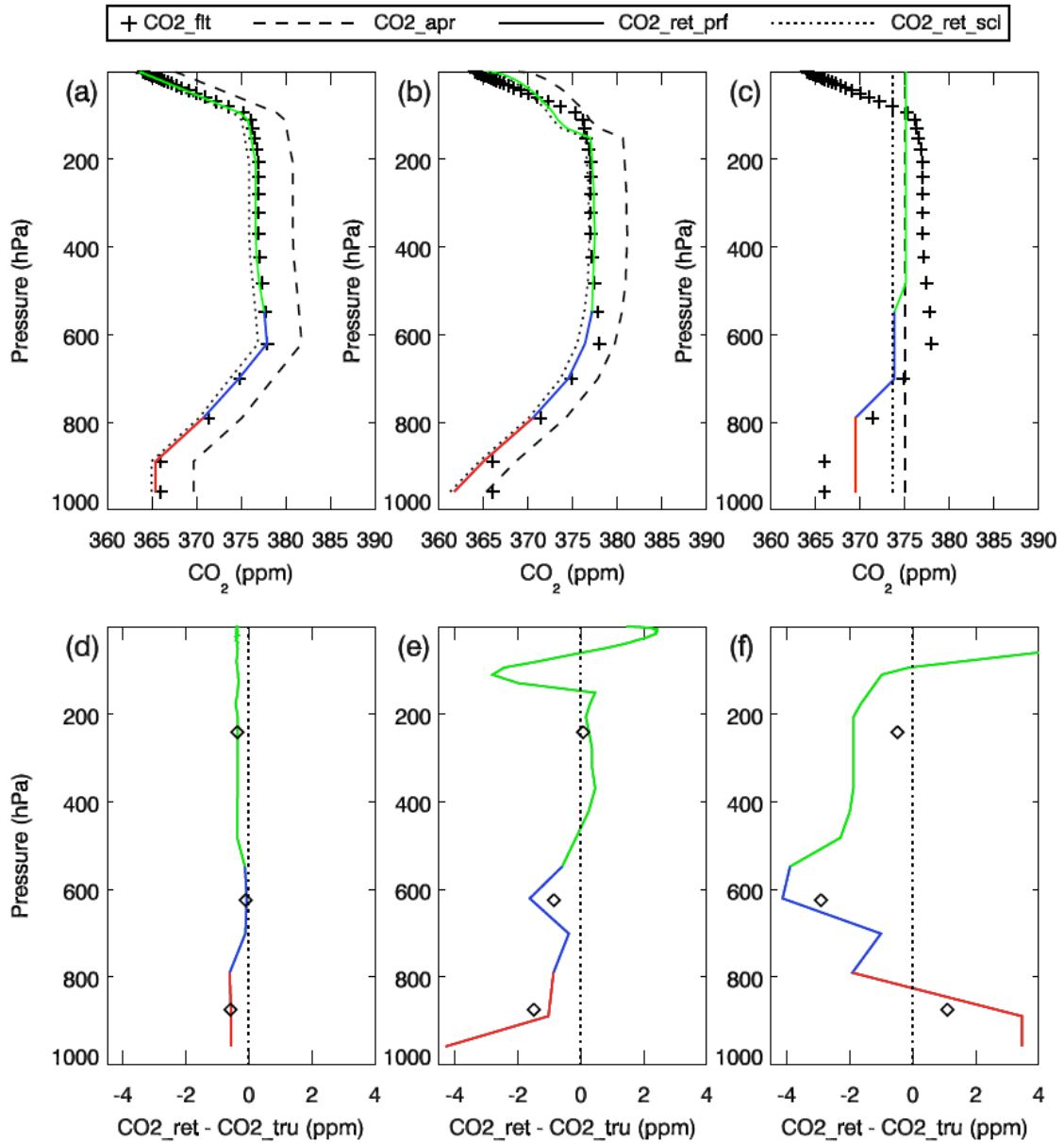


Figure 2.4. Examples of profile retrievals from the same spectrum but with three different a priori profiles. Solid line with three different colors indicate the profile retrieved CO₂. The differences CO₂ between the retrieval profile and aircraft profile are plotted in the bottom panels. The diamonds represent the difference in partial X_{CO₂}. (a) and (d) for test 1; (b) and (e) for test 2; (c) and (f) for test 3.

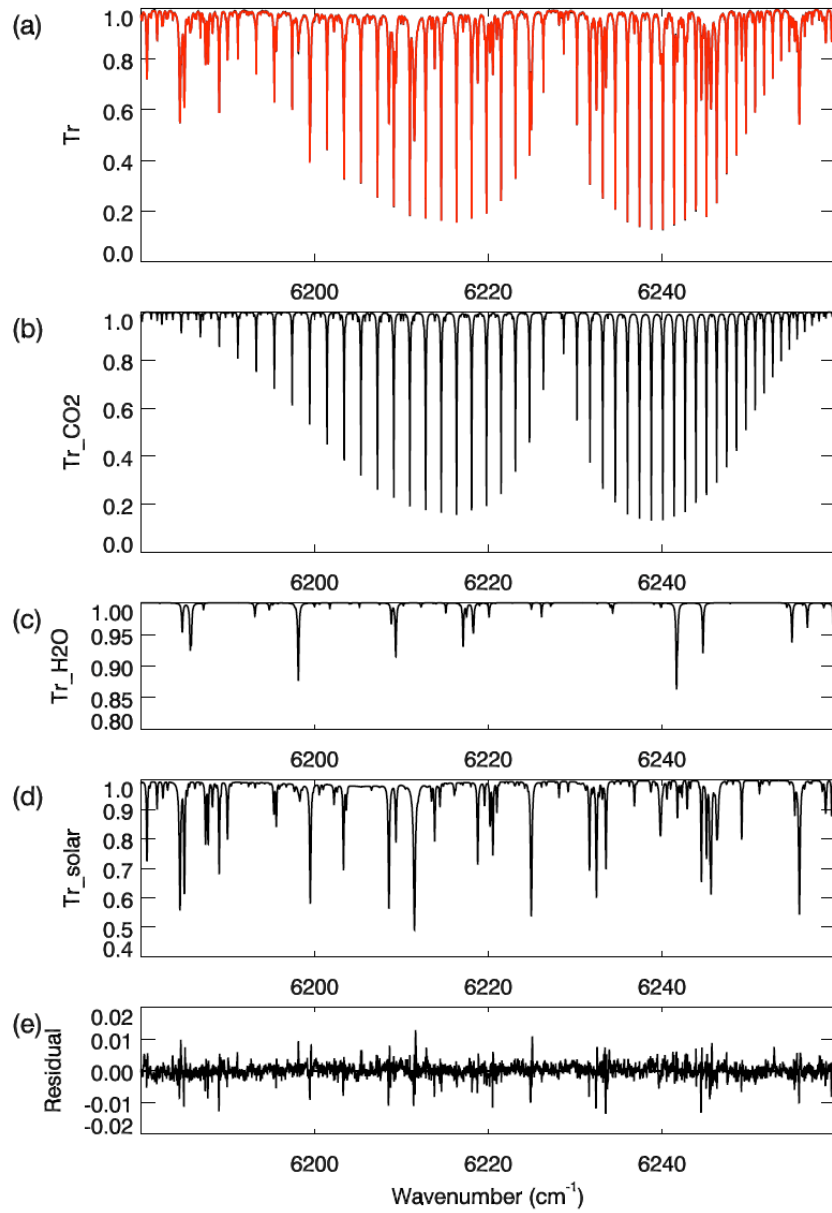


Figure 2.5. (a) Comparison of measured spectrum (black) from TCCON and model spectrum (red line overlapped with black line) by GFIT; (b) CO_2 absorption line; (c) H_2O absorption line; (d) solar absorption line; (e) residuals between the measured spectrum and model spectrum.

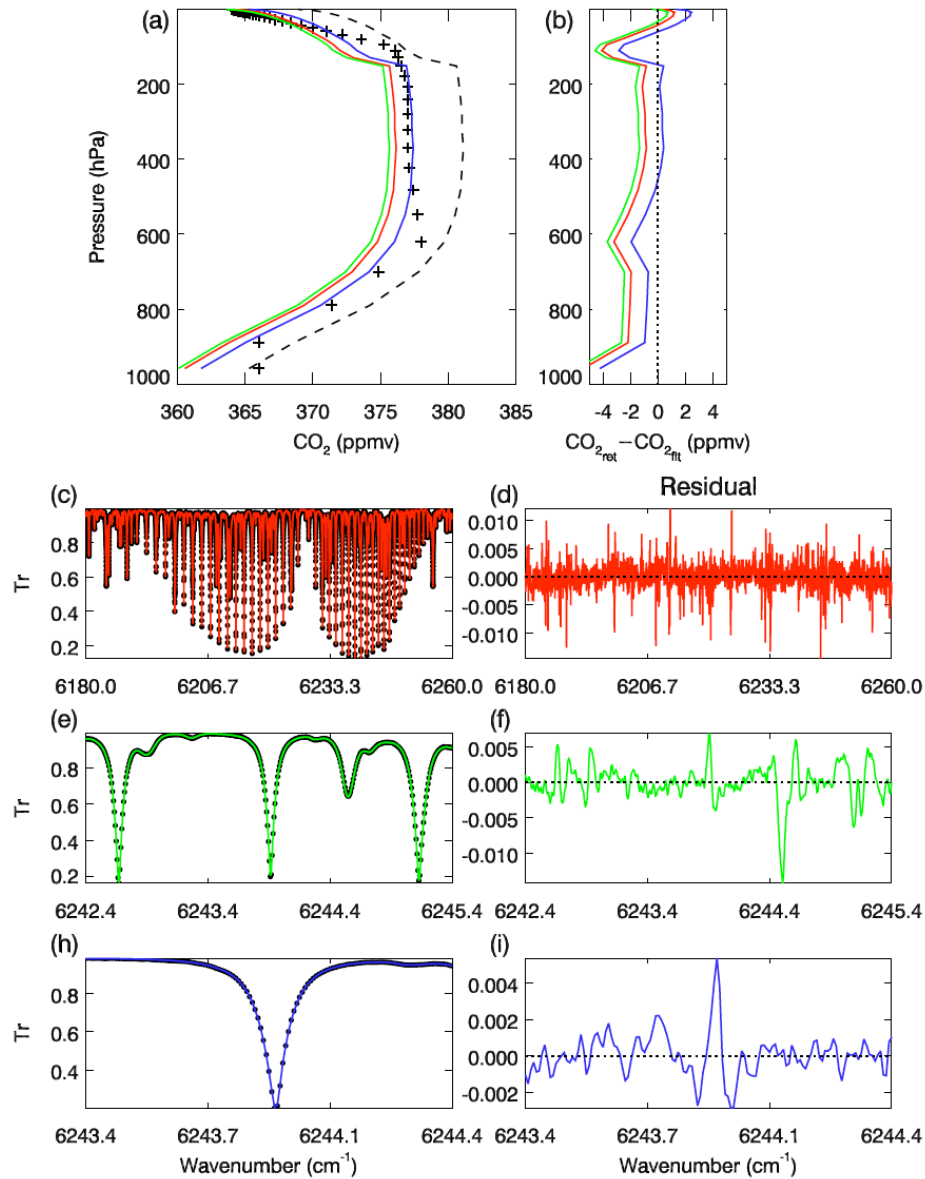


Figure 2.6. Examples of the retrievals from the same spectrum but with three different spectra windows. (a) Comparison of retrieved and aircraft profiles. Dash line for CO₂ *a priori*; (+) for aircraft CO₂ profile; solid line for retrieved CO₂ profile. Red for case full window, green for case microwindow I and blue for case microwindow II. (b) Difference of retrieved profile and aircraft profile. (c), (e) and (f) show the spectrum window for three cases; dot is the measured transmittance and solid line is the calculated transmittance. (d), (f) and (i) demonstrate their residuals

Table 2.1. Information analysis for CO₂ retrievals from TCCON and OCO-2 spectra

	# of channels	SNR	SZA (°)	Information content	Degree of freedom
TCCON	10620	885	80	14.4	4.3
TCCON	10620	885	58	12.5	3.8
TCCON	10620	300	58	7.4	2.8
TCCON	10620	885	22.5	11.6	3.6
TCCON	10620	300	22.5	6.8	2.7
OCO-2	1016	300	17	4.23	1.5

Table 2.2. Bias in total X_{CO_2} from realistic profile retrievals

Type of Retrieval	Bias in total X_{CO_2} (ppmv) (mean \pm std)		
	Test 1	Test 2	Test 3
Profile	-0.67 ± 0.25	-0.85 ± 0.24	-0.80 ± 0.24
Scaling	-1.54 ± 0.29	-1.64 ± 0.35	-1.09 ± 0.29

Table 2.3. Same as table 2.2 but in partial X_{CO_2}

	Bias in total X_{CO_2}	Bias in partial X_{CO_2} (ppmv)		
		Layer 1	Layer 2	Layer 3
Test 1	-0.67 ± 0.25	-0.13 ± 0.76	0.25 ± 0.96	-1.30 ± 0.76
Test 2	-0.85 ± 0.24	-1.07 ± 0.76	0.54 ± 0.96	0.87 ± 0.76
Test 3	-0.80 ± 0.24	4.75 ± 0.76	-3.28 ± 0.96	-1.99 ± 0.78

Table 2.4. Same as table 2.3 but on different dates. The GIT a priori profiles are applied in all the profile retrievals.

Date in 2004	Bias in total	Bias in partial X _{CO₂} (ppmv)		
	X _{CO₂}	Layer 1	Layer 2	Layer 3
07/12	-0.85 ± 0.24	-1.07 ± 0.76	0.54 ± 0.96	0.87 ± 0.76
07/15	-0.44+/-0.19	-1.25+/-0.11	-1.56+/-0.21	0.42+/-0.34
08/14	0.40+/-0.16	-0.82+/-0.34	0.46+/-0.45	1.99+/-0.21

Table 2.5. Information analyses for selected channels

# of channels	Information content	Degree of freedom
10620 (~66 lines)	12.5	3.8
2074 (34 lines)	12	3.6
488 (8 lines)	8.7	3.0
183 (3 lines)	6.7	2.6

Table 2.6. Synthetic scaling retrieval tests for microwindow

Retrievals	SNR	Bias in X_{CO_2} (ppmv)
Whole-window	300	0.03±0.06
Microwindow I	300	0.03±0.20
Microwindow II	300	0.04±0.40
Microwindow I	885	0.02±0.07

Table 2.7. Bias in total X_{CO_2} for realistic scaling retrievals with different spectra windows

	Bias	Bias without outlier
Whole-window	-1.82 ± 0.35	-1.79 ± 0.28
Microwindow I	-1.4 ± 0.61	-1.52 ± 0.48
Microwindow II	-0.48 ± 1.17	-0.30 ± 0.58

Table 2.8. The same as table 2.7 but for the synthetic profile retrievals and also include the biases in partial X_{CO_2}

		Bias in total X_{CO_2}	Bias in partial X_{CO_2} (Mean \pm std) (ppmv)		
	SNR		Layer 1 (0~2 km)	Layer 2 (3~5 km)	Layer 3 (6~70 km)
Whole-window	885	-0.06 \pm 0.05	0.07 \pm 0.62	-0.44 \pm 0.68	0.15 \pm 0.15
Whole-window	300	-0.08 \pm 0.15	-0.17 \pm 1.82	-0.22 \pm 2.01	0.02 \pm 0.48
Microwindow I	885	-0.09 \pm 0.13	-0.13 \pm 0.56	-0.76 \pm 0.45	0.23 \pm 0.45
Microwindow I	300	-0.10 \pm 0.40	-0.26 \pm 1.91	-0.97 \pm 1.23	0.37 \pm 1.51
Microwindow II	885	-0.26 \pm 0.23	-0.56 \pm 0.69	-1.06 \pm 0.43	0.25 \pm 0.56
Microwindow II	300	-0.18 \pm 0.68	-0.75 \pm 2.06	-1.21 \pm 1.29	0.56 \pm 1.82

Part II

Interannual Variability of the Stratospheric

Quasi-Biannual Oscillation

Chapter 3: Nonstationary Synchronization of Equatorial QBO with SAO in Observation and Model

Le Kuai^{1*}, Run-Lie Shia¹, Xun Jiang², Ka-Kit Tung³, Yuk L. Yung¹

1 Division of Geological and Planetary Sciences, California Institute of Technology, Pasadena, CA 91125

2 Department of Earth and Atmospheric Sciences, University of Houston, TX 77204

3 Department of Applied Mathematics, University of Washington, Seattle, WA 98195

Abstract

It has often been suggested that the period of the quasi-biennial oscillation (QBO) has a tendency to synchronize with the semi-Annual oscillation (SAO). Apparently the synchronization is better the higher up the observation extends. Using 45 years of ERA-40 data of the equatorial stratosphere up to the stratopause, we confirm that this synchronization is not just a tendency but a robust phenomenon in the upper stratosphere. A QBO period starts when a westerly SAO (w-SAO) descends from the stratopause to 7 hPa and initiates the westerly phase of the QBO (w-QBO) below. It ends when another w-SAO, a few SAO periods later, descends again to 7 hPa to initiate the next w-QBO. That it is the westerly but not the easterly SAO (e-SAO) that initiates the QBO is also explained by the general easterly bias of the angular momentum in the equatorial stratosphere so that the e-SAO does not create a zero-wind line, unlike the w-SAO. The currently observed average QBO period of 28 months, which is not an integer multiple of SAO periods, is a result of intermittent jumps of the QBO period from 4-SAO periods to 5-SAO periods. The same behavior is also found in a model, the two-and-a-half-dimensional THINAIR model. We find that the nonstationary behavior in both observation and model is not caused by the 11-year solar-cycle forcing, but is instead caused by the incompatibility of the QBO's natural period determined by its wave forcing, and the "quantized" period determined by the SAO. The wave forcing parameter for the QBO period in our current climate probably lies between 4-SAO and 5-SAO periods. If the wave forcing for the QBO is tuned so that its natural period is compatible

with the SAO period above, e.g., at 24 months or 30 months, nonstationary behavior disappears.

3.1 Introduction

The Quasi-Biennial Oscillation (QBO) is an internal oscillation of the equatorial zonal wind in the stratosphere involving wave-mean flow interactions (Holton and Lindzen, 1972; Lindzen and Holton, 1968; Dunkerton, 1997a; Baldwin et al., 2001). There have been numerous observational studies of the QBO in the zonal wind, temperature, and ozone (e.g., Angell and Korshover, 1970; Oltmans and London, 1982; Hasebe, 1983; Zawodny and McCormick, 1991; Randel and Wu, 1996; Pawson and Fiorino, 1998). The equatorial QBO affects the polar stratosphere during winter, with the easterly phase of the QBO creating the condition for a more perturbed and warmer polar vortex (Holton and Tan, 1980, 1982; Baldwin and Dunkerton, 1999, Ruzmaikin et al., 2005). Therefore, the variation of the QBO period has additional significance, especially with respect to the timing of its phase relative to the Northern Hemisphere (NH) winter, a phenomenon called seasonal synchronization (Baldwin et al., 2001).

The mean period of the QBO is around 28 months but is known to have interannual variations of several months about the average. When the QBO was first discovered (Reed et al., 1961; Ebdon and Veryard, 1961), it was found to have a period of 26 months, 13 months each of easterly and westerly phases at 50 hPa. Later it was reported (Tung and Yang, 1994a, b) to have a period of 30 months based on the satellite record of 1979–1992. For the period 1958–2002 spanned by the ERA-40 data (Uppala et al., 2005), the mean QBO period is slightly less than 28 months (see below). It becomes a little longer than 28 months in the longest data record (rocketsonde and rawinsonde) (1953–

2007), which is available from Free University of Berlin (FUB) (Baldwin et al., 2001; Fischer and Tung, 2008). It is interesting to point out that the length of QBO periods is not constant but is quite variable. Individual QBO episodes do not have a mean period of around 28 months with a normal distribution of variability around the mean. For example, the current estimate of 28 months as the mean QBO period is composed of a collection of individual periods of approximately 24 months and 30 months (and an occasional 36 months in the longest records). Thus, the period of a QBO event is a multiple of the 6 month period of the semi-annual oscillation (SAO). Since the SAO is seasonally synchronized, with respect to Northern and Southern Hemisphere winters, the tendency of the QBO to synchronize with the SAO may be an important cause of its seasonal synchronization.

As pointed out by previous authors (Lindzen and Holton, 1968; Gray and Pyle, 1989; Dunkerton and Delisi, 1997b), the SAO's alternating easterly and westerly shear zones near the stratopause level serve to "seed" the QBO below. In particular, the onset of the westerly phase of the QBO (w-QBO) is tied to the downward propagation of the westerly phase of the SAO (w-SAO). A QBO period starts when the zero-wind line associated with the westerly shear zone of the SAO descends into the QBO region below. A QBO period ends when the next such westerly descent occurs after a multiple of SAO periods later and replaces the easterly phase of the QBO (e-QBO) below. In this way the QBO period is "quantized" in units of the SAO period. Lindzen and Holton (1968) found that "the appearance of successive westerly regimes at 30 km tends to be a multiple of 6 months." Since it is thought that there may be other factors that can affect the descent rate

of the QBO from the upper to the lower stratosphere, in the lower stratosphere this property has been regarded more as a “tendency” than a strict synchronization in reality (Dunkerton and Delisi, 1997b).

This chapter is divided into 5 sections. In section 2, we will show that in fact the QBO period is better synchronized with the SAO than previously thought, using the ERA-40 reanalysis data that extends to the stratopause. We will also show that the decadal variation in the QBO period previously reported often takes the form of a discrete jump in integer multiples of SAO period. In section 3, we will use a model to explain why the QBO period variation is nonstationary in our current climate regime. A possible mechanism for QBO-SAO synchronization will be discussed in section 4 and it will be followed by conclusions in section 5.

3.2 QBO-SAO Synchronization: Data Analysis

Figure 3.1 shows the height-time cross section of the equatorial zonal wind in the ERA-40 dataset up to 1 hPa. Baldwin and Gray (2005) compared the ERA-40 reanalysis zonal winds with the tropical rocketsonde and rawinsonde observations, and concluded that the reanalysis provides “a good representation of tropical winds up to 2–3 hPa. The amplitudes of the QBO and the SAO derived from ERA-40 data match the rawinsonde and rocketsonde observations up to 2–3 hPa.” They further suggested “zonal-mean ERA-40 winds could be used, for most purposes, in place of rawinsonde station observations.”

The 2–7 hPa region is where the SAO, which is prominent in the stratopause level above, transitions to the QBO below. The presence of the QBO makes parts of the SAO difficult to see in the raw data shown in the first two panels of figure 3.1: during a QBO easterly phase, the w-SAO and easterly phases of the SAO (e-SAO) are imbedded in an easterly background and show up only as relative easterly maxima and minima. The alternating e-SAO and w-SAO are seen when we remove the QBO by averaging over all Januaries, Februaries etc. in the entire ERA-40 record. This is done in the last two panels in figure 3.1 for 1–3 hPa. It is also seen in figure 3.1 that the w-QBO always starts with a w-SAO above, and one period of the QBO terminates when the westerly phase of the following QBO starts similarly with the descent of another w-SAO. This is as hypothesized originally by Lindzen and Holton (1968). The reason that it is the w-SAO, but not its e-SAO that initiates a QBO below is explained as: since the equatorial upper stratosphere is easterly without the SAO, the e-SAO does not introduce a zero-wind line, but the w-SAO does. A zero-wind line is where enhanced wave-mean flow interaction occurs. Therefore, at and immediately below the zero-wind line introduced by the w-SAO, westerly wave momentum is deposited, causing the descent of the westerly shear zone, provided that the westerly waves are allowed to propagate up from the lower to the upper stratosphere. This happens when the westerly shear zone at the 50–70 hPa region, which shields waves of westerly phase speeds from propagating upward, breaks down at the appropriate time in the QBO's life cycle (see later). Therefore not all w-SAOs initiate a QBO. Since a QBO period always starts and terminates with a w-SAO, the period of the QBO should be an integer multiple of the SAO period, at least in the upper stratosphere.

To verify this hypothesis, we show in figure 3.2a the QBO period at 5 hPa in months. (The descent of the QBO in lower levels may be affected by the variable upwelling rate in the tropics. Higher than the 5 hPa level the SAO signal is comingled with the QBO signal.) A QBO period is measured in the raw monthly mean data by the time interval between the two zero crossings when the wind shifts from easterly to westerly. There are a few instances when a w-SAO descends to the usual QBO altitude at 5 hPa but for some reason (possibly because of the persistence of the westerly wind below 50 hPa that prevents the upward propagations of westerly waves) fails to initiate a QBO below 5–7 hPa. One such example is just before 1963. The QBO period starts instead with the next SAO. Another such case occurs during the QBO of 1987–1989. In this case it is clear, by looking at the QBO below 10 hPa, that the failed initiation of the QBO in mid 1986 should not be regarded as the starting point of the QBO, which actually started in 1987, one SAO period later. Similarly for the QBO onset in 1992, and in 1984. After adjusting for these failed initiations of the QBO by some SAO, the QBO periods cluster around 24 months and 30 months. Counting of the periods of QBO and SAO by zero-wind crossing is not sufficiently accurate because of the presence of a variable mean easterly flow, which makes the SAO period appear to be not exactly 6 months, which accounts for the two cases of 25 month period and the two cases of 29 month period. One could alternatively count the QBO period in units of SAO period using the lower two panels of Figure 3.1, and one finds that the QBO periods are either 4-SAO period long or 5-SAO periods long in the ERA-40 record.

Figure 3.2b is the histogram of the number of occurrences of the QBO period in month for the 45-year ERA-40 data. It is seen that the reported mean period of 28 months for the QBO during this period of record is an average of six QBO periods each lasting 4-SAO periods (on average 24 months), and twelve QBO periods when it is 5-SAO periods (on average 30 months). In figure 3.2c, we show the vertical profiles of two individual QBO periods (one starting in 1962 (5-SAO) and the other in 1997 (4-SAO)), along with the mean period of all the QBOs in the ERA-40 record. We see that, not surprisingly, the mean QBO period is constant with height (as also shown in figure 3.2c of Gabis and Troshichev (2006)). Individual QBO periods are slightly more variable, but can be regarded as almost constant, within ± 1 month between 1–40 hPa, consistent with Fischer and Tung (2008), although we have found 2-month deviations in the lower stratosphere in some cases. Dunkerton (1990) found strong annual modulations of the onset of QBO even at 10 hPa and 50 hPa. He found that the transition of the westerly to easterly QBO at 50 hPa rarely occurs in Northern winter.

Figure 3.2a shows that there are interesting decadal variations in the QBO period, and that such variation takes the form of discrete jumps in integral multiples of SAO periods. The cause of the decadal variation of the QBO period in the lower stratosphere is a topic of current debate (Salby and Callaghan, 2000; Soukharev and Hood, 2001; Pascoe et al., 2005; Hamilton, 2002; Fischer and Tung, 2008). It is however apparent from this figure that such changes in QBO period in the upper stratosphere are not correlated (or anticorrelated) with the 11-year solar cycle (SC); the total solar irradiance (Lean, 2004) is indicated by the solid curve at the bottom of figure 3.2a. Note, however, that this result

concerns the whole period of the QBO and does not necessarily apply to the question of whether the westerly portion of the QBO is correlated with the solar cycle.

An additional interesting result is that the jumps in the QBO period that we see in the ERA-40 data (in figure 3.1 or 3.2) above is not only seen in our model result (to be presented in section 3) with a periodic solar cycle forcing, but is also present in model runs with perpetual solar maxima (SC-max) or solar minima (SC-min) or solar mean (SC-mean) forcing. This suggests that the nonstationary jumps in QBO period are probably not a result of the variable solar-cycle forcing, but are a property intrinsic to the QBO phenomenon itself.

3.3 QBO from THINAIR Model

3.3.1 Model

The THINAIR (two and a half dimensional interactive Isentropic Research) is an isentropic coordinate chemical-radiative-dynamical model (Kinnersley and Harwood, 1993). The model has zonally averaged dynamics and includes the three longest planetary waves, which are prescribed by observations at the tropopause level. For this study, the planetary wave forcing at the tropopause is fixed at the 1979-year level derived from NCEP reanalysis data (Kalnay, et al., 1996; Kistler, et al., 2001), annually periodic and repeated for all years. This choice reduces interannual variability of the planetary wave forcing, so that this variability in forcing is eliminated as a cause of the observed nonstationary behavior of the QBO period. It removes tropospheric variability of

planetary waves, but retains stratospheric variability of the planetary waves that is internally generated through wave propagation in a changing mean flow and wave-mean flow interaction. The model uses an isentropic vertical coordinate above 350 K. Below 350 K a hybrid coordinate is used to avoid intersection of the coordinate layers with the ground. The version used in this study has 29 layers from the ground to ~100 km for dynamics and 17 layers from ground to ~60 km for chemistry. The model has 19 meridional grid points evenly distributed from pole to pole. The QBO-source term in the momentum equation uses parameterization of wave momentum fluxes from Kelvin wave, and Rossby-gravity wave (in the form of a Kelvin wave with a westerly phase speed). (Kinnersley and Pawson, 1996).

UARS/SUSIM spectral irradiance observations are used to simulate the 11-year SC. UARS/SUSIM data consists of the solar spectrum in 119–400 nm during 1991–2002, with 1 nm resolution. The monthly data are extended to 1947–2005 using F10.7 cm as a proxy (Jackman, et al. 1996). The yearly averaged data are integrated to give photon fluxes in wavelength intervals appropriate for the THINAIR model. The general performance of the model has been evaluated by Kinnersley and Pawson (1996). To avoid redoing the climatology with the new solar forcing, the UARS/SUSIM SC-mean is scaled to the SC-mean of the THINAIR model, which is based on Lean (2004).

3.3.2 Time-Varying Solar Cycle Run

A 200-hundred year run is made using the realistic, time-varying solar cycle forcing for 1964–1995 from UARS/SUSIM (extended as described above) and repeated thereafter.

Even in this long run, the period of the QBO does not settle down to a fixed number, but still executes apparently irregular jumps in period. Another 400-year run is carried out to show that the statistical properties in the 200-year run have settled down (in particular the histograms of the distributions for the 200-year run and the 400-year run are the same). The behavior of the QBO period in the model is remarkably similar to the observation discussed above, including features such as QBO westerly synchronized with the SAO westerly in the upper stratosphere, and the QBO westerly sometimes stalling below 50 hPa. As in the observation some SAO also fail to initiate a QBO in the model, but the frequency of such occurrences is smaller in the model. Importantly, the model QBO period also jumps from 4-SAO periods to 5-SAO periods in a nonstationary manner. Figure 3.3 shows a height-time cross section of the mean zonal wind at the equator from the model. Figure 3.4 can be used to compare the period of model QBO with that from ERA-40 shown in figure 3.2. The number of 5-SAO periods is about equal to the number of 4-SAO periods in both the 200- and 400-year runs, and so the frequency of the 5-SAO periods relative to the 4-SAO periods is less than in the 45 years of the ERA-40 data. However, in different smaller time segments of about 45 years from the model, corresponding to the period of ERA-40 data, the distribution can shift. In the segment shown, which is from year 126 to year 172 in the 400-year model run, there are more 5-SAO periods than 4-SAO periods, as in the ERA-40 data (figure 3.4b).

3.3.3 Perpetual Solar Forcing Runs

Additionally, we perform constant solar-cycle forcing experiments in our model to answer the question of whether the nonstationary nature of the QBO period is caused by

the fact that the solar-cycle forcing is time varying. (It should be pointed out that we still have the seasonal cycle in perpetual solar runs.) Figure 3.5 is similar to figure 3.3 except for perpetual SC-mean forcing, in the 200-year runs. There are no qualitative differences between the perpetual solar forcing run and the variable solar-cycle forcing run. In particular, the QBO period still jumps irregularly from 4-SAO periods to 5-SAO periods and back. We therefore conclude that the nonstationary nature of the QBO period is not caused by decadal variability in the solar-cycle forcing.

3.4 A Possible Mechanism for QBO-SAO Synchronization

In the original theory of the QBO by Lindzen and Holton (1968) the presence of the mesospheric SAO above the QBO is needed to restore the flow to a direction that is opposite to the zonal flow at the lower stratosphere. Later publications, however, have tended to deemphasize the essential role of the SAO in seeding the QBO, following the conclusion of Holton and Lindzen (1972) that “The mesospheric semiannual oscillation, while important, is no longer absolutely essential to the overall theory” (Holton was reportedly uneasy with this statement; see Lindzen (1987)). Plumb (1977) also argued that the SAO is unnecessary for the QBO. Neither model, however, incorporated the easterly bias of the equatorial zonal flow on a rotating planet: Without the SAO the equatorial upper stratosphere near the stratopause is generally easterly, making it difficult for initiating a w-QBO. Note that the assumed form of mean zonal flow is westerly in the upper stratosphere in the original model of Lindzen and Holton (1968), and there is a SAO in the numerical model of Holton and Lindzen (1972) that provided the westerly

flow in the upper levels. While it is not “absolutely essential” to have the SAO since a highly nonlinear wave breaking event can initiate a westerly descent by itself, without the SAO the initiation of the westerly descent probably would have occurred higher up, in the mesosphere.

As the w-QBO descends into the lower stratosphere with denser and denser air, it stalls usually at the 70 hPa level. Upward propagating waves with phase speed in the same direction as the lower stratospheric zonal flow, westerly in this phase of the QBO, meet their critical level in the lower stratosphere (where the phase speed equals the mean wind speed) and are absorbed near or below this level. They are thus prevented from propagating further upward. Waves of opposite (easterly) phase speed can however freely propagate up. These (easterly) waves encounter an easterly zonal flow, deposit their easterly momentum and subsequently bring the easterly jet to lower and lower altitudes, replacing the westerly flow below it. In the simple models mentioned above, the westerly jet near 70 hPa becomes thinner and thinner in the process, and eventually breaks due to flow instability. This then allows the propagation of westerly waves into the upper stratosphere. Since the equatorial upper stratosphere and mesosphere are generally easterly without the SAO, these westerly waves do not meet their critical level and the descent of the westerly zonal flow cannot be initiated (in the quasi-linear model of Lindzen and Holton (1968)) in the absence of the SAO. Therefore the SAO plays an important role in initiating the alternating easterly and westerly descents of the zonal wind in a QBO. It follows then that the period of the QBO, at least in the upper stratosphere, should be synchronized with the SAO. In particular, the westerly phase of

the QBO should be synchronized with the w-SAO, as it is observed to do in the ERA-40 data presented in section 2. The initiation of the easterly phase of the QBO does not need the SAO.

The above discussion explains that, given there is a SAO at the stratopause, the initiation of the westerly phase of the QBO should be synchronized with the w-SAO. It then follows that the QBO period in the upper stratosphere should be an integer multiple of the SAO period. The remaining question is, why does the QBO period jump from one SAO multiple to another SAO multiple? One suggestion could have been that it is the variable solar-cycle forcing that alters the QBO period, but this effect is found to be negligible in our model. There is no correlation or anticorrelation of the QBO period with the solar cycle in either the observation or in the model. (We are not addressing here the issue of whether the westerly phase duration of the QBO is anticorrelated with the solar cycle, as reviewed by Fischer and Tung (2008); the modeling work is left to a separate chapter.) Furthermore, we find that the nonstationary jumps still occur even when there is no solar-cycle variability. An explanation of this nonstationary behavior appears to be the following: the intrinsic period of the QBO is determined by the internal dynamics of the wave-mean flow system. Plumb (1977) gave a simple formula for the simplified cases: the period T is proportional to the cube of the phase speed c of the forcing wave and inversely proportional to the magnitude of the wave forcing F . This intrinsic period, however, may not be compatible with the period determined by the SAO. For the case where the intrinsic QBO period lies between 4-SAO and 5-SAO periods, a predicted transition from e-QBO to w-QBO would have to occur in a SAO easterly flow, which is

difficult. Instead the transition would be delayed to the next w-SAO phase. This is consistent with the conceptual model discussed in Lindzen and Holton (1968). However, that this is the cause for the nonstationary behavior has not been pointed out previously. Nonstationary jumps are needed so that the long term averaged period is close to the intrinsic period. Compatibility with the QBO's period is necessary, and explains why not all w-SAOs initiate a QBO. As discussed previously, the initiation of the w-QBO by a w-SAO has to wait until in the life cycle of the QBO in the lower stratosphere when westerly equatorial waves are not blocked from propagating upward.

If the intrinsic period of the QBO is already an integer multiple of the SAO period, the QBO period would be phase-locked with that SAO multiple and the nonstationary jumps would disappear, if this explanation is correct.

3.4.1 Parametric Study

We can test this hypothesis in our model in a parametric study by changing the QBO wave forcing F . We show that in a parametric diagram of the QBO period involving F , nonstationary regimes are separated by islands (actually lines) of phase-locking (and hence stationary behavior).

The westerly forcing by a Kelvin wave is parameterized as in Gray and Pyle (1989), while the easterly forcing in this model by Rossby-Gravity wave differs from the Kelvin wave only in its opposite zonal phase speed (Kinnnersley and Pawson, 1996). The expression for the wave-induced zonal force per unit mass is defined as following by

$$F(z) = \exp\left(\frac{z-z_0}{H}\right) \sum_{i=1}^2 A_i R(z, c_i) \exp(-P_i(z)), \quad (3.1)$$

where

$$R(z, c_i) = \frac{\alpha(z)N}{k_i(\bar{u} - c_i)^2}, \quad (3.2)$$

$$P_i(z) = \int_{z_0}^z R(z) dz, \quad (3.3)$$

Here $i=1$ is for the Kelvin wave and $i=2$ is for the Rossby-Gravity wave. $C_1 (>0)$ is the phase speed (m s^{-1}) for Kelvin wave while $c_2 (<0)$ is the Rossby-Gravity wave phase speed. A_i is the amplitude of vertical momentum flux at z_0 in unit ($\text{m}^2 \text{s}^{-1}$). For the baseline case in figure 3.6b, $A_1=2.7 \times 10^{-3} \text{ m}^2 \text{ s}^{-1}$ and $A_2=-2.7 \times 10^{-3} \text{ m}^2 \text{ s}^{-1}$; $\alpha(z)$ =thermal damping rate; N =Brunt-Väisälä frequency; k_i =zonal wavenumber; \bar{u} =zonal wind speed.

In our study of the sensitivity of the QBO period to wave forcing, the phase speed is not changed. We tune the total wave forcing $F(z)$ on the QBO in our model by varying the parameters A_i in equations by a constant factor (see table 3.1) from their baseline values.

The result is shown in figure 3.6. As predicted by Plumb (1977), the QBO period decreases (increases) as we increase (decrease) F from our baseline case of SC-mean (case (b)). For a value of F that yields a mean QBO period of 24 or 30 months, nonstationary behavior disappears, because now the intrinsic period is synchronized with the SAO period, being an integer multiple of the latter's period. Nonstationary behavior returns when the magnitude of F lies between and away from these values.

3.5 Conclusions

Using ERA-40 data, which extends to the stratopause region and encompasses both the SAO and QBO, we find that the period of the QBO is always an integer multiple of the SAO period. The w-QBO always corresponds to a w-SAO above. A plausible explanation is provided, consistent with the original explanation of Lindzen and Holton (1968). Although a SAO is not “absolutely necessary” for seeding the QBO below, the w-SAO facilitates the initiation of the w-QBO. Since the equatorial upper stratosphere has an easterly bias in the absence of the SAO, as it should by angular momentum considerations on an eastward rotating planet, the initiation of the w-QBO would have become more difficult in the absence of the SAO and thus should have occurred higher up in the mesosphere than observed. We have also shown that since there is very little variation of the QBO period in the vertical (within limits of about 1 to 2 months), the same synchronization with the SAO should also hold throughout the stratosphere, to that accuracy.

A second interesting feature of the observed behavior of the QBO period is that it jumps from 4-SAO periods to 5-SAO periods and back in a seemingly random way. This nonstationary behavior is explained using a model. In our model we show that the nonstationary behavior is not due to the fact that the solar-cycle forcing is time varying, because the same behavior remains when we remove the solar cycle in our perpetual SC-mean run (see the comparison between figures 3.3 and 3.5). An alternative explanation is that the magnitude of wave forcing in our current climate is consistent with a QBO period

intermediate between 4-SAO and 5-SAO, and so the period of the QBO determined by its internal forcing mechanism is incompatible with the external constraint provided by the SAO. To maintain synchronization with the SAO period, the QBO period jumps in a nonstationary way so that a long-term average of its period is compatible with its intrinsic wave forcing. If this explanation is correct, then we should be able to find a different behavior for a different wave forcing, larger or smaller than the value for the current climate, for which the intrinsic period is an integer multiple of the SAO period. Under such a condition, the nonstationary behavior should disappear. This is indeed the case, and the QBO period locks into 4- (or 5-SAO) periods, when the relative forcing is increased (or decreased) by $\sim 10\%$ (see figure 3.6).

3.6 Acknowledgements

This work was supported in part by NASA grants NAG1-1806 and NNG04GN02G to the California Institute of Technology. K. K. Tung's research was supported by NSF grants ATM 0332364 and ATM 0808375 to University of Washington. We would like to thank A. Ruzmaikin and J. Feynman for useful discussions and K. F. Li for his calculation of the solar cycle variation in solar flux data and helpful suggestions. We also acknowledge help in improving the paper from M. C. Liang, N. Heavens, X. Guo, A. Soto and T. Lee, X. Zhang, P. S. Jiang, Y. C. Chen, D. Yang, C. D. Camp.

3.7 References

- Angell, J. K., and Korshove, J., 1970: Quasi-biennial, annual, and semiannual zonal wind and temperature harmonic amplitudes and phases in stratosphere and low mesosphere of northern hemisphere. *J. Geophys. Res.*, **75**, 543–550.
- Baldwin, M. P., and T. J. Dunkerton, 1999: Propagation of the Arctic Oscillation from the stratosphere to the troposphere, *J. Geophys. Res.*, **104**(D24), 30937–30946.
- , 2001: The quasi-biennial oscillation, *Rev. Geophys.*, **39**(2), 179–229.
- , 2005: Tropical stratospheric zonal winds in ECMWF ERA-40 reanalysis, rocketsonde data, and rawinsonde data. *Geophys. Res. Lett.*, **32**, doi:10.1029/2004GL022328.
- Dunkerton, T. J., 1990: Annual variation of deseasonalized mean flow acceleration in the equatorial lower stratosphere. *J. Meteor. Soc. Japan*, **68**, 499–508.
- , 1997a: The role of gravity waves in the quasi-biennial oscillation, *J. Geophys. Res.*, **102**(D22), 26053–26076.
- , 1997b: Interaction of the quasi-biennial oscillation and stratopause semiannual oscillation, *J. Geophys. Res.*, **102**(D22), 26107–26116.
- Ebdon, R. A., and R. G. Veryard, 1961: Fluctuations in tropical stratospheric winds, *Nature*, **189**(476), 791–793.
- Fischer, P., and K. K. Tung, 2008: A reexamination of the QBO period modulation by the solar cycle, *J. Geophys. Res.—Atmos.*, **113**(D07114), doi:10.1029/2007JD008983.

- Gabis, I., and O. Troshichev, 2006: Influence of solar UV irradiance on the quasi-biennial oscillation of zonal winds in the equatorial stratosphere, *J. Atmos. Sol.—Terr. Phys.*, **68**, 1987–1999.
- Gray, L. J., and J. A. Pyle, 1989: A two-dimensional model of the quasi-biennial oscillation of ozone, *J. Atmos. Sci.*, **46**, 203–220.
- Hamilton, K., 2002: On the quasi-decadal modulation of the stratospheric QBO period. *J. Climate*, **15**, 2562–2565.
- Hasebe, F., 1983: Interannual variations of global total ozone revealed from Nimbus 4-Buv and ground-based observations, *J. Geophys. Res.*, **88**(NC11), 6819–6834.
- Holton, J. R., and R. S. Lindzen, 1972: Updated theory for quasi-biennial cycle of tropical stratosphere, *J. Atmos. Sci.*, **29**(6), 1076–1080.
- , 1980: The influence of the equatorial quasi-biennial oscillation on the global circulation at 50 mb, *J. Atmos. Sci.*, **37**(10), 2200–2208.
- , 1982: The quasi-biennial oscillation in the northern hemisphere lower stratosphere, *J. Meteor. Soc. Japan*, **60**(1), 140–148.
- Jackman, C., E. L. Fleming, S. Chandra, D. B. Considine, and J. E. Rosenfield, 1996: Past, present, and future modeled ozone trends with comparisons to observed trends, *J. Geophys. Res.*, **101**(D22), 28753–28767.
- Kalnay, E., M. Kanamitsu, R. Kistler, W. Collins, D. Deaven, L. Gandin, M. Iredell, S. Saha, G. White, J. Woollen, Y. Zhu, M. Chelliah, W. Ebisuzaki, W. Higgins, J. Janowiak, K. C. Mo, C. Ropelewski, J. Wang, A. Leetmaa, R. Reynolds, R. Jenne, and D. Joseph, 1996: The NCEP/NCAR 40-year reanalysis project, *Bull. Am. Meteorol. Soc.*, **77**(3), 437–471.

- Kinnersley, J. S., and R. S. Harwood, 1993: An isentropic 2-dimensional model with an interactive parameterization of dynamical and chemical planetary-wave fluxes, *Q. J. R. Meteorol. Soc.*, **119**(513), 1167–1193.
- , 1996: The descent rates of the shear zones of the equatorial QBO, *J. Atmos. Sci.*, **53**(14), 1937–1949.
- Kistler, R., E. Kalnay, W. Collins, S. Saha, G. White, J. Woollen, M. Chelliah, W. Ebisuzaki, M. Kanamitsu, V. Kousky, H. van den Dool, R. Jenne, and M. Fiorino, 2001: The NCEP–NCAR 50-year reanalysis: Monthly means CD-ROM and documentation, *Bull. Am. Meteorol. Soc.*, 247–267.
- Lean, J., 2004: “Solar Irradiance Reconstruction”, IGBP PAGES/World Data Center for Paleoclimatology Data Contribution Series # 2004–035. NOAA/NGDC Paleoclimatology Program, Boulder CO, USA. Data are downloaded from http://gcmd.nasa.gov/records/GCMD_NOAA_NCDC_PALEO_2004-035.html.
- Lindzen, R. S., and J. R. Holton, 1968: A theory of the quasi-biennial oscillation, *J. Atmos. Sci.*, **25**, 1095–1107.
- , 1987: On the development of the theory of the QBO, *Bull. Amer. Meteorol. Soc.*, **68**, 329–337.
- Oltmans, S.J., and J. London, 1982: The quasi-biennial oscillation in atmospheric ozone, *J. Geophys. Res.*, **87**(NC11), 8981–8989.
- Pascoe, C. L., L. J. Gray, S. A. Crooks, M. N. Juckes, and M. P. Baldwin, 2005: The quasi-biennial oscillation: Analysis using ERA-40 data. *J. Geophys. Res.*, **110**, D08105.

- Pawson, S., and M. Fiorino, 1998: A comparison of reanalyses in the tropical stratosphere. Part 2: The quasi biennial oscillation. *Climate Dynamics*, **14**, 645–658.
- Plumb, R. A., 1977: Interaction of 2 internal waves with mean flow-implications for theory of quasi-biennial oscillation, *J. Atmos. Sci.*, *34*(12), 1847–1858.
- Randel, W.J., and F. Wu, 1996: Isolation of the ozone QBO in SAGE II data by singular-value decomposition, *J. Atmos. Sci.*, **53**(17), 2546–2559.
- Reed, R. J., L. A. Rasmusse, W. J. Campbell, and D. G. Rogers, 1961: Evidence of a downward propagating, annual wind reversal in equatorial stratosphere, *J. Geophys. Res.*, **66**(3), 813–818.
- Ruzmaikin, A., J. Feynman, X. Jiang, and Y. L. Yung, 2005: The extratropical signature of the Quasi-Biennial Oscillation, *J. Geophys. Res.*, **110**(D11), doi:10.1029/2004JD005382.
- Salby, M. and P. Callaghan, 2000: Connection between the solar cycle and the QBO: The missing link. *J. Climate*, **13**, 2652–2662.
- Soukharev, B. E. and L. L. Hood, 2001: Possible solar modulation of the equatorial quasi-biennial oscillation: Additional statistical evidence. *J. Geophys. Res.*, **106**, 14855–14868.
- Tung, K. K. and H. Yang, 1994a: Global QBO in circulation and ozone .1. reexamination of observational Evidence. *J. Atmos. Sci.*, **51**, 2699–2707.
- , 1994b: Global QBO in Circulation and Ozone, .2. A simple mechanistic model. *J. Atmos. Sci.*, **51**, 3365–3365.
- Uppala S. M. , P. W. Kallberg, A. J. Simmons, U. Andrae, V. Da Costa Bechtold, M. Fiorino, J. K. Gibson, J. Haseler, A. Hernandez, G. A. Kelly, X. Li, K. Onogi, S.

Saarinen, N. Sokka, R. P. Allan, E. Andersson, K. Arpe, M. A. Balmaseda, A. C. M. Beljaars, L. Van De Berg, J. Bidlot, N. Bormann, S. Caires, F. Chevallier, A. Dethof, M. Dragosavac, M. Fisher, M. Fuentes, S. Hagemann, E. Holm, B. J. Hoskins, L. Isaksen, P. A. E. M. Janssen, R. Jenne, A. P. McNally, J.-F. Mahfouf, J.-J. Morcrette, N. A. Rayner, R. W. Saunders, P. Simon, A. Sterl, K. E. Trenberth, A. Untch, D. Vasiljevic, P. Viterbo, and J. Woollen, 2005: The ERA-40 re-analysis, *Quart. J. Roy. Meteor. Soc.*, **131**, 2961–3012.

Zawodny, J. M., and M.P. McCormick, 1991: Stratospheric Aerosol and Gas Experiment-II Measurements of the Quasi-Biennial Oscillations in Ozone and Nitrogen-Dioxide, *J. Geophys. Res.*, **96**(D5), 9371–9377.

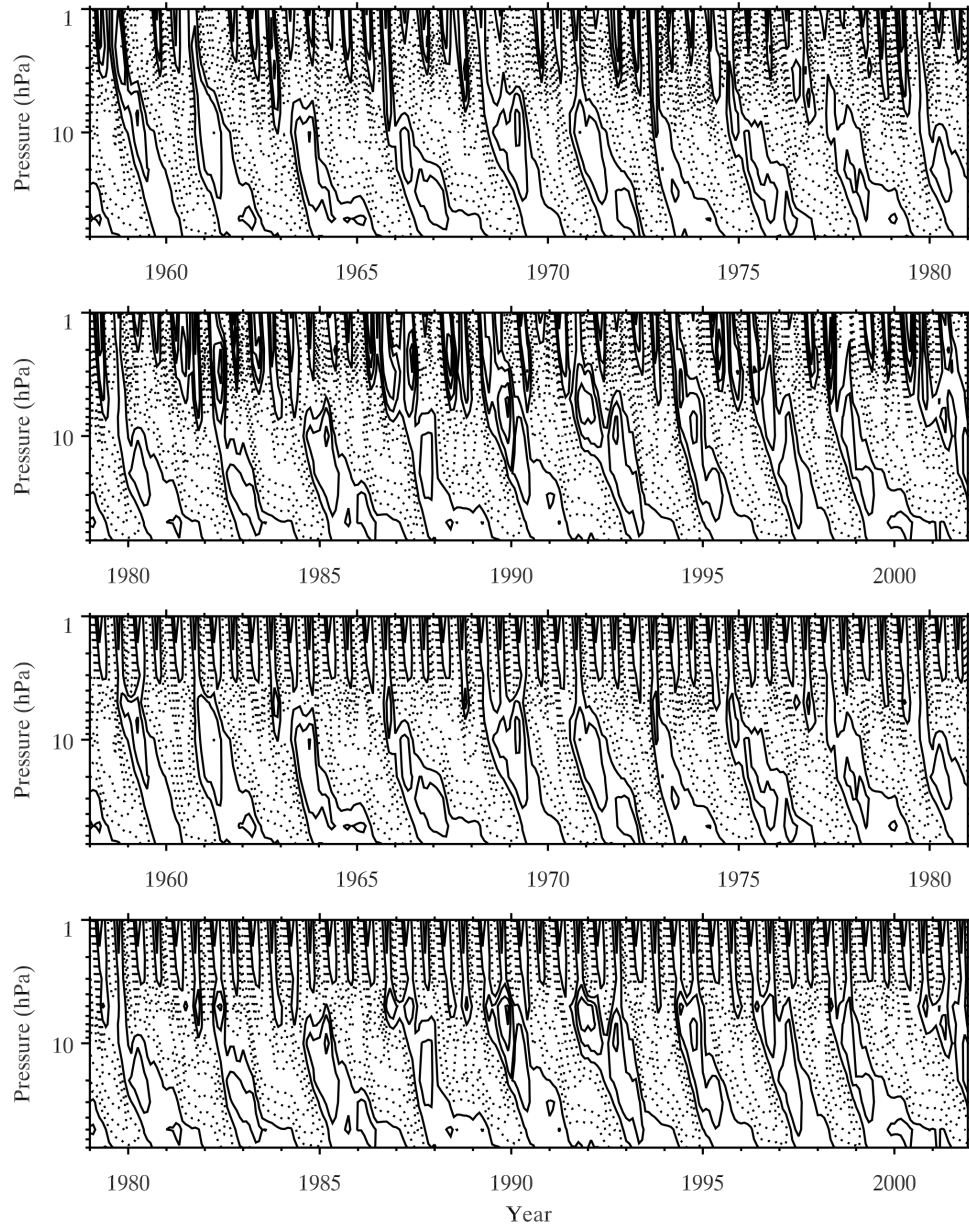


Figure 3.1 Height-time crosssection of the monthly mean ERA-40 zonal mean zonal wind (top two panels). The contour interval is 10 m/s. Positive values are plotted in solid line. Negative values are plotted in dotted line. In the lower two panels, the zonal wind in the upper three levels (1, 2, 3 hPa) are replaced by its seasonal climatology, which removes the QBO and shows the SAO more clearly.

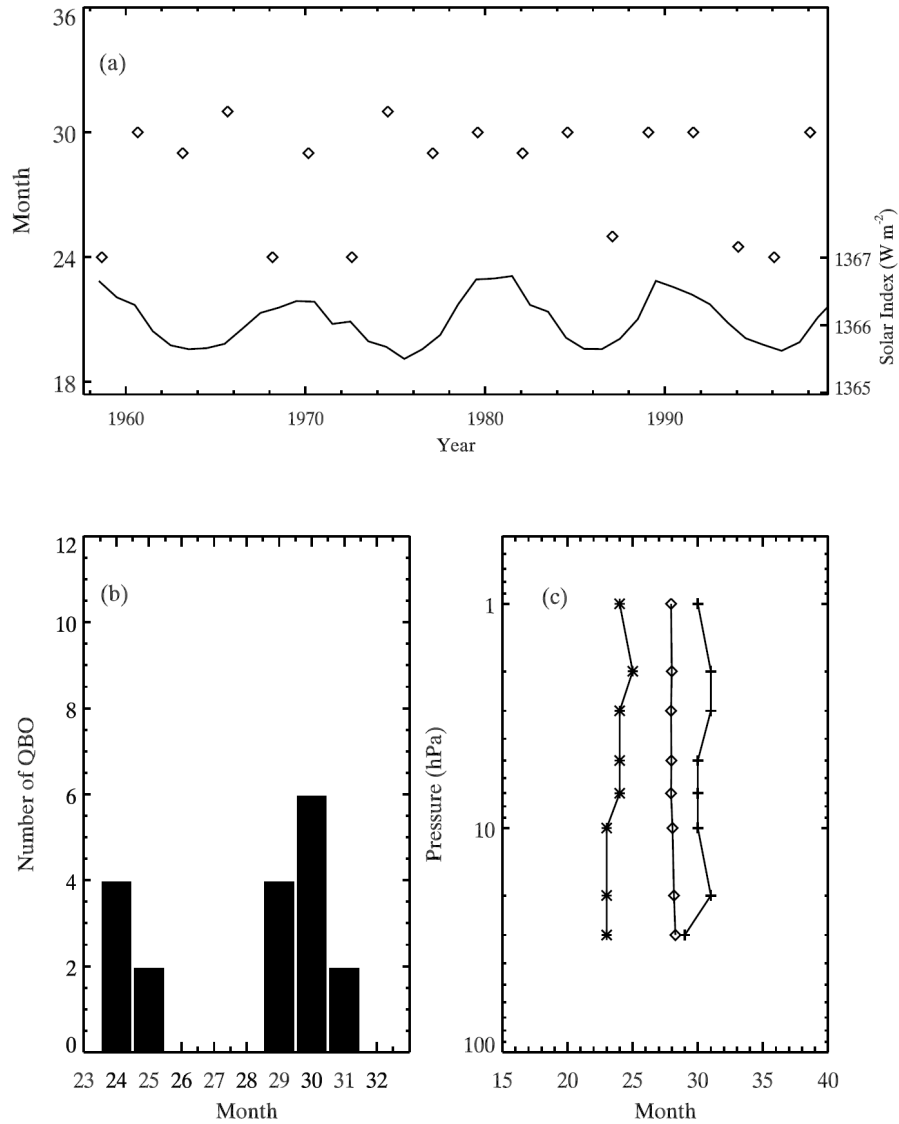


Figure 3.2 QBO period in ERA-40 data at 5 hPa. (a) QBO period in units of month (left scale). The solid curve at the bottom is the total solar irradiance (W m^{-2}) (right scale). (b) The histogram of the QBO period, counting the number of occurrences of the QBO period in months. (c) The QBO period as a function of pressure level. (*) represents the QBO during 1997, (+) represents the QBO during 1962, and diamonds represent the mean of all QBO periods in ERA-40 record.

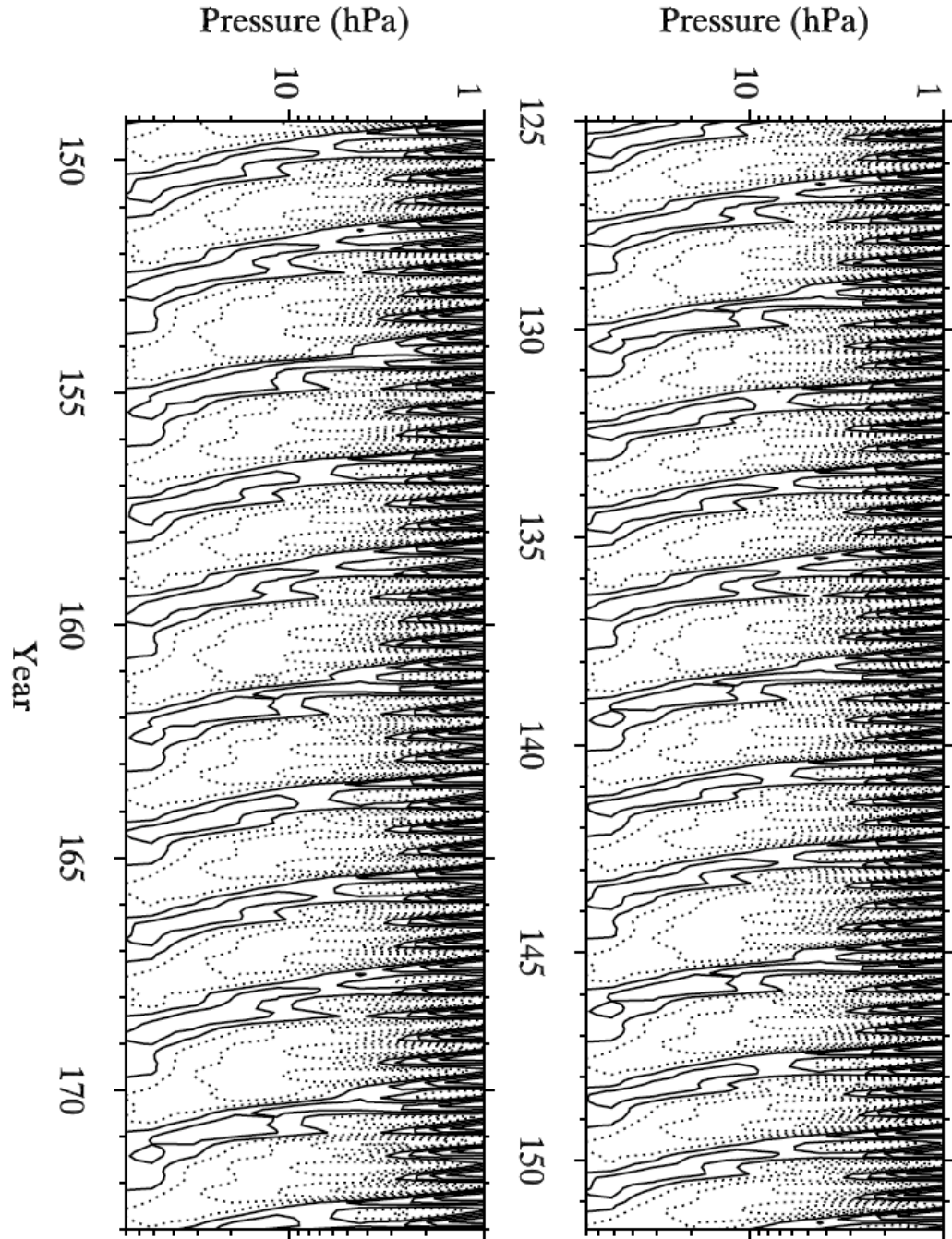


Figure 3.3 Height-time crosssection of zonal mean zonal wind for SC-varying case. The contour interval is 10 m/s. Positive values are plotted in solid line. Negative values are plotted in dotted line.

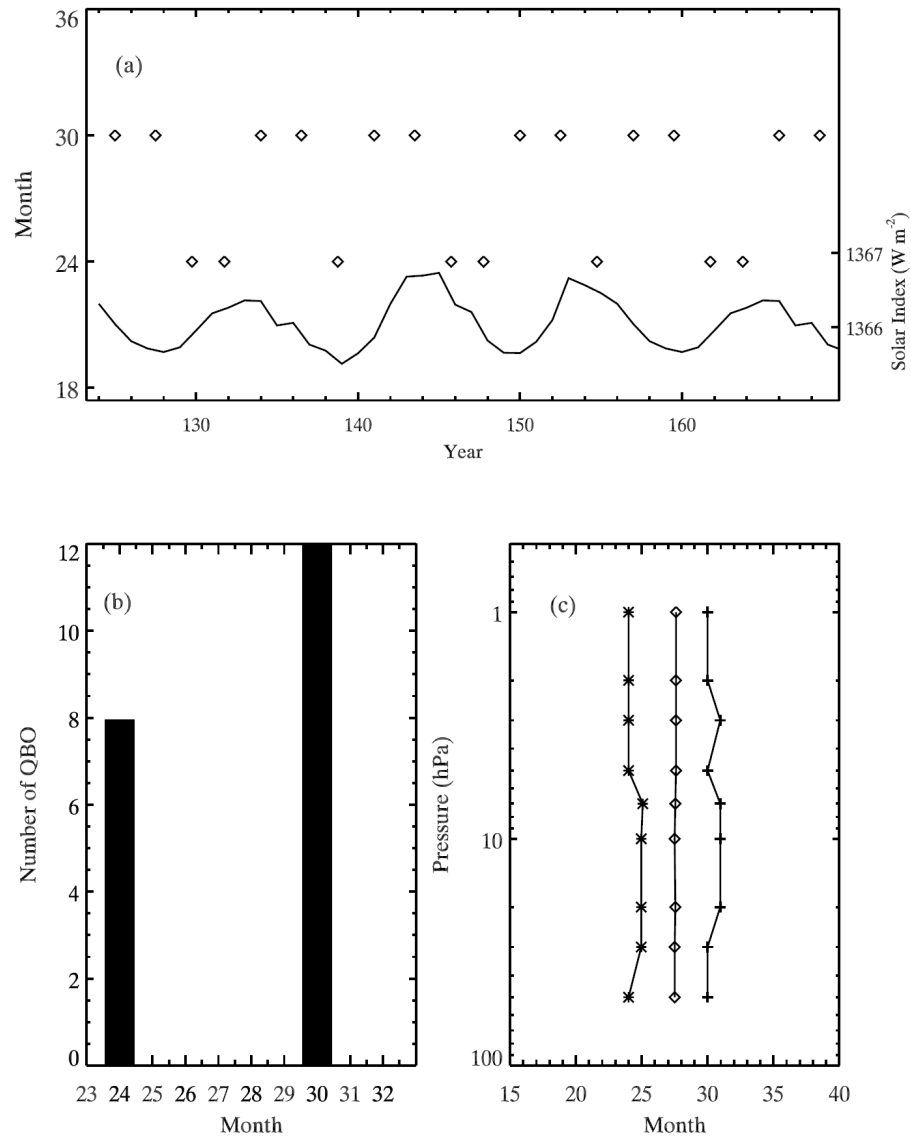


Figure 3.4 Same as figure 3.2 but for model results for the SC-varying case. The solid curve is the solar index as in figure 3.2 but repeating the data from 1964 to 1995 to cover 400 years. Here we choose 46 year out of 400 year run from 126 to 172. In (c) (*) represents the QBO in year 165 and (+) represents the QBO year 128. Diamonds represent the mean QBO periods during these 46 years.

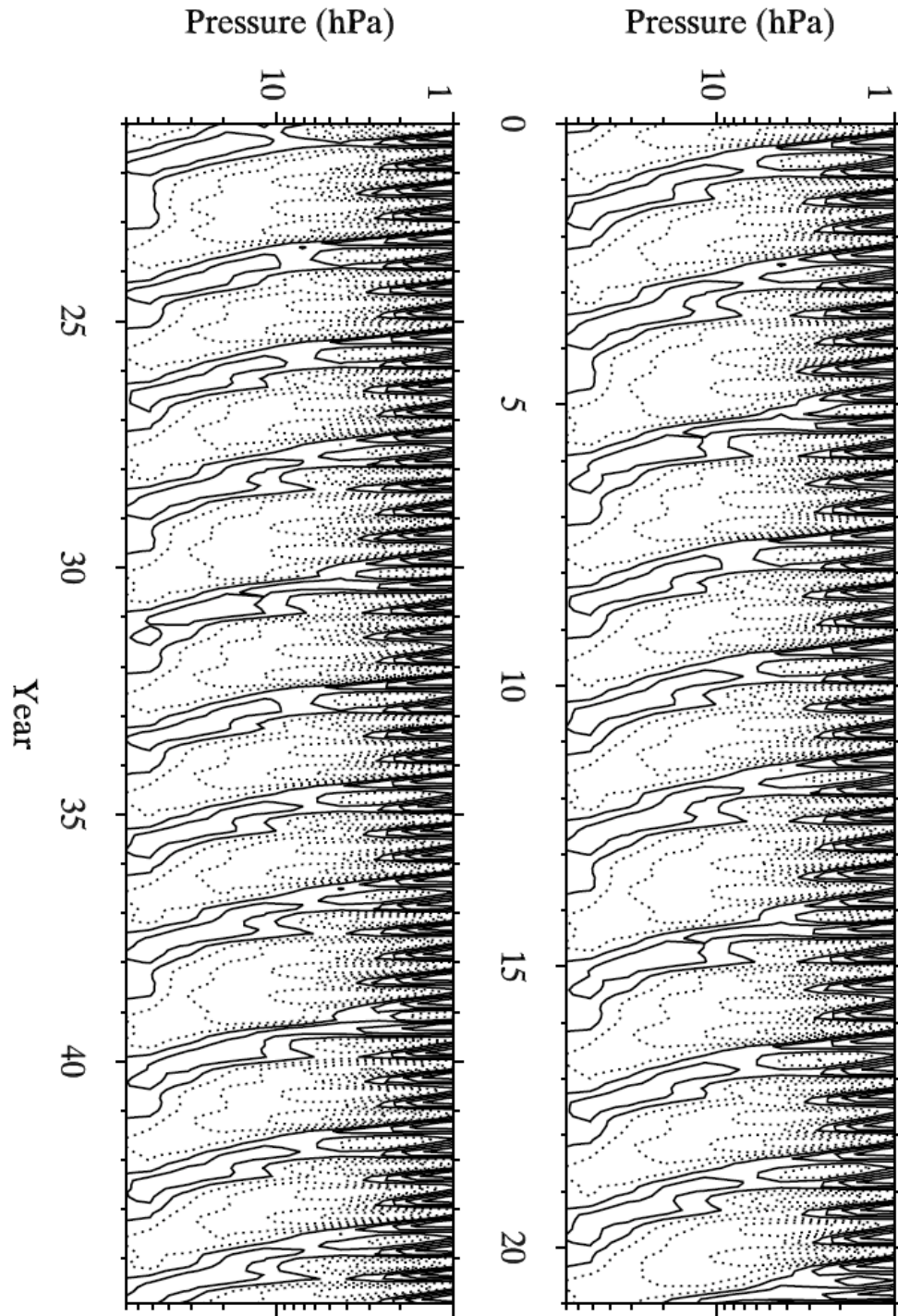


Figure 3.5 Height-time crosssection of zonal mean zonal wind for SC-mean case. The contour interval is 10 m/s. Positive values are plotted in solid line. Negative values are plotted in dotted line.

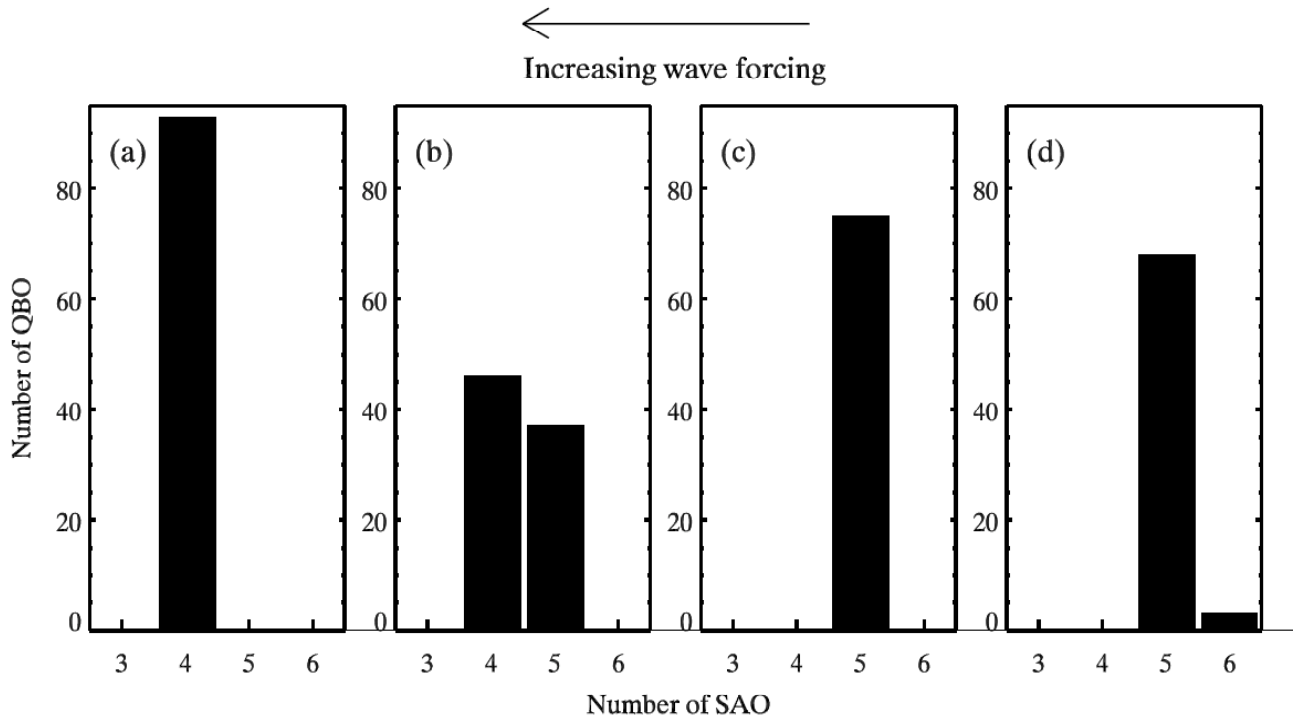


Figure 3.6 Histogram of the periods of the QBO for different wave forcings. See table 3.1 for details; case (b) is the baseline case, same as in figure 3.5.

Table 3.1 Parameters used to force the QBO in the THINAIR model

Phase speed	Kelvin wave	Rossby-Gravity wave
$c \text{ (m s}^{-1}\text{)}$	25	-30
Case	$A_1 / (A_1)_{\text{baseline}}$	$A_2 / (A_2)_{\text{baseline}}$
(a)	1	1.1
(b)	1	1
(c)	0.91	1
(d)	0.83	1.05

**Chapter 4: The Modulation on the Period of the Quasi-Biennial
Oscillation by the Solar Cycle**

Le Kuai^{1*}, Run-Lie Shia¹, Xun Jiang², Ka-Kit Tung³, Yuk L. Yung¹

1 Division of Geological and Planetary Sciences, California Institute of Technology, Pasadena, CA 91125

2 Department of Earth and Atmospheric Sciences, University of Houston, TX 77204

3 Department of Applied Mathematics, University of Washington, Seattle, WA 98195

Abstract

Using a two-and-a-half-dimensional THINAIR model, we examine the mechanism of solar-cycle modulation of the Quasi-Biennial Oscillation (QBO) period. Previous model results (using two-dimensional and three-dimensional models of varying complexity) have not convincingly established the proposed link of longer QBO periods during solar minima. Observational evidence for such a modulation is also controversial because it is only found during the period 1960s to early 1990s, which is contaminated by volcanic aerosols. In the model, 200- and 400-year runs without volcano influence can be obtained, long enough to establish some statistical robustness. Both in model and observed data, there is a strong synchronization of the QBO period with integer multiples of the semiannual oscillation (SAO) in the upper stratosphere. Under the current level of wave forcing, the period of the QBO jumps from one multiple of SAO to another and back so that it averages to 28 months, never settling down to a constant period. The “decadal” variability in the QBO period takes the form of “quantum” jumps, and these however do not appear to follow the level of the solar flux in either the observation or the model using realistic quasi-periodic solar cycle (SC) forcing. To understand the solar modulation of the QBO period, we perform model runs with a range of perpetual solar forcing, either lower or higher than the current level. At the current level of solar forcing, the model QBO period consists of a distribution of 4-SAO periods and 5-SAO periods, similar to the observed distribution. This distribution changes as solar forcing changes. For lower (higher) solar forcing, the distribution shifts to more (less) 4-SAO periods than 5-SAO periods. The record-averaged QBO period increases with the solar forcing.

However, because this effect is rather weak and is detectable only with exaggerated forcing, we suggest that the previous result of the anticorrelation of the QBO period with the SC seen in short observational records reflects only a chanced behavior of the QBO period, which naturally jumps in a nonstationary manner even if the solar forcing is held constant, and the correlation can change as the record gets longer.

4.1 Introduction

Quasi-Biennial Oscillation (QBO) is an internal oscillation of the equatorial zonal wind in the stratosphere involving wave-mean flow interactions (Holton and Lindzen, 1972; Dunkerton, 1997; Baldwin et al., 2001). There have been numerous observational studies of the QBO in the zonal wind, temperature, and ozone (e.g., Angell and Korshover, 1970; Oltmans and London, 1982; Hasebe, 1983; Zawodny and McCormick, 1991; Randel et al., 1996; Pawson and Fiorino, 1998). The period of the QBO averages to about 28 months but is known to have interannual variations of a few months about the average. While it is not surprising for this phenomenon arising from wave-mean flow interaction to have a variable period, the possibility that it could be affected by external forcing such as the 11-year solar cycle (SC) is intriguing.

Using radiosonde data from Free University of Berlin (FUB) near the equator at 45 hPa between 1956 and 1996, Salby and Callaghan (2000) found that the duration of the equatorial westerly phase QBO (w-QBO) appears to vary with the SC and tends to be longer during the solar minima (SC-min; we will use “SC-max” to refer to solar maxima). By comparison, the duration of the easterly phase of QBO (e-QBO) has little variability at that level, but has a decadal variation above 30 hPa. Soukharev and Hood (2001) extended the work of Salby and Callaghan (2000) using composite mean analysis of a similar dataset but at 50 to 10 hPa from 1957 to 1999. Their analysis also indicated that the duration of both QBO phases is longer during the SC-min. Pascoe et al. (2005) examined the ERA-40 data set (Uppala et al., 2005) from 1958 to 2001 to study the solar

modulation of the mean descent rate of the shear zone. They found that on average, it requires two more months for the easterly shear zone to descend from 20 to 44 hPa under the SC-min condition and that the w-QBO duration increases (decreases) under the SC-min (SC-max) condition. This relation, however, broke down during the 1990s. Later, Hamilton (2002) and Fischer and Tung (2008) employed longer FUB datasets and both found the opposite behavior in the 1950s, the late 1990s and 2000s. Although there is anticorrelation (correlation coefficient = -0.46) between the w-QBO duration at 50 hPa and the solar flux for the period of 1956–1996, Hamilton (2002) showed that the correlation coefficient is only -0.1 during the extended period of 1950–2001. Additionally, Fischer and Tung (2008), who applied the Continuous Wavelet Transform to determine the QBO period at 50 hPa for the longer record of 1953–2007, found that the correlation coefficient between the period of the QBO and a SC is practically zero. These later work did not contradict the findings of the earlier authors. They merely pointed out that the behavior of the 60s, 70s, 80s and early 90s were the opposite to that of the other decades before and after this period. A possible cause may be that the diabatic heating due to volcanic aerosols could lead to the stalling of the downward propagation of the QBO (Dunkerton, 1983). Fischer and Tung (2008) found that in the recent two decades when no large volcanic eruptions occurred, the previous anticorrelation disappeared and reverted to a positive correlation, which was also found prior to the 1960s. A few more decades without volcanic interference would be needed to obtain a statistically significant correlation with the SC. This complication can be circumvented in a modeling experiment.

An additional possibility considered here is that, with or without volcano aerosols in the stratosphere, the QBO period may respond to the solar flux in a nonstationary manner, with apparently random changes even without being perturbed by external forcing. The averaged effect on the QBO period by the solar-cycle forcing is detectable only if the record is over a hundred years long. Although such a long record is not available in observation, model results of over 200 years can be generated to test this hypothesis.

4.2 Relevant Features in ERA-40 Data

There are two characteristics of the observed behavior of the QBO that are relevant to the present study but have been underemphasized by previous modeling and observational discussions: its synchronization with the semiannual oscillation (SAO) in the upper stratosphere and the apparently random “quantum” jumps of the QBO period by a multiple of the SAO period. A detailed description of these features in the ERA-40 data (Uppala et al., 2005) and an explanation of possible causes can be found in Kuai et al., (2008). Here we briefly summarize the observational results for the purpose of comparing with our model results. Figure 4.1 shows the equatorial zonal wind as a function of height (up to 1 hPa) and years using ERA-40 data. The upper two panels display the original monthly mean data. For the lower two panels, in the region 1–3 hPa, where SAO and QBO coexist, the QBO is removed by long-term averaging. Only a climatological seasonal cycle, which shows the SAO prominently without the QBO, is displayed in the 1–3 hPa region. Below that the “raw” ERA-40 monthly zonal wind is again shown. A prominent SAO exists near the stratopause level and appears to be synchronized with the

QBO below 5 hPa. That is, the w-QBO is initiated from a westerly phase of the SAO (w-SAO), and the next QBO period starts when another w-SAO, four or five SAO periods later, descends below 10 hPa. Therefore, the QBO period is always an integer multiple of the SAO period, since the former always starts with the westerly descent of a SAO. In Figure 4.2, we show the observed QBO period at 5 hPa in units of a month, ignoring the false-start cases, when the SAO descends to 7 hPa but for some reason fails to initiate a QBO below 10 hPa. It becomes immediately apparent that the QBO period varies in a nonstationary manner, taking “quantum” jumps from 4-SAO periods to 5-SAO periods. Such variations are not correlated or anticorrelated with the SC (see the index of Total Solar Irradiance (TSI) plotted at the bottom of figure 4.2(a). Figure 4.2b is the histogram of the number of occurrences of the QBO period in month for the 45-year ERA-40 data. It is seen that the QBO period in the upper stratosphere clusters around 24 and 30 months, corresponding to 4 or 5 SAO periods. The synchronization of the QBO period with an integer multiple of the SAO period is actually better than what one can casually infer from figure 4.2b if we express instead the QBO period in units of the SAO period. This is because the SAO period inferred from observation is not exactly 6 months because the SAO is imbedded in a variable background wind. It is seen that the reported mean period of 28 months for the QBO during this period of record is an average of six QBO periods each lasting 4-SAO periods (on average 24 months), and twelve QBO periods when it is 5-SAO periods (on average 30 months). Figure 4.2(c) shows that there is very little vertical variation (usually within $\sim \pm 1$ month between 1 and 40 hPa, with an occasional 2 month deviation) of the QBO period in the ERA-40 data (see also Fischer and Tung (2008)).

4.3 Model

The THINAIR (two and a half dimensional interactive isentropic research) is an isentropic chemical-radiative-dynamical model. The model has zonally averaged radiation, chemistry and dynamics. It includes the three longest planetary waves, which are prescribed by observations at the tropopause level (Kinnersley and Harwood, 1993). For this study, the planetary wave forcing at the tropopause is fixed at the 1979 year level derived from NCEP reanalysis data (Kalnay, et al., 1996; Kistler, et al., 2001), annually periodic and repeated for all years. This choice reduces interannual variability of the planetary wave forcing, so that the (weak) influence of the SC on the QBO can be studied. It removes tropospheric variability of planetary waves, but retains stratospheric variability that is internally generated through wave-mean flow interaction and modulated by SC. The model uses an isentropic vertical coordinate above 350 K. Below 350 K a hybrid coordinate is used to avoid intersection of the coordinate layers with the ground. The version used in this study has 29 layers from the ground to ~100 km for dynamics and 17 layers from ground to ~60 km for chemistry. The model has 19 meridional grid points evenly distributed from pole to pole. The QBO source term in the momentum equation uses parameterization of wave momentum fluxes from Kelvin, “anti-Kelvin” (to represent the Rossby-gravity wave) and gravity waves (Kinnersley and Pawson, 1996). These momentum sources also partially force the SAO above the QBO. UARS/SUSIM spectral irradiance observation is used for the 11-year SC. UARS/SUSIM data consists of the solar spectrum in 119–400 nm during 1991–2002, with 1 nm resolution. The monthly data are extended to 1947–2005 using F10.7 cm as a proxy (Jackman, et al., 1996). The

yearly averaged data are integrated to give photon fluxes in wavelength intervals appropriate for the THINAIR model. The performance of the model has been reported in the literature (Kinnersley and Pawson, 1996). To avoid redoing the climatology of the model with the new UARS/SUSIM solar spectral forcing, we retain the mean SC forcing (SC-mean) in the original model and multiply it by the ratios (SC-max/SC-mean and SC-min/SC-mean using the UARS/SUSIM data) to create the SC-max forcing and SC-min forcing. This procedure is also necessitated by the fact that while the relative variation over a SC is well measured by the UARS/SUSIM instrument, the mean is not calibrated accurately because of possible long-term instrumental drifts.

4.4 Model Solar Influence on QBO Period

4.4.1 Time-Varying SC Run

A 400-year run is made using the realistic, time varying SC forcing for 1964–1995 from UARS/SUSIM (extended as described above) and repeated thereafter. The SC-mean of this record is scaled to the SC-mean of the THINAIR model as described above. Even in this long run, the period of the QBO does not settle down to a fixed number, but still executes apparently random jumps. The behavior of the QBO period is quite similar to what was found from the observations discussed above. In particular, the QBO period jumps from 4-SAO periods to 5-SAO periods and back, in a nonstationary manner. Figure 4.3 shows a height-time cross section of the zonal-mean zonal wind at the equator from the model for 1×SC-vary case. Figure 4.4 shows the distribution of model results for 1×SC-vary case from year 126 to year 172. The number of 5-SAO periods and 4-SAO

periods are about equal in this 400-year run. However, in different smaller time segments of about 40–46 years (20 QBOs) corresponding to the period of ERA-40 data, the distribution can shift. In some segments, there are more 5-SAO periods than 4-SAO periods (figure 4.5(c)), as in the ERA-40 data. In other segments of about 40–46 years, it can have equal number of 4-SAO and 5-SAO (figure 4.5(b) or more 4-SAO than 5-SAO (figure 4.5(d)). Therefore we are not too concerned that the 400-year model result has proportionally less 5-SAOs than in the ERA-40 data. Forty-five years of the observation are probably too short to establish a robust statistics on the distribution; two hundred years are needed. The results presented below for perpetual solar forcing runs are from the two-hundred-year runs.

The correlation of the QBO period with the TSI index is small in the model 200-year run. The correlation coefficient is 0.172, consistent with that in the ERA-40 data of 0.05; neither is statistically significant. This result applies to the entire stratosphere, since the QBO period is almost constant with height in both model and ERA-40 data, within an accuracy of 1 to 2 months (Fischer and Tung, 2008).

4.4.2 “Perpetual” Solar Forcing Runs

Additionally, we perform 200-year constant solar-cycle forcing experiments in our model to answer the question of whether the nonstationary nature of the QBO period is caused by the fact that the solar-cycle forcing is time varying. It should be pointed out that we still have the seasonal cycle in the “perpetual” solar runs. Figure 4.6(c) is similar to figure 4.3 except for the “perpetual” solar-cycle mean forcing, in the 200-year runs. There are

no qualitative differences in the results between the “perpetual” solar forcing run and the variable solar-cycle forcing run. In particular, the QBO period still jumps irregularly from 4-SAO periods to 5-SAO periods and back. We therefore conclude that the nonstationary nature of the QBO period is not caused by the fact that the solar-cycle forcing is time varying.

4.4.3 Exaggerated, “Perpetual” Solar-Cycle Forcing

Figure 4.6(a) is for the perpetual $15\times\text{SC-min}$ condition. At this low solar forcing, the QBO period is mostly at 4-SAO periods. At the slightly higher, but still low, $10\times\text{SC-min}$ forcing, the QBO period consists mostly of 4-SAO periods, with occasionally a 5-SAO period (see figure 4.6(b)). Figure 4.6(d) shows the result for the high solar forcing, at $10\times\text{SC-max}$, case. There are now more 5-SAO periods than 4-SAO periods. Figure 4.6(e) shows the case for still higher SC forcing, at $15\times\text{SC-max}$. The distribution shifts towards even more 5-SAO periods. The histograms for the QBO periods for these five cases are shown in figure 4.7, along with an additional case of $5\times\text{SC-max}$.

In summary, we find that even with perpetual solar forcing, the nonstationary jumps in QBO period continue, with a tendency to jump to longer periods with higher solar forcing. Thus there appears to be some modulation of the QBO period by the SC, but such modulation is only apparent at exaggerated solar forcing. Furthermore, the correlation of solar forcing magnitude and the average QBO period is positive, in contrast to the implication by some previous authors that the QBO period is longer during solar min. In the realistic case of periodic solar-cycle forcing, the instantaneous correlation of

the QBO period with the SC is not statistically significant, consistent with the ERA-40 result.

4.5 Partition of the QBO Period into Westerly and Easterly Durations

In figure 4.8 we plot the QBO period as a function of the solar index in units of solar flux (one unit represents one half of the difference of solar fluxes between the SC-max and SC-min) over the pressure range from 10 to 80 hPa in the model. This establishes that the mean period of the QBO, including its easterly and westerly durations, generally increases as the solar flux increases, contrary to the finding of previous authors that the period reaches a maximum during solar minima. In this model there is little variation of the mean (and also individual) QBO period with height (panel (a) has lines for 7 levels from 7 to 80 hPa overlapping and indistinguishable from each other). Above 30 hPa, it is the easterly duration that varies with solar flux (figure 4.8(b), (c) and (d)), while below 50 hPa it is the westerly duration that varies more with solar flux (figure 4.8(e)), consistent with the observational result of Fischer and Tung (2008). The occasional stalling of the easterlies at 30 hPa and the prolongation of the westerly duration at 50 hPa are not seen clearly in these figures because only the average is shown, but these cases can be seen in the height-time diagrams shown previously in figure 4.6.

In this model, stalling of the easterly descent tends to occur in some years at around 40 hPa. Below that level, the westerly duration becomes longer in these years. The westerly duration lasts between one and two years. As the solar-cycle flux increases, the westerly

duration becomes longer. Therefore it is the average westerly duration near 50 hPa that is correlated with the solar flux, while the easterly duration there shows much smaller variability from one QBO period to the next. Since the next westerly phase is not initiated at the upper stratosphere until the westerly region in the lower stratosphere wanes—due to the filtering of the westerly waves by the lower stratospheric westerly region—the easterly phase above 30 hPa is correspondingly lengthened, and its mean value is correlated with the solar flux. This is consistent with the finding of Salby and Callaghan (2000), except that here the correlation with the solar flux is positive instead of the anticorrelation found by them.

4.6 Possible Mechanisms for Solar Modulation of QBO Period

As mentioned above, one unique feature of the QBO variability is the apparently random “quantum” jumps in its period from one SAO multiple to another. This is found in observation and in this model with and without a variable SC forcing. An explanation for this behavior is given in Kuai et al. (2008), as a result of the QBO trying to satisfy two often incompatible factors in determining its period: its period as determined internally by the wave forcing amplitude and the wave speed (see Plumb (1977)), and that its period has to be integer multiples of the SAO period. The latter is not an absolute requirement, but the westerly phase of the SAO initiates (and thus seeds) the westerly phase of the QBO in the upper equatorial stratosphere, where it is generally easterly without the SAO. The first factor determines that the period should be approximately 28 months, which is intermediate between 4-SAO and 5-SAO periods. It achieves an averaged period of 28

months by jumping between 4-SAO periods and 5-SAO periods. And it does so even if the solar forcing is held constant. These nonstationary jumps, of about 6 months from one period to another, account for most of the variability of the QBO period, and can probably account for the contradictory findings of correlation and anticorrelation with the SC depending on which segment of record one examines.

Nevertheless, there does exist SC influence on the mean QBO period. These effects are weak but are detectable in the model, and appear to be opposite to what was previously proposed. We offer an explanation below.

The partition of the whole QBO period into its easterly and its westerly parts in the lower stratosphere depends on the equatorial upwelling rate of the global Brewer-Dobson circulation. Camp and Tung (2007) found that the polar stratosphere is warmer because of the higher frequency of sudden warmings (Labitzke, 1982) and therefore the Brewer-Dobson circulation is more downward in mid to high latitudes (Cordero and Nathan, 2005). This could remotely force a stronger compensating upwelling branch of the Brewer-Dobson circulation over the equator, which then slows the descent of the QBO shear zone and extends the QBO period. Because the QBO-induced secondary circulation itself is also upward for the easterly phase at the equator, the e-QBO is more vulnerable to slowing and eventual stalling, which usually occurs near 30 hPa (Plumb and Bell, 1982a, 1982b). Below the stalling level, the westerly phase persists without being replaced by the descending easterlies, leading to a longer westerly duration. In this model there is no local heating due to volcanic aerosols, and so the anomalous upwelling over

the equator is remotely forced by the breaking of planetary waves in the extra-tropics. This is the so-called “polar route” (Pascoe et al., 2005).

This feature of the occasional stalling of the easterlies and the prolongation of the westerly duration below is absent in the two-dimensional model of Mayr et al., (2003), which does not have planetary waves that interact with the mean flow altered by solar-cycle forcing. Consequently in their model the descent of the easterlies and westerlies are more uniform than here and than in the observed data. The prolongation of the w-QBO in the lower stratosphere is an important feature of the observed decadal variation of the QBO period because it delays the onset of the next westerly descent into the stratosphere by filtering out the westerly waves. In the absence of the westerly wave momentum deposition, the easterly duration is lengthened in the upper stratosphere. In the observational result of Fischer and Tung (2008), the decadal variation of the easterly duration at 15 hPa is tied to that of the westerly duration at 50 hPa. This feature is also seen in this model.

A second mechanism is the so-called equatorial route of local radiative heating by the increased solar flux in SC-max as compared to the SC-min. In this model the UV radiation of the SC forcing interacts with ozone most strongly in the stratopause region, and the resulting diabatic heating affects the propagation of the equatorial waves in the upper stratosphere and affects the wave forcing of the QBO. This solar perturbation serves to “kick” the QBO period from one SAO multiple into another, higher (on average) multiple. To test this hypothesis, we make another run by switching off the SC-

ozone feedback. Ozone in the model is then not allowed to change as SC changes, but other interactions with dynamics are still allowed. When ozone concentration is fixed, the mean QBO period changes very little with solar flux, even for up to 15 times SC-max. This experiment suggests that the small positive dependence of QBO period on the strength of the solar flux we see in the model is mostly due to this “equatorial route”. Although much more work needs to be done to fully understand this mechanism, we do not believe it is worth the effort at this time given how small an effect it has on the QBO period under realistic levels of solar forcing.

Another mechanism for solar influence on the period of QBO was proposed by Cordero and Nathan (2005), who employed a model simulation to show that the QBO circulation is slightly stronger (weaker) during the SC-max (SC-min), resulting in a shorter (longer) QBO period arising from wave-ozone feedback. They argued that this leads to the required diabatic heating that slows down the descent rate of the equatorial QBO. This wave-ozone feedback is not included in our model.

In summary, we have discussed two mechanisms of how a change in solar flux affects the period of the QBO. Both are weak under the current SC forcing—explaining perhaps about one to two months of the variability—but can nevertheless account for the tendency of positive correlation of the mean QBO period with the SC in models: (1) through a change in the strength of the Brewer-Dobson circulation by its effect on planetary waves, and (2) by local heating change in the upper stratosphere. The first mechanism is a remote mechanism, and is absent in two-dimensional models without

interannual change in planetary wave propagation and dissipation. The second mechanism is local, and affects the magnitude of the radiative heating perturbation that alters the wave forcing of the QBO. This effect is absent in models without ozone photochemistry. This mechanism responds to increasing solar forcing by changing the distribution of its period to less 4-SAO periods and more 5-SAO periods. The first mechanism, previously suggested, affects mainly the partition of the QBO into its easterly and westerly phases. Its effect on the QBO period is about one month or less. The second mechanism is effective only when the SC forcing is magnified 5 to 10 times.

4.7 Conclusions

It is well known that the polar stratosphere in winter is significantly more perturbed when the equatorial QBO is easterly than when it is westerly (Holton and Tan, 1980, 1982; Baldwin et al, 2001). A mechanism that can affect the period of the equatorial QBO, by altering the timing of the phase of the QBO relative to the polar winter will therefore have a significant impact on the circulation of the entire stratosphere. The 11-year SC has often been cited as able to modulate the equatorial QBO period, especially its westerly duration in the lower stratosphere. Salby and Callaghan (2000), Soukharev and Hood (2001) and Pascoe et al., (2005) found that the duration of the w-QBO in the lower stratosphere is lengthened during solar minima based on the observations. While confirming these results, Hamilton (2002) and Fischer and Tung (2008) found with longer datasets that perhaps the opposite may hold during other decades, which coincidentally did not have volcanic aerosol contamination. The record is not long

enough for us to establish the behavior of the solar-cycle modulation of the QBO period in a clean stratosphere, although it is not clear if the volcanoes were the culprit. In the present model where there is no volcanic influence and long runs are possible, we find that the main variability of the QBO period is not related to the SC, but is an intrinsic property of the QBO itself. “Quantum” jumps of about six months between QBO periods occur in an apparently random fashion even when the variability in the solar forcing is suppressed in the model. In shorter segments of the record, such variability can give the appearance of instantaneous correlation or anticorrelation with the SC. Examples are shown in figure 4.9: both positive and negative instantaneous correlations with the SC can be found in short segments with durations comparable to those used in previous observational studies, while there is no statistically significant correlation of QBO period with the SC in the long records of 200 or even 400 model years of periodic forcing.

When the nonstationary variability of the QBO period is averaged out in a long enough run (200 years), there is a statistically significant positive correlation of the averaged QBO period with the solar forcing: the QBO period is lengthened during solar maxima, and that the increase in period is proportional to the solar-cycle forcing. This effect is weak and can be overwhelmed by the nonstationary behavior in shorter records. This finding may reconcile the contradictory findings of Salby and Callaghan (2000), Hamilton (2002) and Fischer and Tung (2008), using observation from FUB of various lengths that show either anticorrelation or no correlation of the QBO period with the SC.

4.8 Acknowledgements

This work was supported in part by NASA grants NAG1-1806 and NNG04GN02G to the California Institute of Technology. K. K. Tung's research was supported by NSF grants ATM 0332364 and ATM 0808375 to University of Washington. We would like to thank A. Ruzmaikin and J. Feynman for useful discussions. We also acknowledge help in improving the chapter from M. C. Liang, N. Heavens, X. Guo, A. Soto, T. Lee, X. Zhang, P. S. Jiang, Y. C. Chen, D. Yang, and C. D. Camp.

4.9 References

- Angell, J. K., and J. Korshover, 1970. Quasi-biennial, annual, and semiannual zonal wind and temperature harmonic amplitudes and phases in stratosphere and low mesosphere of northern hemisphere, *J. Geophys. Res.*, **75**(3), 543–550.
- Baldwin, M. P., L. J. Gray, T. J. Dunkerton, K. Hamilton, P. H. Haynes, W. J. Randel, J. R. Holton, M. J. Alexander, I. Hirota, T. Horinouchi, D. B. A. Jones, J. S. Kinnersley, C. Marquardt, K. Sato, and M. Takahashi, 2001. The quasi-biennial oscillation, *Rev. Geophys.*, **39**(2), 179–229.
- Camp, C. D., and K. K. Tung, 2007. The influence of the solar cycle and QBO on the late-winter stratospheric polar vortex, *J. Atmos. Sci.*, **64**(4), 1267–1283.
- Cordero, E. C., and T. R. Nathan, 2005. A new pathway for communicating the 11-year solar cycle signal to the QBO, *Geophys. Res. Lett.*, **32**(18), art. no L18805.
- Dunkerton, T. J., 1983. Modification of stratospheric circulation by trace constituent changes? *J. Geophys. Res.*, **88**, 10831–10836.
- Dunkerton, T. J., 1997. The role of gravity waves in the quasi-biennial oscillation, *J. Geophys. Res.*, **102**(D22), 26053–26076.
- Fischer, P., and K. K. Tung, 2008. A reexamination of the QBO period modulation by the solar cycle, *J. Geophys. Res.—Atmos.*, **113**(D07114), doi:10.1029/2007JD008983.
- Hamilton, K., 2002. On the quasi-decadal modulation of the stratospheric QBO period, *J. Climate*, **15**(17), 2562–2565.
- Hasebe, F., 1983. Interannual variations of global total ozone revealed from Nimbus 4-Buv and ground-based observations, *J. Geophys. Res.*, **88**(NC11), 6819–6834.

- Holton, J. R., and R. S. Lindzen, 1972. Updated theory for Quasi-Biennial Cycle of tropical stratosphere, *J. Atmos. Sci.*, **29**(6), 1076–1080.
- , 1980. The influence of the equatorial quasi-biennial oscillation on the global circulation at 50 mb, *J. Atmos. Sci.*, **37**(10), 2200–2208.
- , 1982. The quasi-biennial oscillation in the northern hemisphere lower stratosphere, *J. Meteor. Soc. Japan*, **60**(1), 140–148.
- Jackman, C., E. L. Fleming, S. Chandra, D. B. Considine, and J. E. Rosenfield, 1996. Past, present, and future modeled ozone trends with comparisons to observed trends, *J. Geophys. Rev.*, **101**(D22), 28753–28767.
- Kalnay, E., M. Kanamitsu, R. Kistler, W. Collins, D. Deaven, L. Gandin, M. Iredell, S. Saha, G. White, J. Woollen, Y. Zhu, M. Chelliah, W. Ebisuzaki, W. Higgins, J. Janowiak, K. C. Mo, C. Ropelewski, J. Wang, A. Leetmaa, R. Reynolds, R. Jenne, and D. Joseph, 1996. The NCEP/NCAR 40-year reanalysis project, *Bull. Am. Meteorol. Soc.*, **77**(3), 437–471.
- Kinnersley, J. S., and R. S. Harwood, 1993. An isentropic 2-dimensional model with an interactive parameterization of dynamical and chemical planetary-wave fluxes, *Q. J. R. Meteorol. Soc.*, **119**(513), 1167–1193.
- , 1996. The descent rates of the shear zones of the equatorial QBO, *J. Atmos. Sci.*, **53**(14), 1937–1949.
- Kistler, R., E. Kalnay, W. Collins, S. Saha, G. White, J. Woollen, M. Chelliah, W. Ebisuzaki, M. Kanamitsu, V. Kousky, H. van den Dool, R. Jenne, and M. Fiorino, 2001. The NCEP-NCAR 50-year reanalysis: Monthly means CD-ROM and documentation, *Bull. Am. Meteorol. Soc.*, 247–267.

- Kuai, L., R. L. Shia, X. Jiang, K. K. Tung, and Y. L. Yung, 2008. Nonstationary synchronization of equatorial QBO with SAO in observation and in model, *J. Atmos. Sci.* **66**, 1654–1664.
- Labitzk, K., 1982. On the interannual variability of the middle stratosphere during the northern winters, *J. Meteorol. Soc. of Japan*, **60** (1), 124–139.
- Mayr, H. G., J. G. Mengel, D. P. Drob, H. S. Porter, and K. L. Chan, 2003a. Modeling studies with QBO: I. Quasi-decadal oscillation, *J. Atmos. Terr. Phys.*, **65**(8), 887–899.
- , 2003b. Modeling studies with QBO: II. Quasi-decadal oscillation, *J. Atmos. Terr. Phys.*, **65**(8), 901–916.
- Oltmans, S.J., and J. London, 1982. The quasi-biennial oscillation in atmospheric ozone, *J. Geophys. Res.*, **87**(NC11), 8981–8989.
- Pascoe, C. L., L. J. Gray, S. A. Crooks, M. N. Jukes, and M. P. Baldwin, 2005. The quasi-biennial oscillation: Analysis using ERA-40 data, *J. Geophys. Res.*, **110**(D8), D08105, doi:10.1029/2004JD004941.
- Pawson, S., and M. Fiorino, 1998. A comparison of reanalyses in the tropical stratosphere. Part 2: The quasi-biennial oscillation, *Clim. Dyn.*, **14**(9), 645–658.
- Plumb, R. A., 1977. Interaction of 2 internal waves with mean flow-implications for theory of quasi-biennial oscillation, *J. Atmos. Sci.*, **34**(12), 1847–1858.
- , 1982a. Equatorial waves in steady zonal shear flow, *Q. J. R. Meteorol. Soc.*, **108**(456), 313–334.
- , 1982b. A model of the quasi-biennial oscillation on an equatorial beta-plane, *Q. J. R. Meteorol. Soc.*, **108**(456), 335–352.

- Randel, W.J., and F. Wu, 1996. Isolation of the ozone QBO in SAGE II data by singular-value decomposition, *J. Atmos. Sci.*, **53**(17), 2546–2559.
- Salby, M. L., and P. F. Callaghan, 2000. Connection between the solar cycle and the QBO: The missing link, *J. Climate*, **13**(14), 2652–2662.
- Soukharev, B. E., and L. L. Hood, 2001. Possible solar modulation of the equatorial quasi-biennial oscillation: Additional statistical evidence, *J. Geophys. Res.*, **106**(D14), 14,855–14,868.
- Uppala S. M. , Kallberg P. W. , Simmons A. J. , Andrae U. , Da Costa Bechtold V. , Fiorino M. , Gibson J. K. , Haseler J. , Hernandez A. , Kelly G. A. , Li X. , Onogi K. , Saarinen S. , Sokka N. , Allan R. P. , Andersson E. , Arpe K. , Balmaseda M. A. , Beljaars A. C. M. , Van De Berg L. , Bidlot J. , Bormann N. , Caires S. , Chevallier F. , Dethof A. , Dragosavac M. , Fisher M. , Fuentes M. , Hagemann S. , Holm E. , Hoskins B. J. , Isaksen L. , Janssen P. A. E. M. , Jenne R. , McNally A. P. , Mahfouf J.-F. , Morcrette J.-J. , Rayner N. A., Saunders R. W. , Simon P. , Sterl A. , Trenberth K. E. , Untch A. , Vasiljevic D. , Viterbo P., and Woollen J., 2005. The ERA-40 re-analysis, *Quart. J. Roy. Meteor. Soc.*, *131*, 2961–3012.
- Zawodny, J.M., and M.P. McCormick, 1991. Stratospheric aerosol and gas experiment-II measurements of the quasi-biennial oscillations in ozone and nitrogen-dioxide, *J. Geophys. Res.*, **96**(D5), 9371–9377.

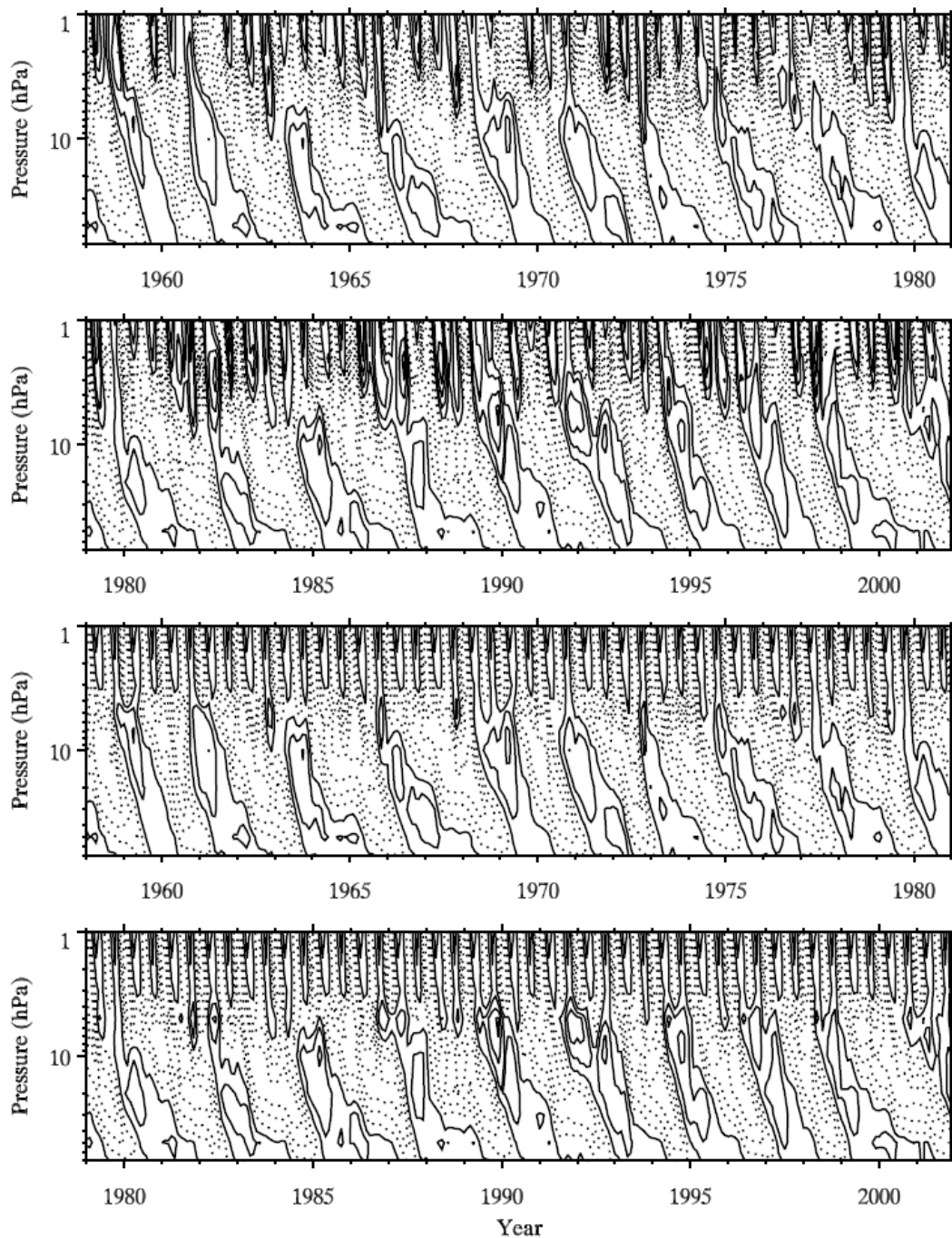


Figure 4.1 Height-time cross-section of the monthly mean ERA-40 zonal wind (top two panels). In the lower two panels, the zonal wind in the upper three levels (1–3 hPa) are replaced by its seasonal climatology, which removes the QBO and shows the SAO more clearly.

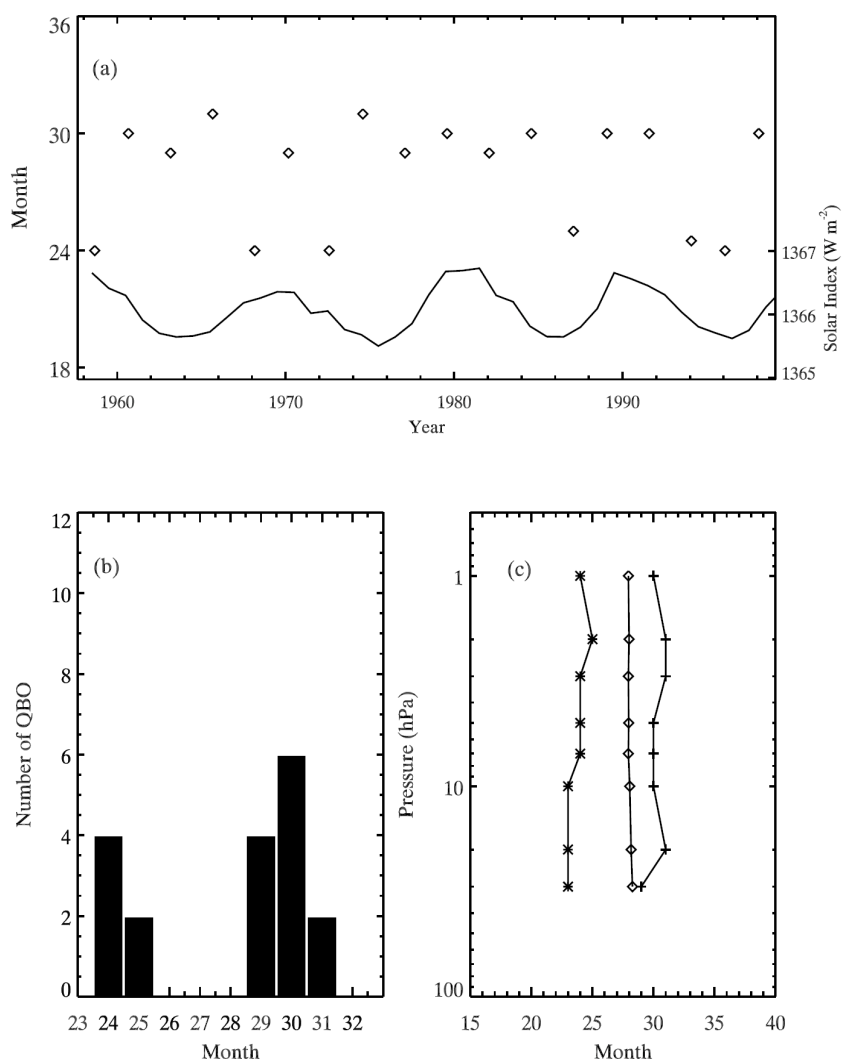


Figure 4.2 QBO period in ERA-40 data at 5 hPa. (a) QBO period counted in months (left scale). The solid curve at the bottom is the total solar irradiance (W m^{-2}) (right scale). (b) The histogram of the QBO period, counting the number of occurrences of the QBO period in month. (c) The QBO period as a function of pressure level. (*) represents the QBO during 1997, (+) represents the QBO during 1962, and diamonds represent the mean of all QBO periods in the ERA-40 record.

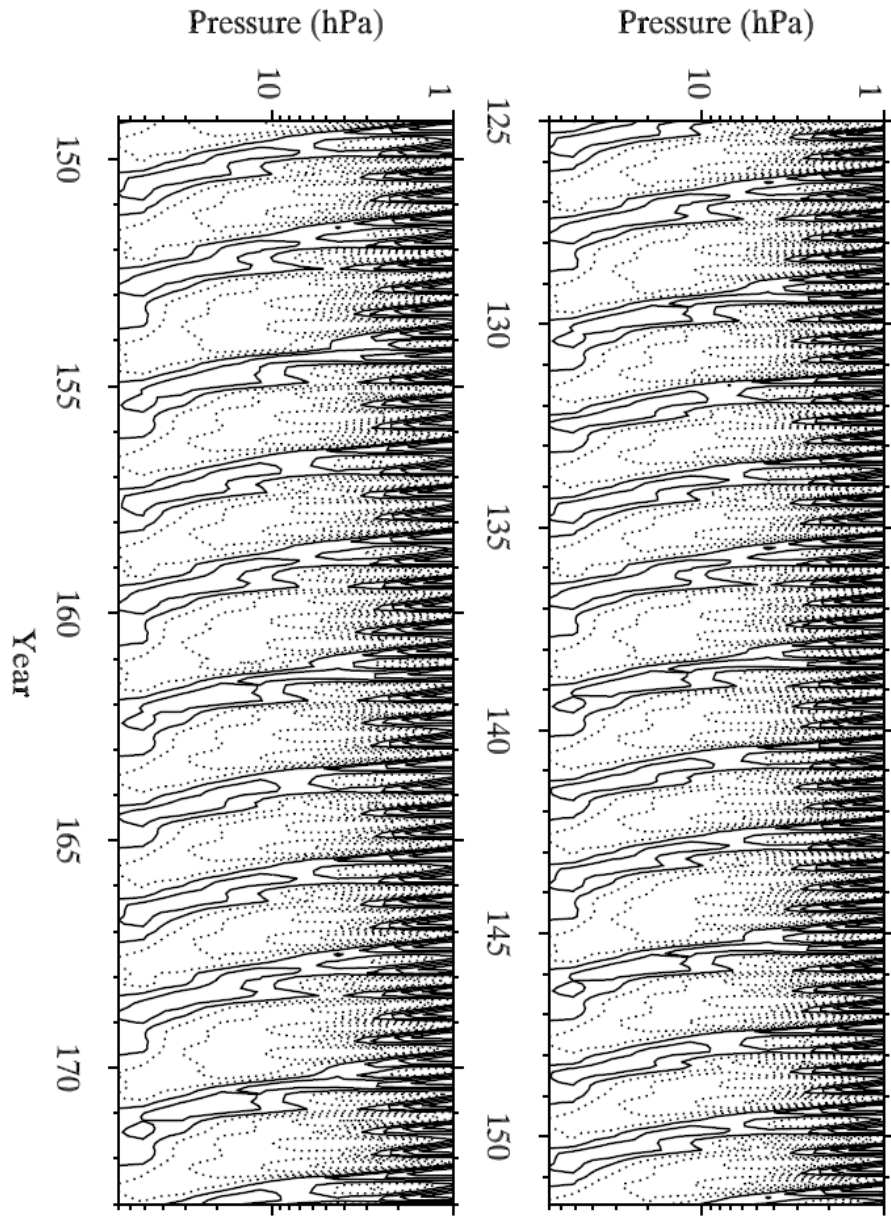


Figure 4.3 Height-time cross-section of zonal mean zonal wind for 1xSC-vary case from year 126 to 151.5 and year 149.3 to 172.8 in two panels, respectively.

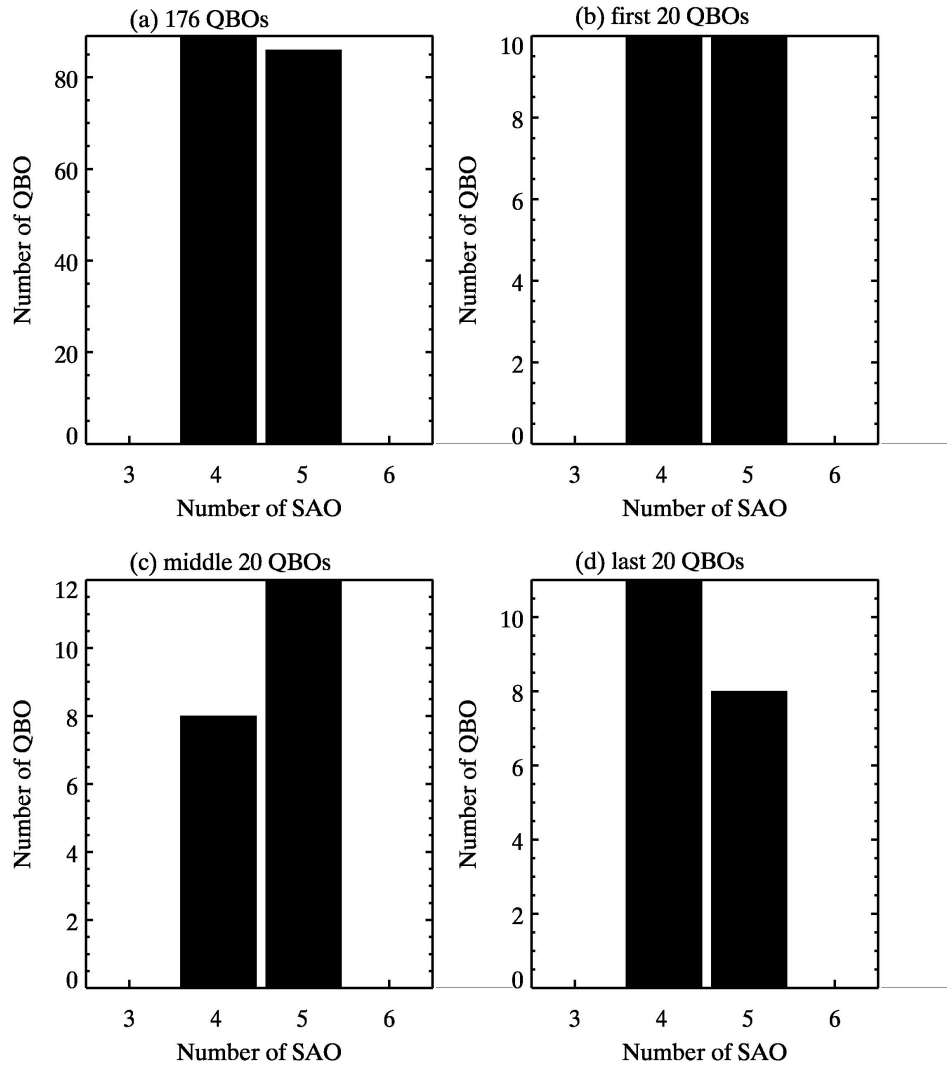


Figure 4.5 Histogram of the QBO period, counting the number of occurrences when the QBO period is 4-SAO period and when it is 5-SAO period: (a) over the 400 years period; (b)–(d) different smaller time segments of 20 QBO periods, about 40–46 years.

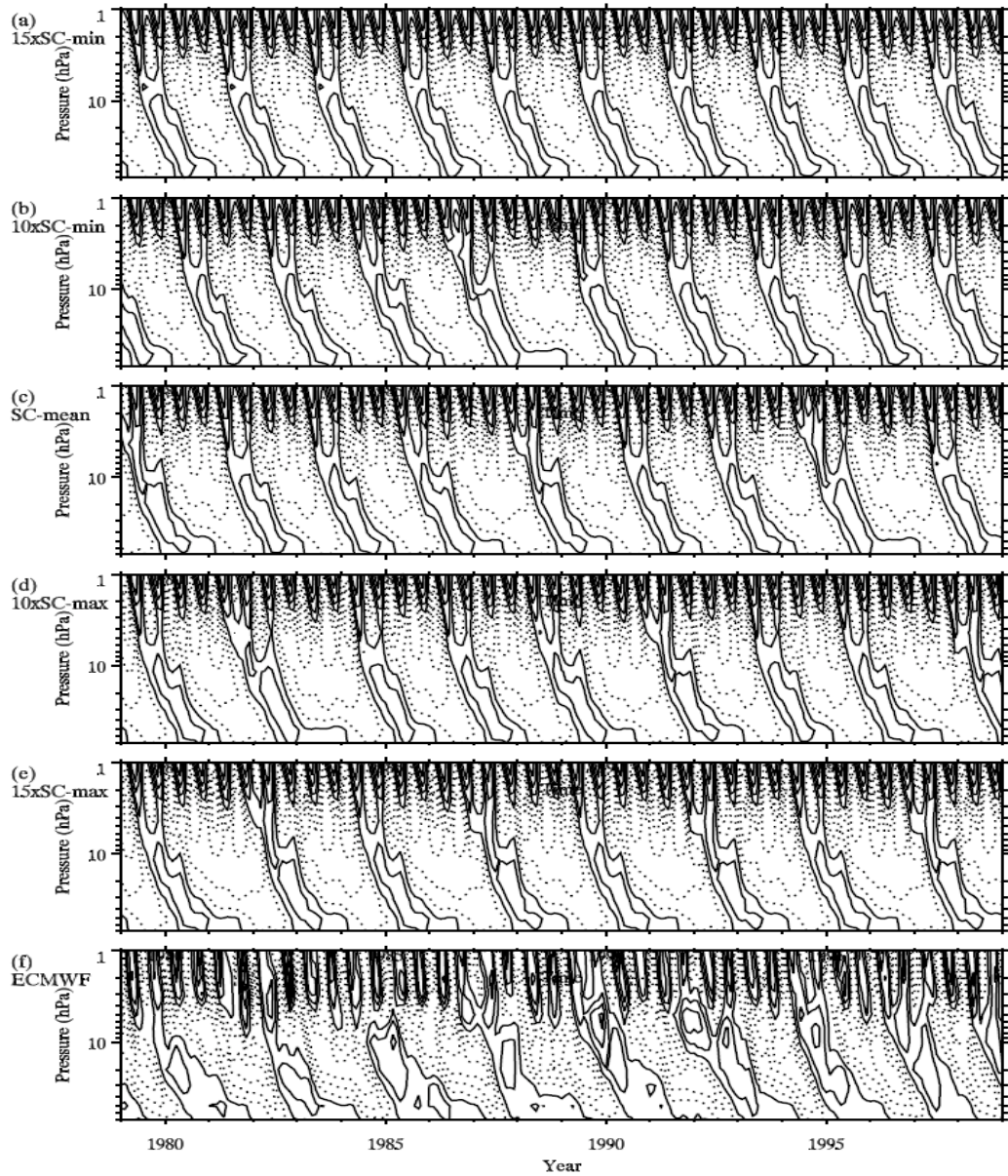


Figure 4.6 Time-height section of the equatorial monthly-mean zonal wind component (in m/s) from the THINAIR model simulation. The individual QBO period is synchronized with SAO near the stratopause. The black line is the zero-wind line. (a) $15\times\text{SC-min}$ perpetual condition; (b) $10\times\text{SC-min}$ perpetual condition; (c) SC-mean perpetual condition; (d) $10\times\text{SC-max}$ perpetual condition; (e) $15\times\text{SC-max}$ perpetual condition; (f) ERA-40 observation data.

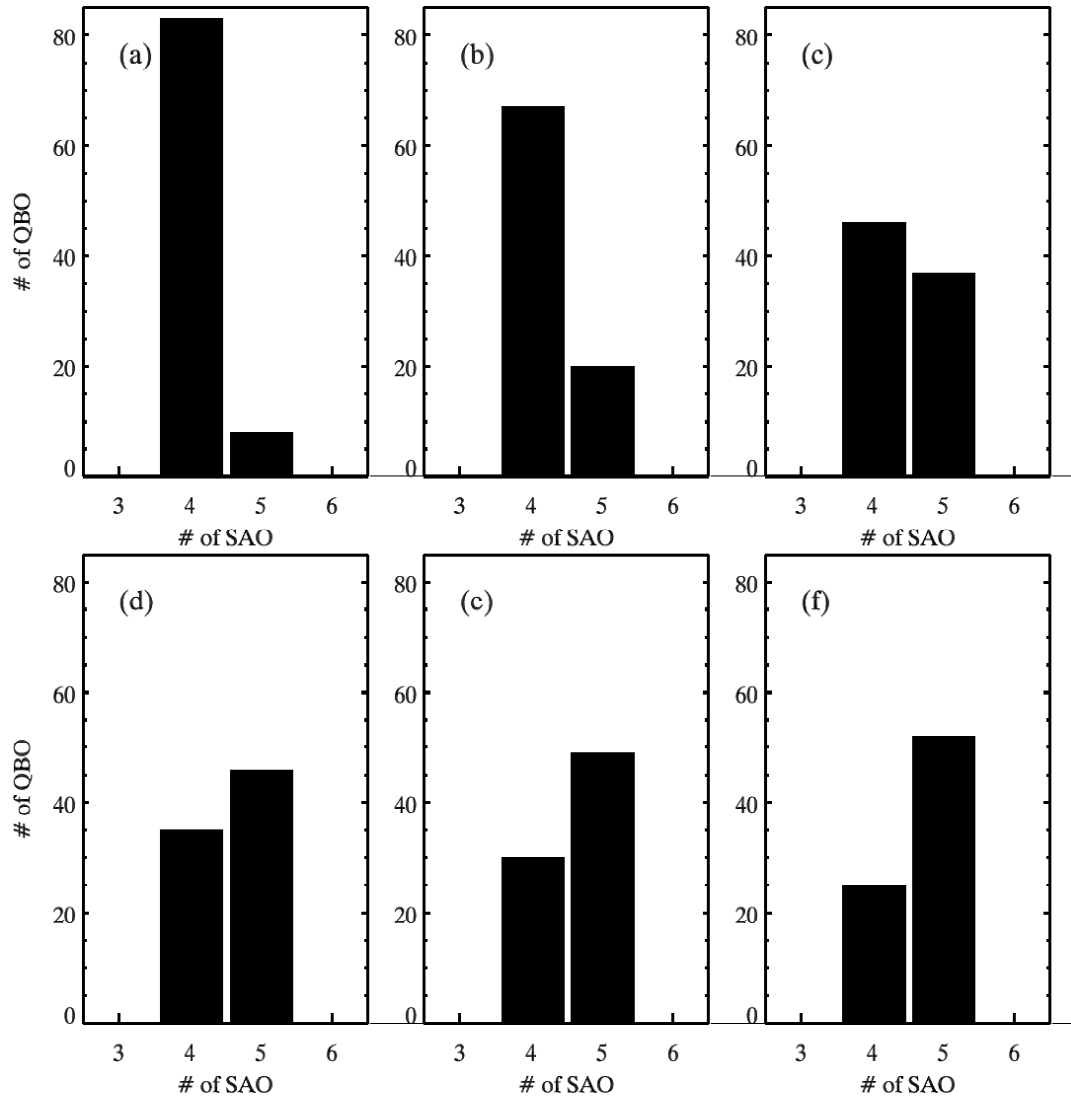


Figure 4.7 Histogram of the QBO period—the number of occurrences when a QBO period is 4-SAO or 5-SAO periods—in model runs for various perpetual solar cycle forcing. (a) 15xSC-min; the resulting averaged QBO period is 24.64 months; (b) 10xSC-min; the averaged QBO period is 25.66 months; (c) SC-mean; the averaged QBO period is 27.20 months; (d) 5xSC-max; the averaged QBO period is 26.67 months; (e) 10xSC-max; the averaged QBO period is 28.43 months; (f) 15xSC-max; the averaged QBO period is 29.04 months.

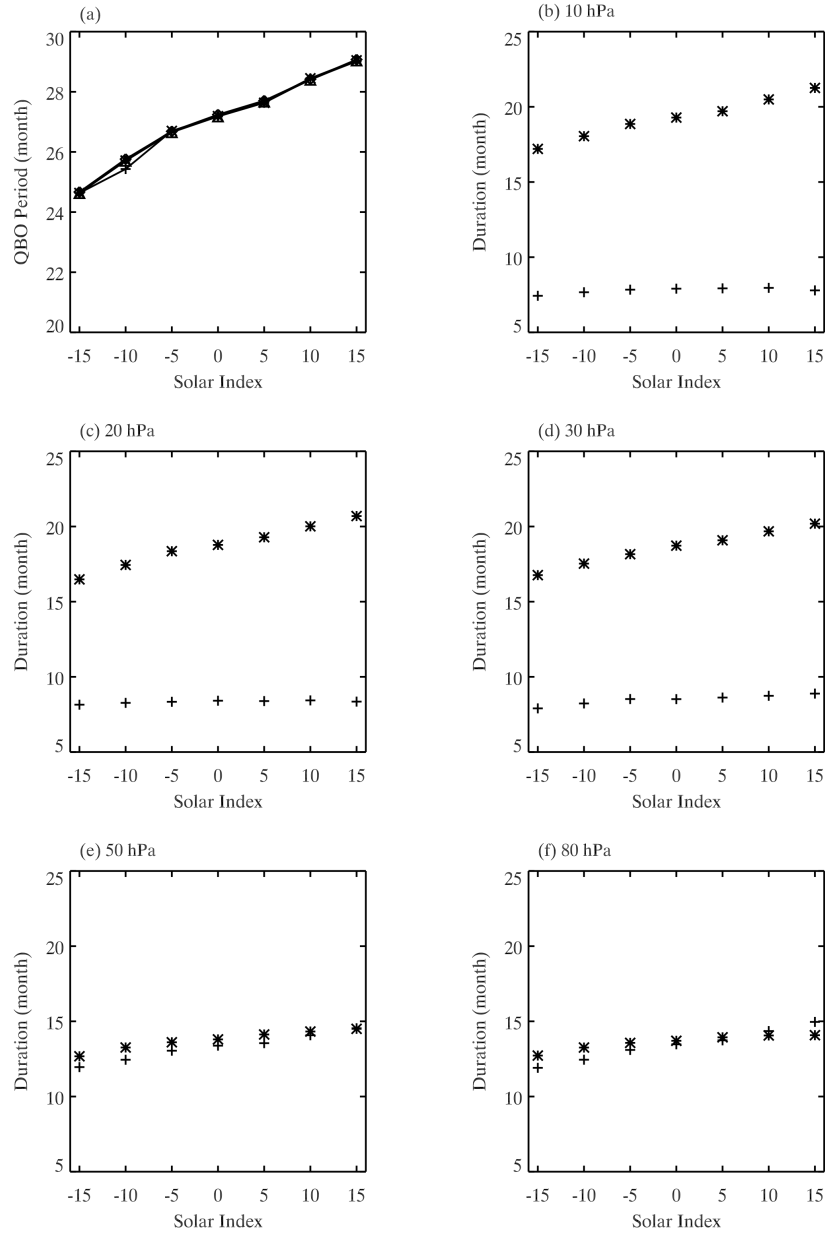


Figure 4.8 QBO period averaged over the model run, as a function of the solar forcing, in units of SC-max. (a) The QBO period at various pressure levels from 10 hPa to 80 hPa; lines mostly overlap, showing not much vertical variation. Easterly duration is shown with (*) and westerly duration with (+) at (b) 10 hPa, (c) 20 hPa, (d) 30 hPa, (e) 50 hPa, (f) 80 hPa.

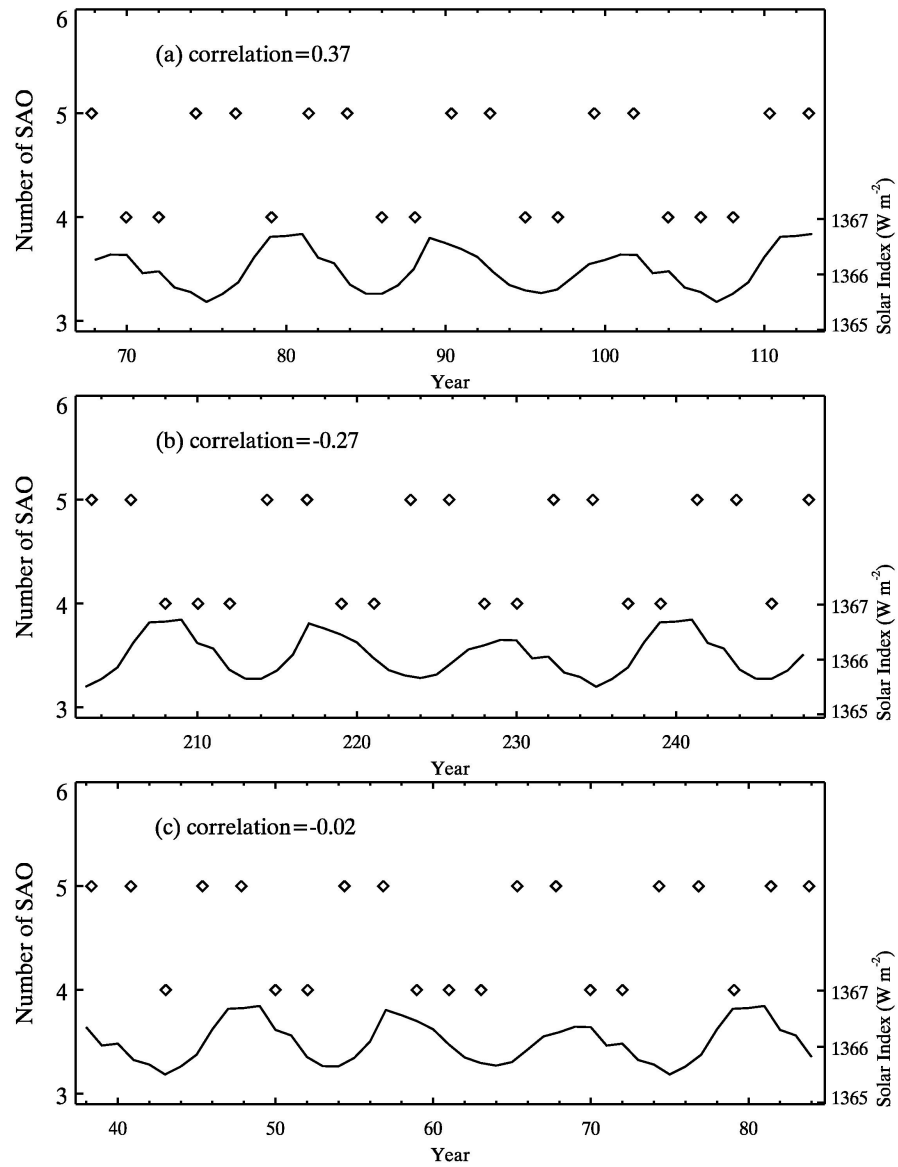


Figure 4.9 QBO periods as a function of years in the 400-year periodic solar cycle run. The TSI index is shown in solid line with the right-hand scale. The various panels are segments of the run of 40–46 years each (about 20 QBOs). The correlation of the QBO period with the TSI index is marked for each period.

